PhD-FSTM-2022-091

The Faculty of Science, Technology and Medicine

DISSERTATION

Presented on 13/07/2022 in Luxembourg

to obtain the degree of

DOCTEUR DE L'UNIVERSITÉ DU LUXEMBOURG

EN Sciences de l'ingénieur

by

Natago Guilé MBODJ

Born on the 5th of May 1991 in Dakar, Senegal

MODELING AND CONTROL OF LASER WIRE ADDITIVE MANUFACTURING PROCESS

Dissertation Defence Committee:

Prof. Dr. Peter PLAPPER, dissertation supervisor - University of Luxembourg

Prof. Dr.-Ing. Holger VOOS, vice-chair - University of Luxembourg

Prof. Dr. Olivier BRÜLS - University of Liège

Prof. Dr. Slawomir KEDZIORA, chairman - University of Luxembourg

Prof. Dr.-Ing. Matthias V. STEINKAMP - Trier University of Applied Sciences

Affidavit

I hereby confirm that the PhD thesis entitled “Modeling and Control of Laser Wire Additive Manufacturing Process” has been written independently and without any other sources than cited.

Luxembourg, 13th July 2022

Natago Guilé MBODJ

Acknowledgment

I would like to express my gratitude to my doctoral supervisor, Peter Plapper, who trusted me and helped me throughout this project and to my co-supervisors Holger Voos, Olivier Bruls and Slawomir Kedziora for their time, guidance and constructive feedback from the start to the end this work. I express my gratitude to the external jury member, Matthias Vette-Steinkamp for being part of my defence committee.

I wish to acknowledge the help from Institut de Soudure throughout the FaFil project manager Maxime El Kandaoui who facilitated and supported my works in the Robotics platform of Institut de Soudure. With that, I thank the technical and support staff in the Institut de Soudure. Thanks also to Slah Yacoubi for reviewing, supporting and evaluating my publications.

I would also like to show my deep appreciation to my colleagues and mostly to Mohammed Abuabiah who helped me finalize this project.

I extend my gratitude to the funding agency, Interreg V-A Grande Région and the University of Luxembourg for the doctoral assistance.

Finally, I thank my friends and family for their patience and support during these four years.

Abstract

Metal Additive Manufacturing (MAM) offers many advantages such as fast product manufacturing, nearly zero material waste, prototyping of complex large parts and the automatization of the manufacturing process in the aerospace, automotive and other sectors. In the MAM, several parameters influence the product creation steps, making the MAM challenging. In this thesis, we modelize and control the deposition process for a type of MAM where a laser beam is used to melt a metallic wire to create the metal parts called the Laser Wire Additive Manufacturing Process (LWAM). In the dissertation, first, a novel parametric modeling approach is created. The goal of this approach is to use parametric product design features to simulate and print 3D metallic objects for the LWAM. The proposed method includes a pattern and the robot toolpath creation while considering several process requirements of LWAM, such as the deposition sequences and the robot system. This technique aims to develop adaptive robot toolpaths for a precise deposition process with nearly zero error in the product creation process. Second, a layer geometry (width and height) prediction model to improve deposition accuracy is proposed. A machine learning regression algorithm is applied to several experimental data to predict the bead geometry across layers. Furthermore, a neural network-based approach was used to study the influence of different deposition parameters, namely laser power, wire-feed rate and travel speed on bead geometry. The experimental results shows that the model has an error rate of (i.e., 2∼4%). Third, a physics-based model of the bead geometry including known process parameters and material properties was created. The model developed for the first time includes critical process parameters, the material properties and the thermal history to describe the relationship between the layer height with different process inputs (i.e., the power, the standoff distance, the temperature, the wire-feed rate and the travel speed). The numerical results show a match of the model with the experimental measurements. Finally, a Model Predictive Controller (MPC) was designed to keep the layer height trajectory constant, considering the constraints and the operating range of the parameters of the process inputs. The model simulation result shows an acceptable tracking of the reference height.

Keywords: Laser Wire Additive Manufacturing, Parametric Modeling, Bead Geometry, Physical Modeling, Layer Height Control

Contents

List of Figures

List of Tables

List of Abbreviations

AM	Additive Manufacturing
AAM	Arc Additive Manufacturing
ANFIS	Adaptive Neuro-Fuzzy Inference Systems
ANN	Artificial Neural Network
ASTM	American Society for Testing and Materials
CAD	Computer-Aided Design
CFD	Computer Fluid Dynamics
CNC	Computer Numerical Control
FDM	Fused Deposition Modeling
DED	Direct Energy Deposition
DM	Direct Manufacturing
DMD	Direct Metal Deposition
EBAM	Electron Beam Additive Manufacturing
EBM	Electron Beam Melting
FEM	Finite Element Method
G-Code	Geometric Code
GMAW	Gas Metal Arc Welding
LAM	Laser Additive Manufacturing
LBM	Laser-Based Manufacturing
LENS	Laser Engineered Net Shaping
LTI	Linear Time Invariant
LWAM	Laser Wire Additive Manufacturing
LWMAM	Laser Wire-Feed Metal Additive Manufacturing
MAG	Metal Active Gas

MAM	Metal Additive Manufacturing
MD	Metal Deposition
MIG	Metal Inert Gas
MIMO	Multiple Input Multiple Output
ML	Machine Learning
MPC	Model Predictive Controller
PAW	Plasma Arc Welding
PBF	Powder Bed Fusion
PI	Proportional integral
PID	Proportional Integral Derivative
PM	Parametric Modeling
SLM	Selective Laser Melting
SLS	Selective Laser Sintering
SLS	Selective Laser Sintering
SMC	Sliding Mode controller
VPL	Visual Programming Language
WAAM	Wire Arc Additive Manufacturing

List of Symbols

$F(x)$	Prediction function
x_i	input variable
m	Final layer geometry dimension
y_i	output variable
$h(x)$	Hypothesis of the normalized training set
$J(\theta)$	Cost function
n	n is the number of unknown variable
$i,\ j$	Iterative element for the cost function
θ_j	Least mean squares update
α	Learning rate
f	Sum of squared errors
$J_{i,j}$	Jacobian matrix of the loss function with respect to parameters
∇f	Gradient vector of the loss function
H_f	Hessian matrix
$w_{(i+1)}$	Levenberg–Marquardt algorithm
λ	Damping factor
I	Identity matrix
P	Laser power
F	Wire feed rate
V	Travel speed (Chapter 2)
R^2	Squared error
$RMSE$	Root Mean Square Error
MAE	Mean Absolute Error
$MAPE$	Mean Absolute Percentage Error
ρ	Melt pool density
V	Volume of the melt pool (Chapter 3 & 4)
v	Travel speed (Chapter 3 & 4)
μ	Total material transfer rate (wire feed rate)
A	Cross-section area of the melt pool
w	Width of the melt pool
l	Length of the melt pool
h	Height of the melt pool/bead
Q	Laser power
a	Thermal diffusivity
C	Specific heat
T_m	Melting temperature

T	Initial temperature
Γ	Linear coefficient
d	Diameter of the laser beam in the horizontal plane
z_{pool}	Melt pool standoff
D	Laser beam diameter
f	Focal length of the objective lens
I	Intensity of the laser source
r_{p}	Proportion of laser power reflected to the melt pool
α	Melt pool absorptivity
$\dot{Q}$	Rate of heat flowing into the melt pool
T_s	Sample time
P_h	Prediction horizon
C_h	control horizon
Q_i	Input weight matrix
Q_o	Output weight matrix
s^y	Scale factor of the plant output
w_i^y	Tuning weight for the plant output
u_{lb},u_{ub}	Low bound and upper bound of the input
y_{lb}, y_{ub}	Low bound and upper bound of the output
$y(k+i\|k)$	Predicted value of the plant output
$r(k+i\|k)$	Reference value
k	Current control interval
ϵ_k	Non-negative slack variable
e_i^2	Error between the estimated output (prediction) and the training set
w_j	Weight applied to the neuron's input to produce the output

Chapter 1

Introduction

1.1 Background

Recently, Additive Manufacturing (AM) has been developed in design and functions and has become more open to the public. Additive Manufacturing is simply the appellation for rapid prototyping, also called 3D printing. Additive Manufacturing (AM) is the process of adding layer-upon-layer material in order to produce a hard-compact physical object. A layer is a cross-section of the material used as a deposition path. Earlier, AM was used to visualize products as they were being developed. Today, with the advancements in material science, more robust and accurate pieces can be created without losing material like traditional subtractive manufacturing. Today's applications of AM can be found in automobiles, aircraft, medical implants, dental restoration, and even fashion products [2].

Over the past 30 years, the demand to create complex components at a low cost has explosively grown. Additive manufacturing which is an integral part of the "fourth industrial revolution," has today a global market size of around 4.2 billion compared to 0.25 billion in the mid-1990s [3]. The annual growth rate is averaged at 25.4% since the 1990s [4] and this impressive compound (CAGR) of growth is set to evolve from US12.1 billion up to over 20 billion at the end of 2020 [5]. Additive manufacturing is also a pillar in research and innovation and represents precisely over 64% of the private sector research development expenditure and over 49% of the innovation expenditure in Europe. The AM sector regroups 2 million enterprises (around 1 in 10 of all enterprises in the EU-27 are non-financial business economies). Also, 2,078 billion in gross value was added, and 32.1 million jobs were created in 2019 in the EU 27, including 14.5 million jobs in advanced manufacturing) [6]. Moreover, the market revenues of lasers in additive manufacturing are increasing steadily with a year-on-year growth rate of 50.7% from 2014-2015 and forecast for 41.1% growth from 2015-2016 [7]. This impressive year-on-year growth is the largest percentage growth relative to other laser categories and underpins the steadily growing market share of lasers in total market revenues in the additive manufacturing sector and represents an increase of around 1% of total market revenue annually) [8].

Hideo Kodama of the Nagoya Municipal Industrial Research Institute presented in 1981, a technique to print plastic using a photo-hardening polymer. Some years after, Charles Hull patented the STL (StereoLithography) file format and developed a prototype to create parts by curing a liquid photopolymer resin using UV lasers based on Kodama's concept. The machine, which is the first produced 3D printer, will be commercialized later, allowing engineers to gain significant time to create 3D designs. At the end of the 1980s, Scott Crump invented Fused Deposition Modeling (FDM) process. Between the 1980s and 1990s, 3D printing technology started to be widely used by scientists for industrial and medical applications. A synthetic scaffold is printed to grow a human bladder at the Wake Forest Institute. At Stanford University, a micro-casting application was performed using AM. Metal deposition techniques are started to be applied to repair or modify some metallic components. 2000s were the years where additive manufacturing technology started to soar quickly. The Selective Laser Sintering (SLS) machine is commercialized. Since then, various types of 3D printers are commercialized and available in the market [9, 10].

AM technology is divided based on seven types of processes as shown in Figure 1.1 The American Society for Testing and Materials (ASTM) proposed the innovative classification. They are: 1) Binder Jetting, where the deposition is done selectively by a liquid binding agent onto the material. 2) Direct Energy Deposition (DED), or direct manufacturing, creates the part by melting the metallic material using a power source. 3) Material Extrusion or Fused Deposition Modeling where a nozzle is used to deposit materials. 4) Material Jetting: where the deposition occurs through droplets of materials. 5) Powder Bed Fusion or laser sintering where thermal energy melts the material coming out from a powder bed to produce parts. 6) Sheet Welding in which bond sheets of materials are arranged together. And finally, 7) Vat Photopolymerization, where light is used to produce a liquid photopolymer in a vat [11].

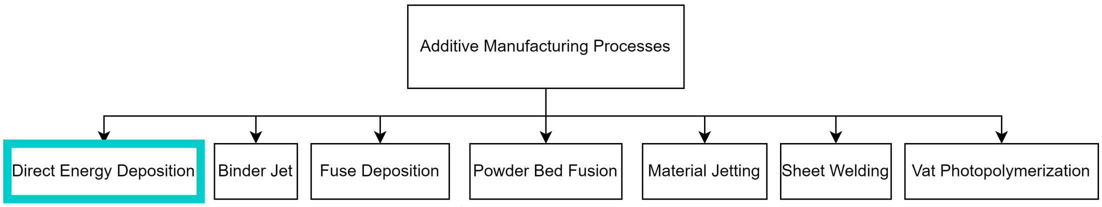

Figure 1.1: Additive Manufacturing types

Each of these seven categories has its approach. This thesis concerns the Direct Energy Deposition (DED) technique. Metal Deposition (MD) is a 3D printing concept used to create parts from a Computer-Aided Design (CAD) drawing. Metal 3D printing can employ one of the following methods: Directed Energy Deposition, Powder Bed Fusion, Binder Jetting, Metal micro-droplet derived from Material Jetting where 3D parts are fabricated using micro-droplets which are deposited onto a substrate layer-by-layer.

Metallic depositions are supplied either by a powder or a wire. The powder-feed process is practical when fabricating small parts while looking for high geometrical accuracy. Contrarily, the wire-feed approach offers an environmentally friendly process by being cleaner, therefore, does not expose operators to potential hazards. It also has up to 100 % of the deposition rate of the wire material. Moreover, the metal wire is more cost-competitive, and is more abundant than metal powder. Finally, the wire-feed approach affords a larger build volume with almost no limitation provided the printing device has the capability [12].

Large-scale AM usually requires large-size machines and post-processing. However, both of them are costly. Therefore, new methods for a reliable product manufacturing process that include large size and stable deposition should be developed. The aeronautical sector is highly interested in the new methods to meet the expectation of lighter and high-strength plane parts. The new method should consider the material properties, the process parameters and the printing device properties to create the product and keep a good geometrical accuracy of the parts. This thesis develops a modelization and control methodology of the layer metal wire deposition process to ensure a stable design flexibly while caring about the final geometrical accuracy.

Metal Additive Manufacturing (MAM) technique is the approach to creating metallic products. The MAM technologies reduce the cost of creation of metallic products directly from a CAD part, reduces the lead-time and eliminate the need for post-processes compared to other processes. The MAM technique offers more flexibility in creating metallic parts with complex geometries while controlling the deposition process [13]. That is why the interest in MAM has significantly increased in the last decade.

Metal Additive Manufacturing (MAM) is divided into two categories [14]: the Powder Bed Fusion (PBF) process, where thermal energy fuses the powder selectively, and the Direct Energy Deposition (DED) where the thermal energy melts a material to form the part. The Powder Bed Fusion (PBF) is composed of 5 types of processes that are the Selective Laser Melting (SLM), the Selective Laser Sintering (SLS), the Direct Metal Laser Sintering (DMLS), the Electron Beam Melting (EBM) and the Laser Metal Fusion (LMF). For the Direct Energy Deposition (DED), five know processes exist that are the Direct Manufacturing (DM), the Direct Metal Deposition (DMD), the Laser Engineered Net Shaping (LENS), and the Wire Arc Additive Manufacturing (WAAM). Additionally, this thesis presents a sixth new technique called Laser Wire Additive Manufacturing (LWAM). Figure 1.2 summarizes the MAM categories.

Based on the acquired understanding, the laser-based additive manufacturing process parameters can be classified based on the laser specifications, the feeding type, the material specifications, and other parameters such as the equipment settings, the path and motion parameters, etc. Figure 1.3 shows a diagram specifying the process parameters. It is found that the power of the laser, the travel speed, and the feeding rate are the main process parameters influencing the bead geometry formation and the final part accuracy [15–17].

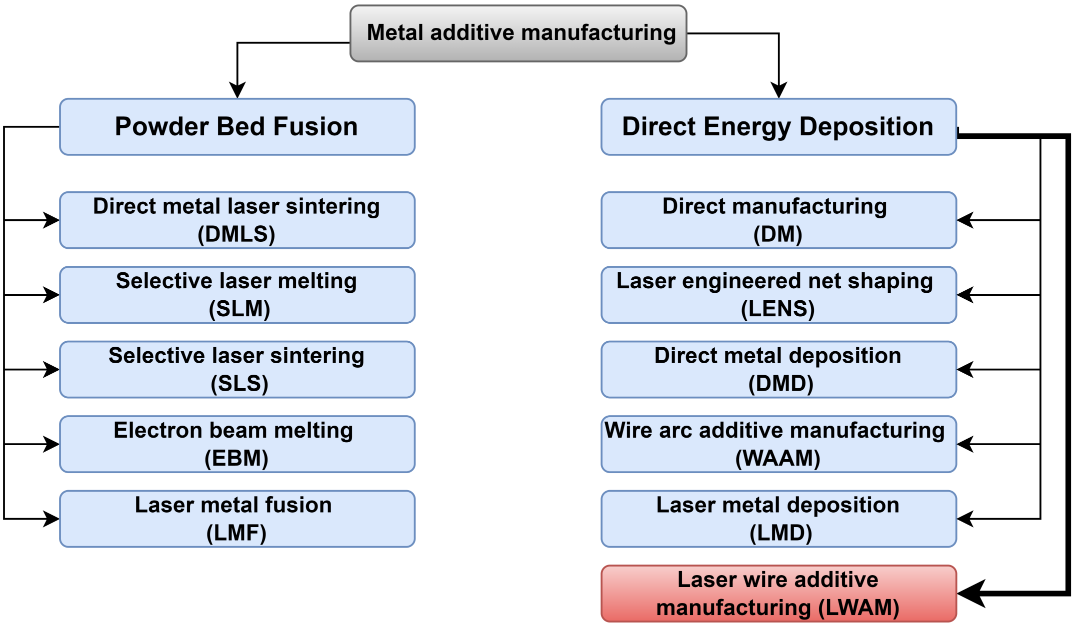

Figure 1.2: Metal additive manufacturing categories.

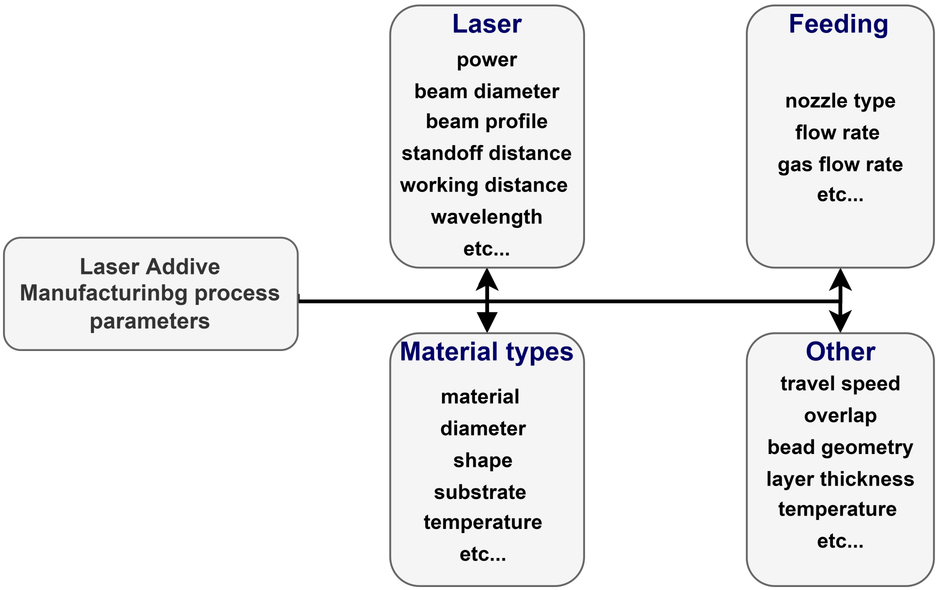

Figure 1.3: Type of process parameters in laser additive manufacturing.

Laser wire additive manufacturing (LWAM) is a subset of direct energy deposition (DED). DED is classified based on the energy source, and the feedstock. Power or wire are the principal feedstock employed for DED. The energy can come from a heat source or a cold spray technique. The heat source can be an arc, a laser, a plasma and an electron. Figure 1.4, illustrates the DED classifications.

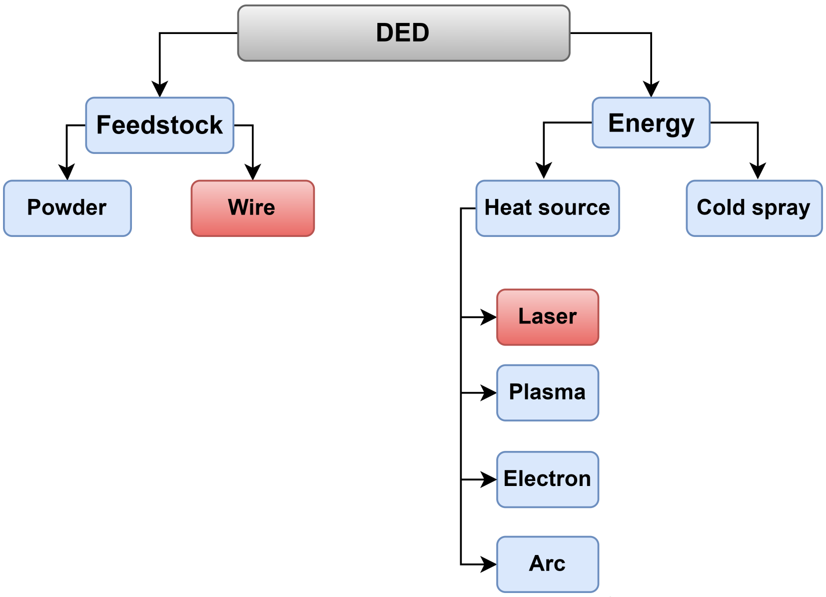

Figure 1.4: Direct energy deposition types.

DED has a high energy efficiency compared to PBF. Also, DED saves a huge amount of raw material compared with conventional manufacturing techniques. Further, DED is flexible, time-saving and does not need a special tool to create the product [18]. For most DED methods, a heat source melts a wire or powder to deposit metal. The laser method has been the best technique because it provides good geometrical accuracy, provides easiness to control, and is cleaner. The powder approach is generally axed to manufacturing small complex parts with a slow deposition speed. The powder-based approach is prone to defects such as pore formation, weakening the final product [19]. In general, the wire-based approach has higher deposition rates than the powder-based approach. A higher deposition rate is desirable for fast product manufacturing in a short time. Also, the wire-based approach does not require a sealed chamber compared to the powder-based process which must be safely run to avoid fine metal powder projections. That is why the wire-based approach does not have limitations in product dimension manufacturing. Furthermore, the wire-based is preferred for large parts because of the high deposition rate, accuracy, and safety. Also, the wire is simpler to set up and does not require a special feeding nozzle or chambers like the powder-based approach. The material deposition is near 100%; therefore, there is no need to recycle or lose some material compared to powder-based process. Finally, metal powder is more expensive than metal wires. Therefore, wire-based additive manufacturing is suitable for large and complex metal product manufacturing for its fast fabrication time and less post-machining time compared to other processes [20].

The main challenge of the wire-based approach is the stability of the process. The laser wire-based technique is sensitive to the wire feeding orientation, speed and deposition direction. Also, other deposition parameters such as the power, travel speed, and temperature are essential in the melt pool formation and geometrical accuracy of the final product. This thesis treats the challenges in the LWAM process, and proposes and validates different approaches to obtain a reliable process. A metal wire AM system needs a motion system (e.g., a robot), a heat source (e.g., laser power), and a feeding system (e.g., wire feeder). The DED technology which is closer to the LWAM treated in this thesis is the WAAM. The Wire Arc Additive Manufacturing is one of the first techniques of wire-based DED. WAAM uses an arc heat source to melt a metal wire. The formed melt pool solidifies and forms the deposited metal product guided by a motion system (ex: the robot). The WAAM started first in 1925 and was introduced by Baker and became well-known in the 1990s. In the WAAM, the heat source can be a gas tungsten arc welding (GTAW), a Gas Metal Arc Welding (GMAW), or a Plasma Arc Welding (PAW) [21]. In the WAAM process, the deposition rate varies with the type of material. It is noticed that the deposition rate is highest in tandem GMAW because of the metal wires used. The GMAW is also called the Metal Inert Gas (MIG)/Metal Active Gas (MAG) uses electrodes and a coaxial heat source to create the toolpath with less interference. However, the GMAW has a limited build volume of product due to the large melt pool and high heat. The GTAW and PAW-based WAAM have higher product quality. The limitations come from the relatively low deposition rate, the cost of maintenance and the wire feeding orientation selection [22].

The drawback of WAAM is the need for complex specialized equipment to deal with the process that needs a specific material handling safety, exposing the quality of the products and an environmental risk [23]. It also has a low deposition rate making the product creation time long. Also, the WAAM process can be complex because of many process parameters that must be controlled to obtain a good geometrical accuracy product. The process parameters are the voltage, the current intensity, the flow rate of the shielding gas and the shielding gas type, the contact tip to work distance, the wire feed speed, the travel speed, and the torch angle. Also, other parameters such as the optimal torch orientation, path planning, melt pool and bead geometry evolution for multiple layer deposition, and temperature behavior during the deposition need to be considered. These process parameters depend on the equipment type, the material type and the environmental factors and affect the transfer mode influencing the melt pool formation, the bead geometry, and the deposition accuracy [19].

In summary, the arc-based AM technology presents some challenging issues that need to be addressed. The new method discussed in the thesis, the Laser Wire Additive Manufacturing (LWAM) is a variation of Direct Energy Deposition (DED) method. LWAM uses a high laser power source to create a metal liquid molten pool. LWAM needs mostly a shroud of shielding gas to avoid contamination in the deposition. For the manipulation of reactive metals, a fully inert chamber is needed with a significant amount of gas and time to achieve the desired oxygen levels [24].

LWAM uses high laser power to melt metal wire and form a melt pool. The melt pool created is deposited first on the substrate and then layer by layer with the movement of the head to form a solid part. In this work, a 6-axis industrial robot arm performs this movement. The bead geometry formation with the process setup is shown in Figure 1.5.

The laser wire additive manufacturing has many advantages. The process offers the possibility to print at wider path widths, thus offering the opportunity to deposit high deposition rates compared to the other processes. This gives the LWAM the possibility of printing large scale object. The process has a high deposition rate compared to existing processes. This allows for lower product manufacturing costs and time for large parts compared to other methods that need post-processing. Also, the LWAM uses high power density and laser flexibility allowing a good control to manufacture parts with near-net shape features

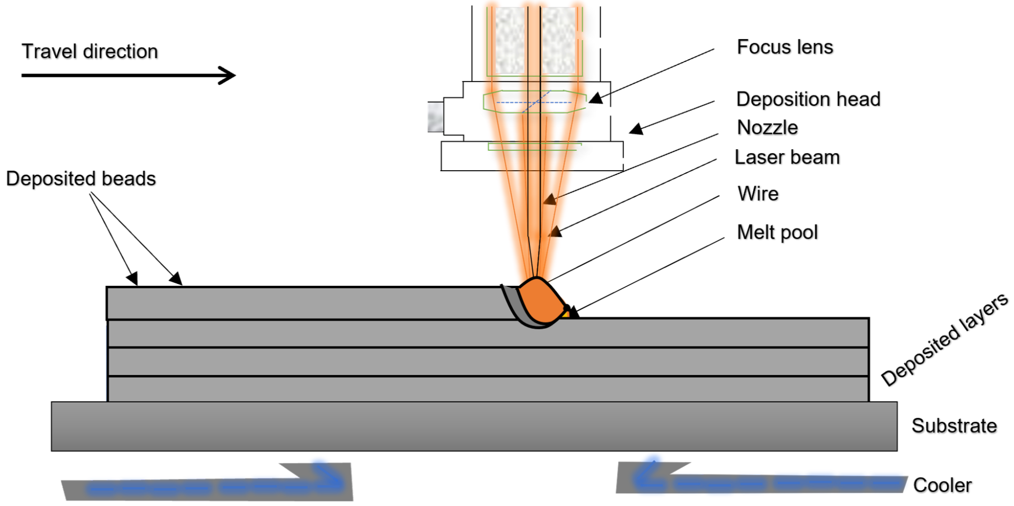

Figure 1.5: Bead deposition process

with better metallurgical qualities, thus offering more cost savings and high design freedom. That means that the products from the LWAM exhibit high strength bounding structures and nearly zero porosity. The LWAM uses a six-axis robot and sometimes a positioning table. This offers the possibility to create freedom products articulating the robot and the movable table. Also, the experimental setup in the LWAM offers a better opportunity to work around complex shapes such as overhangs and bridges.

With all cited advantages, the LWAM process can be used as an alternative to existing processes to manufacture large-scale parts. The LWAM process creates a near-net-shape part is about the same time as the casting method. However, with the LWAM, a considerable time saving is obtained when the process is well understood, and the product creature could be reduced from months to days. As long as the process is defined correctly and mastered, the LWAM can offer benefits not comparable to conventional manufacturing processes.

The main process parameters used are the laser power, the wire feed rate, and the travel speed. Other process parameters exist, such as the layer thickness, the standoff distance, and the temperature. The process parameters control the melt pool geometry (the width and the height) and also the product creation process. In an ideal condition, the process parameters are kept constant during the product creation process. However, in reality, disturbances occurring in the process impose the need to vary one or more process parameters to guarantee a smooth deposition process. These parameters influence the melt pool formation, thus the part creation. One parameter of interest in this thesis is the bead geometry. The bead geometry mainly the bead height, defines the layer thickness that needs to be selected perfectly to avoid the accumulation of errors during the part building. The bead geometry formation will depend on the heat transferred to the melt pool. This layer thickness process variable depends on the other process parameters and is particularly affected by the heat. The heat transferred to the melt pool depends on the variation of laser power, the robot's travel speed, and the input temperature of the cooler. The melt pool formation is modified when the heat provided to the process varies because of disturbances, resulting in a bead shape change. Then the bead width and height will increase or decrease in size, as shown in Figure 1.6 (See the Appendix chapter for the detailed terminology definitions). The cited problems need solutions and motivated this thesis with the following objectives:

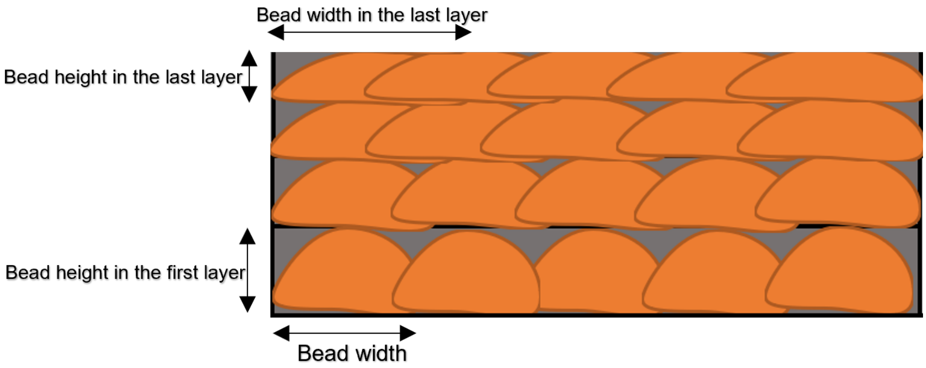

Figure 1.6: Bead geometry modification due to the thermal diffusion

1.2 Objective

The objectives of this thesis are the followings:

1. **Objective 1:** To develop a method to print parts precisely in LWAM without using G-Code.
2. **Objective 2:** To predict the bead geometry to improve the product creation accuracy.

3. **Objective 3:** To derive a complete physical multivariable model for the LWAM.
4. **Objective 4:** Finally, the acquired knowledge in **1)**, **2)** and **3)** will be used To develop a control strategy to guarantee a stable deposition.

1.3 Scientific Gap and Hypothesis

The scientific gap identifies factors influencing the process, predicting them when needed, modeling them, and controlling them to ensure process stability and material integrity, thus obtaining good deposition.

Some attempts have been made and discussed in each introduction of respective chapters. Most of them concern powder-based or arc-based processes; however, this thesis deals with LWAM and addresses the complete deposition of this new process starting from:

- **1.** The modelization using the parametric modeling approach to create the 3D printing paths from the CAD to the part creation.
- **2.** The process identification and bead geometry evolution over layers to predict the influence of the primary process parameters on the bead geometry.
- **3.** A physical model development to correlate all known process parameters and the material properties intervening in LWAM process and use an appropriate sensor to perform experiments needed to validate the physical model.
- **4.** The development of an offline process control to compensate the layer height and avoid errors accumulation.

1.4 Methodology

The following methodologies are used to fill the objectives:

1. **Methodology 1:** A parametric design method is adopted to generate these printing paths. This gives easiness in the CAD model design and deposition while allowing the designer to implement 3D printing process parameters

for robotics devices. Therefore many issues found with Geometric Code (G-Code) which is the language for Computer Numerical Control (CNC) machines are avoided. Skipping the G-code gives the designer the option to communicate directly to the robot.

2. **Methodology 2:** A neural network-based approach will be used to investigate the influence of main process parameters (laser power, wire feed rate and travel speed) on the bead geometry.
3. **OMethodology 3:** A complete physics-based multivariable model that describes the LWAM process is created. The model includes material properties and all known process parameters. Also, the influence of standoff distance is included in the model as it plays a significant role in the layer thickness definition.
4. **Methodology 4:** A Model Predictive Controller (MPc) is created to predict the layer height and keeps variables at their operating ranges.

The laser wire additive manufacturing process needs to be understood to be applied to create parts. The deposition starting from the CAD creation to the final part, faces generally challenges leading to many phenomena that influence bead formation and deposition, thus leading to cracks and irregularities to the final part.

A complete automation process starting from the CAD model to the produced part offers an adaptive design process, providing available tools to predict and simulate deposition process, allowing the possibility to 3D print correctly metallic parts using laser-wire deposition process with a significant gain of time and understanding of the process.

1.5 Thesis Outline

The thesis is organized in the following: In Chapter 2, The 3D Parametric Modeling (PM) approach is presented. The goal of this approach is to use parametric design features to simulate and print 3D metallic objects using Laser Wire Additive Manufacturing (LWAM) process. The proposed approach includes the 3D printing path creation and robot targets assignment while considering several process requirements of LWAM and the robot system. This technique helps to develop interactive and easily the robot toolpath while including the process parameters of the LWAM process. Finally, three typical parts that are a wall, a cylinder, and a complex shape were created using the developed approach and printed.

In Chapter 3, a prediction model to improve deposition accuracy of the layer geometry (width and height) is proposed. A machine learning regression algorithm was used to several experimental data to forecast the bead geometry dimension of layers. A test split strategy was applied to train and validate the models. Finally, a neural network-based approach is used to observe the influence of the main parameters (power, wire feed rate, travel speed) on the bead geometry.

In Chapter 4, a physics-based model of the bead geometry including all process parameters and material properties was developed for the laser wire additive manufacturing process. The developed model aimed to include critical process parameters and material properties describing the LWAM process. To check the model robutsness, validations are performed.

In Chapter 5, the developed model in Chapter 4 was linearized to create a linear state-space representation form. To guarantee acceptable results, a Model Predictive Controller (MPC) was proposed. The MPC technique was chosen to keep the bead height trajectory constant and to improve the layer height compensation while taking into consideration the constraints faced in the LWAM process. The developed model is an Multiple Input, Multiple Output (MIMO) model and many of the variables influence each other and works in a limited range.

Chapter 2

Parametric Modeling Approach

2.1 Introduction

The association between parametric modeling and industrial robots opens a new way to fabricate products using Additive Manufacturing technology (AM). Where AM is simply a 3D printer device that is usually restrained to the manufacturing of small or medium size parts [25, 26]. Nonetheless, today AM equipment can also operate to fabricate large-scale objects as in the field of Metal Additive Manufacturing. [27, 28].

Metal Additive Manufacturing (MAM) process began in the late 1990s [29, 30]. The MAM is classified based on the sources of energy employed for metal deposition into Electron Beam Additive Manufacturing (EBAM), Arc Additive Manufacturing (AAM), and Laser Additive Manufacturing (LAM) [31]. Concerning the additive material form, Laser Additive Manufacturing is divided into a wire-based Laser Additive Manufacturing and a powder-based and. This thesis will focus on a new Metal Deposition (MD) process using a robot that includes many process parameters and material properties that need to be considered. The new deposition process is called the Laser Wire Additive Manufacturing (LWAM) technology.

The process of LWAM consists of melting a wire using an energy source to create a liquid melt pool bead. The beads are then added layer by layer to form the final object, as shown in Figure 2.1. Today's application of the process can be found in the automotive sector, aircraft, medical implants, dental restoration, and even the fashion sector [2, 32, 33].

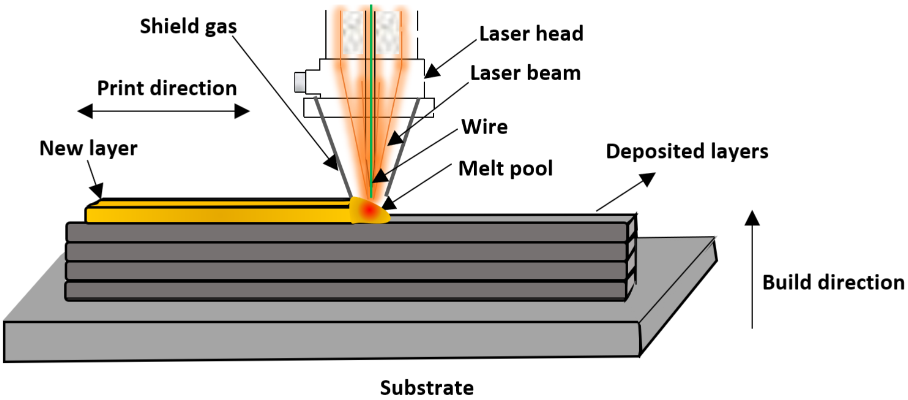

Figure 2.1: Schematic diagram of Metal Additive Manufacturing.

Despite the advances in AM, there are still many challenges related to the process applicability, cost, and deposition process parameters [1, 2, 24, 29, 33, 34]. However, one of the main challenges in AM, especially in LWAM, is the understanding and knowledge of the combination of the system's software and hardware. On the other hand, standard G-code is usually employed by 3D technology to print the final parts. 3D printers use only linear commands of the G-code to define the printing paths, whether the motions are linear or circular. Consequently, the G-code becomes computationally heavy for curvy product creation as the G-code uses straight lines to create curves. [35]. Thus one problem with the G-code technique is that it can be inadequate to create complex parts [36]. Furthermore, it is complicated to convert a G-code to a 3D deposition path, for complex objects, that are usable by the robot [37]. These extra works frequently result in simulation errors, time loss and process errors [38].

To overcome such limitations a method called Parametric Modeling (PM) is developed to 3D print using a robot for large-scale manufacturing processes and complex objects [39]. The evolution of computer-aided design technology imposes the creation of this method to improve the digital model creations. PM method helps the development of 3D printing in the industry to create parts on large scales using an automatic layer-by-layer deposition process [37].

Few studies can be reported using parametric designs in 3D printing technology. In [39, 40], Kontovourkis et al. presented two works related to the development of a parametric design approach and an automated model for 3D clay printing. In [39] the authors gave an insight for 3D clay printing using a parametric environment and a robot. While in [40], Kontovourkis et al. showed the development of a parametric-integrated algorithm for 3D printed earth and clay-based materials using an industrial robot. On the other hand, Fischer et al. [41] presented an overview of concrete 3D printing and an online parametric customization and fabrication of small 3D concrete printed pavilions. While Jeong et al. [42], used a parametric design method to create 3D printed wearable fashion products using the Fuse Deposition Manufacturing (FDM) process. The work demonstrated that parametric design method features could produce fashion products. In [43], Naddeo et al. used parametric algorithms in a finite element environment to simulate curved beam lattice structure. The comparison between the numerical results and experimental results confirmed the validity of this approach that could be used for different solid shapes. Finally, Lim et al. [37] proposes a parametric design to generate curved-layered printing paths for large-scale construction processes. Scripting languages are used to slice layers and provide printing paths adjustable interactively to fit various shapes. The paths are converted to G-Code and extra Computer Numerical Control (CNC) related commands such as the nozzle on/off and pump start/stop commands, speed control of the pump, etc. added later.

The Parametric Modeling approach has not been yet developed and adapted to the LWAM technology to the best of our knowledge. Therefore, this chapter aims to print 3D metallic models using a novel parametric modeling design framework in the LWAM process. More specifically, the proposed parametric model includes the main process parameters (power, wire-feed rate, travel speed, bead geometry), skips the G-Code conversion step and provides directly a 3D printing code for the assigned robot (see Figure 2.2). The proposed approach also offers a user-friendly method for printing metal objects and taking into consideration different process requirements, the deposition rules, the robot system and the virtual simulation of the process before the real deposition. For the validation, a wall, a hollow cylinder and a complex shape model will be simulated and experimentally printed to confirm the feasibility of the proposed approach. The remaining of this chapter is structured as follows, Section 2.2 introduces methodology, while Section 4.3 presents the experimental results and discussion. This chapter finishes in Section 2.4 with a summary.

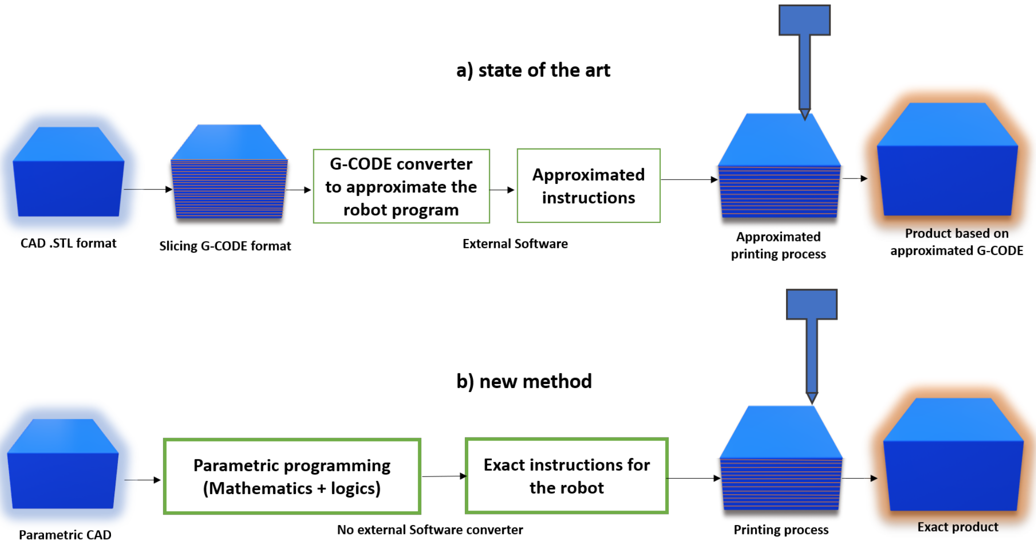

Figure 2.2: (a) Conventional 3D printing using G-code approach; (b) Proposed 3D printing technique using Parametric Modeling Approach.

2.2 Methodology

The association between Parametric Modeling and industrial robots opens a new way to fabricate products. This association needs an understanding and knowledge of the system's software and hardware. In this section, a methodological frame that integrates a parametric implementation for large-scale manufacturing parametric design using an industrial robot system to 3D print metallic parts is developed. More specifically, this work provides a sustainable and open-source framework to print medium and big sizes parts in a single adaptive environment. The work considers the LWAM process as a case-of-study including all its process parameters and bead geometry, and the a descriptive workflow from the CAD part to the manufacturing part.

In LWAM process, the process parameters play an important role in the final product. The process parameters choice such as the laser power, the wire feed rate and the travel speed have an influence on the robot toolpath design. The toolpath planning includes contour creation, layer height (adaptive or fixed thickness), printing direction, path pattern, and bead geometry settings. Therefore, process planning is important to create a homogeneous and stable printing process. In this work, Grasshopper software is used to achieve the task. Grasshopper uses a Visual Programming Language (VPL) that is easy to program and allows the create advanced parametric models for many computer-aided design applications.Grasshopper is developed in 2007 by McNeel Corporation [44].

Both, parametric and non-parametric CAD models can be created or imported within Grasshopper software. In this work, both approaches will be performed for toolpath creation. The proposed method enables to produce digitally various shapes and design possibilities parametrically, as shown in the flowchart illusrated in Figure 2.3. The parametric design creation is embedded in the bead width and height, layer heights, contour, and toolpath. Then, a robotic control plug-in for Rhino called HAL software [45] is used to convert each defined point to robot targets. Finally, a robot programming language is used to include printing process parameters and data related to the robot system to produce the deposition executable by the the robotic arm.

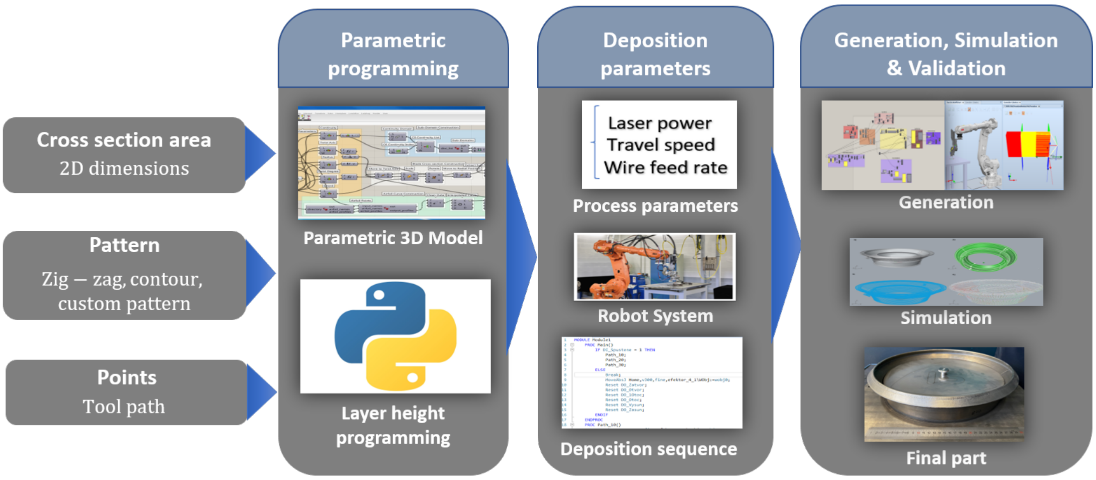

Figure 2.3: Parametric 3D printing flowchart for the LWAM process.

Figure 2.3 shows that the proposed parametric 3D printing process begins with first creating a parametric surface. In this step, a cross-section of the CAD model is created. Mathematical formulas of regular shapes (square, rectangle, triangle, circle, parallelogram, etc.) are used to create the cross-section of the final object. The object dimension and its cross sectional area parameters are given as predefined inputs, as illustrated in Figure 2.4.

After the 2D surface is created, patterns are added to it. In most 3D printing processes, patterns such as raster, zigzag, contour or concentric are commonly used in AM (see e.g., [46]). The patterns are created based on the bead geom-

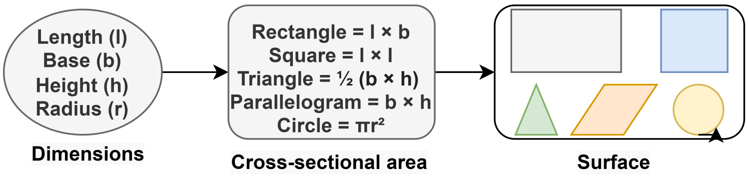

Figure 2.4: Cross section creation.

etry dimension, mainly the bead width dimension. The step-by-step process of pattern creation is shown in Figure 2.5 and Figure 2.6.

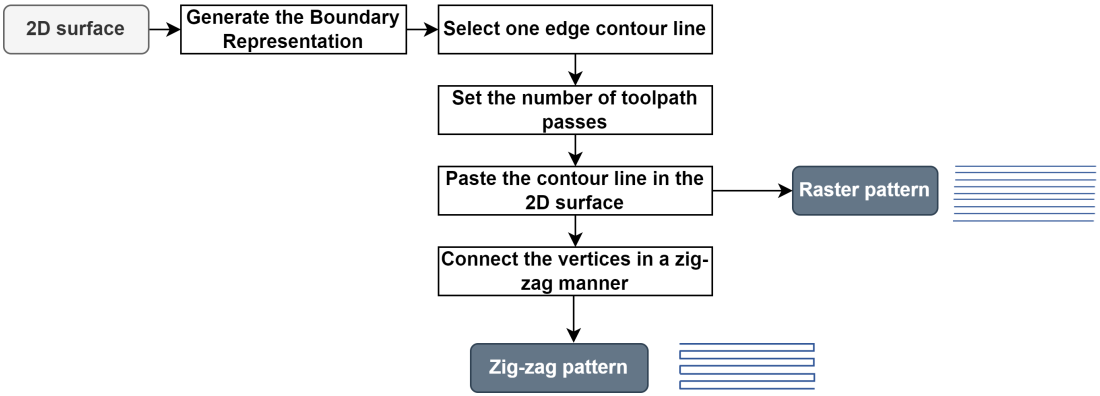

Figure 2.5: Pattern creation for raster and zig-zag patterns.

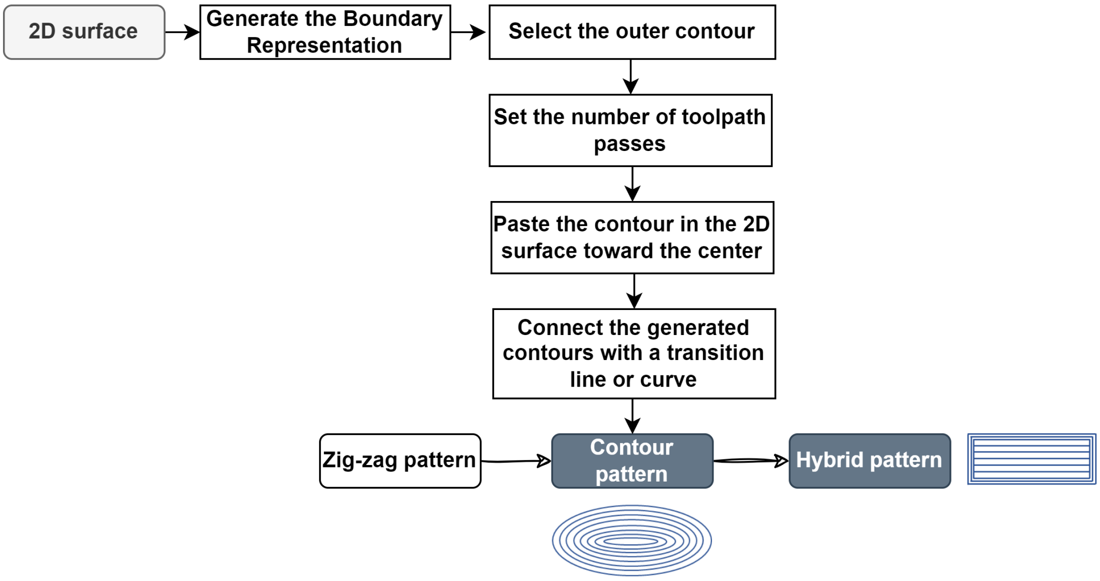

Figure 2.6: Pattern creation for contour and hybrid patterns.

The next step is to assign points to the generated patterns. These points will later be used by the robot as targets. The points are arranged and connected sequentially to form the toolpath pattern for the robot, as shown in Figure 2.7.

Noting that, after placing the points on the first layer, the generated toolpath is then copied to the other layers with fixed or variable thicknesses using a Python script. A layer thickness algorithm (see Chapter 3 is run in the script to create the toolpath patterns for each layer.

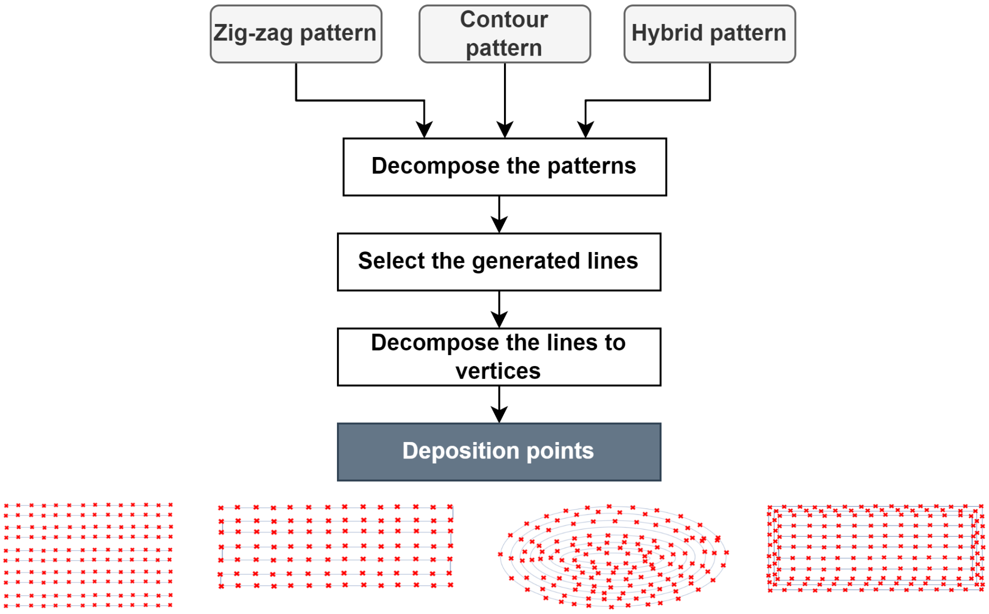

Figure 2.7: Points creation.

Hereafter a layer-to-layer travel strategy is implemented. The travel strategy is created by selecting and connecting the last point of each layer to the first point of the next layer, or vice-versa. Defining a suitable travel strategy is crucial and affects the final object geometry in terms of cooling and the bonding between layers. Lastly, all created points will be converted to robot targets to generate the 3D printing program. HAL framework is used to convert the created points to robot targets. Finally, a digital parametric object, convertible into many robot programs, is now created and ready to be used by the industrial robot to perform the printing process.

Remark: HAL is a Grasshopper plug-in allowing the translation of parametric designs to industrial robot programs. After the robot targets are created, deposition process parameters (power, wire feed rate, travel speed), the robot system (tool frame, object frames, task frames) and the deposition sequences (wait time, stop, etc) are added to the final program.

2.3 Results Verification

In this section, three cases study (wall, hollow cylinder and complex model) are performed using the described parametric approach from the surface creation to the LWAM robot program creation. The printing process starts at an assigned point in the object where deposition process parameters are activated simultaneously. The toolpath is reproduced layer by layer until the full part is created and the final object is completely simulated. After completion, the program is transferred to RobotStudio where the deposition sequences are added based on the deposition requirement. The full program is then sent to the robot controller to execute the printing process. The real robot follows the robot targets in the virtual simulation where frames are assigned to each of them. If a problem occurs, meaning the programmed points do not coincide with the real points, stop instructions integrated at specific points of the program will stop the deposition process. This will ensure that the final part is printed correctly without collision or undesirable movements that may occur.

For the three case studies, experimental tests were performed on the laser platform at Institut de Soudure. A robotized laser wire-feed system ran tests. An ABB 6-axis poly-articulated robot is used to provide the kinematics of the process. A fiber laser source, IPG Photonics with a power of 10 kW was used. A CoaxPrinter laser head is used to deliver the laser beam and the wire. Figure 2.8 shows the LWAM system setup.

2.3.1 Case 1: Wall

The first test, to validate the proposed approach, is to simulate and print a metal wall object using the LWAM technique. The construction steps for the wall printing are divided into the following steps, **(i)** defining the wall's dimension (length and width). **(ii)** Pattern creation using the approach discussed in Section 2.2. In this step, the distance between passes (filling density) is chosen according to the bead geometry dimension. **(iii)** Defining the layer height thicknesses and the layer by layer travel strategy. **(iv)** Assigning points to the defined pattern and converting them as robot targets. **(v)** Defining the robot program parameters,

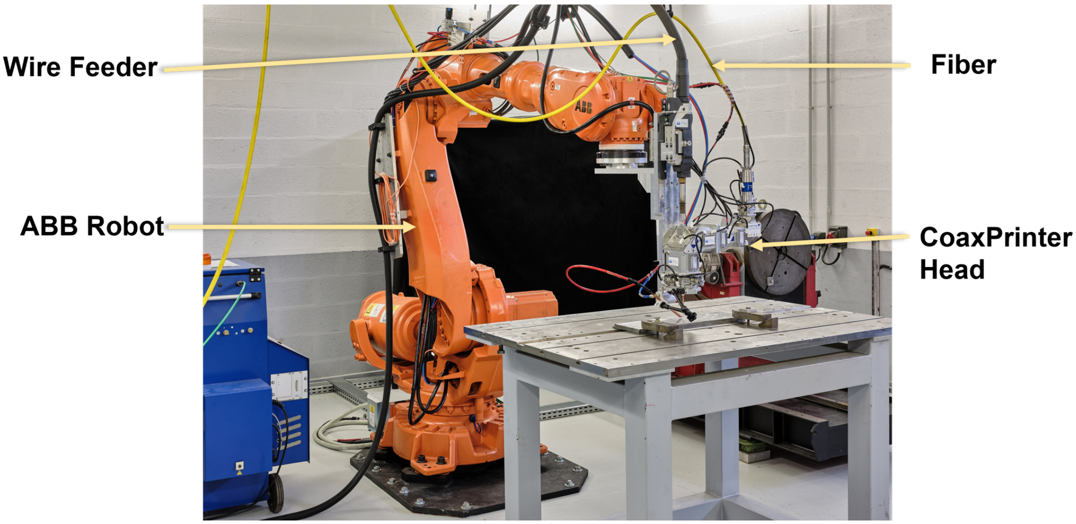

Figure 2.8: Experimental Setup of LWAM platform at Institut de Soudure.

such as the robot frames (tool, task, object), the process parameters (see Table 2.1) and the deposition sequences (stop time, wait time, process parameters ON and OFF sequences). **(vi)** Finally, the wall object is simulated and the program is transferred to the robot controller for the experimental deposition process. Figure 2.9 shows the result of the wall creation. From the result, we can notice the flexibility of the proposed technique to print a metal wall object without the need for the G-code and having similar printing object output compared with the simulation result.

Table 2.1: Case 1: Wall deposition parameters.

Power (W)	Travel speed (m/min)	Wire-feed rate (m/min)	Number of passes	Number of layers
2200	1.2	1.8	10	61

2.3.2 Case 2: Hollow cylinder

The second test, to validate the proposed approach, is to simulate and print a metal hollow cylinder object using the LWAM technique. The construction steps for the hollow cylinder printing are similar to those discussed in Case 1. For this case, a contour toolpath is designed, and the deposition parameters are given in Table 2.2. The result in Figure 2.10 shows a printed hollow cylinder object that is similar to the simulated output using the proposed approach and without the need for the G-Code.

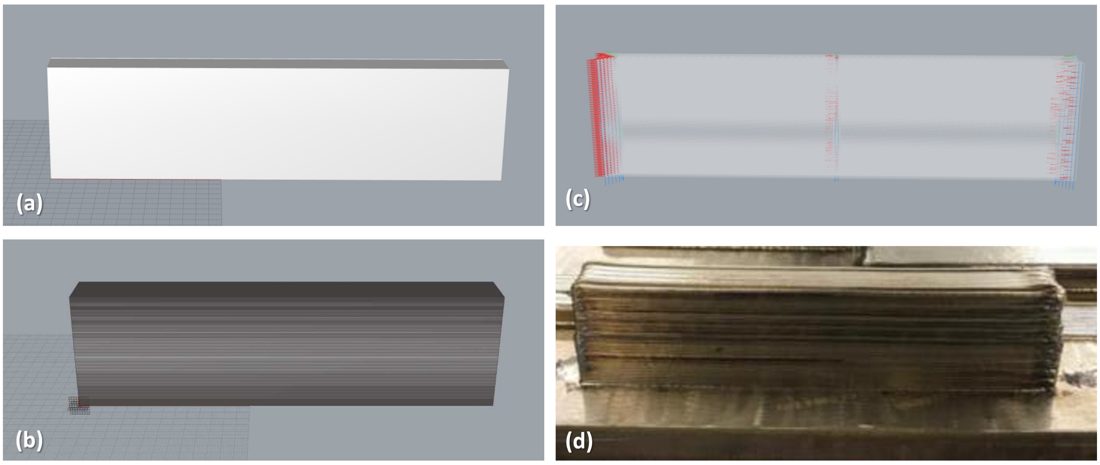

Figure 2.9: Case 1 (a) wall 3D model object, (b) wall pattern creation, (c) wall points creation, (d) printed metal wall output.

Table 2.2: Case 2: Hollow cylinder deposition parameters.

Power (W)	Travel speed (m/min)	Wire-feed rate (m/min)	Number of passes	Number of layers
2200	1.2	1.8	2	130

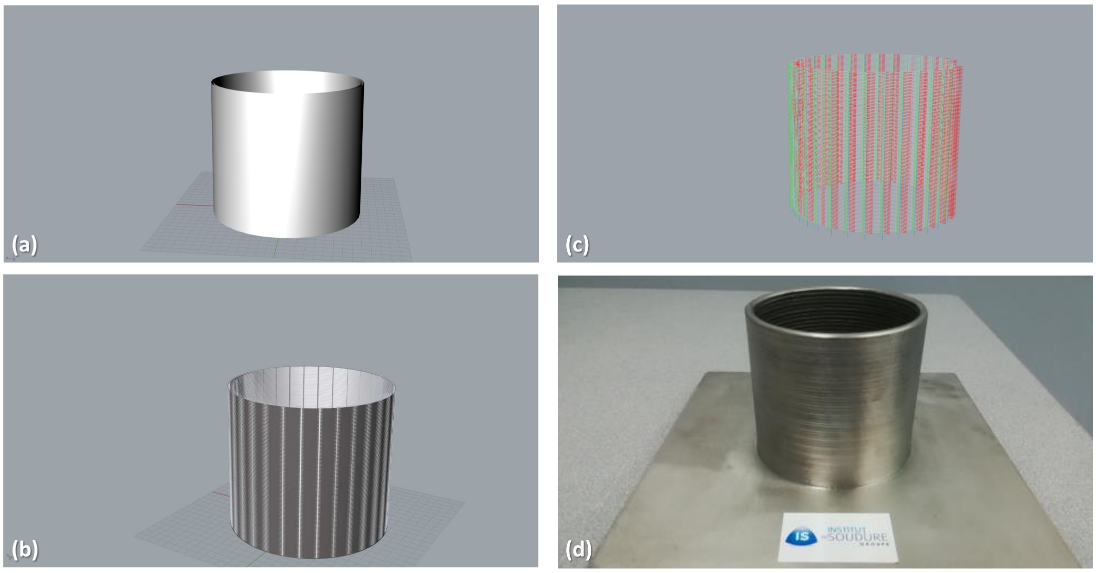

Figure 2.10: Case 2 (a) hollow cylinder 3D model object, (b) hollow cylinder pattern creation, (c) hollow cylinder points creation, (d) printed metal hollow cylinder output.

2.3.3 Case 3: Complex model

The final test simulates and prints a complex metal object using the LWAM to validate the proposed approach. For any complex objects that are difficult to create parametrically, Grasshopper offers tools to automatically parametrize such an object. The modified process steps for printing such a complex object are the following (see also Figure 2.11),

- **(i)** The CAD file for the required model is imported into the parametric programming framework.
- **(ii)** Then, the CAD model is converted to a parametric CAD file.
- **(iii)** A Brep function is used to create a boundary representation of the CAD model, where the boundary representation is composed of the boundary of the model, the solids, the vertices, the edges and the faces, as illustrated in Figure 2.12.
- **(iv)** The parametrized CAD is used then to define the layers, the pattern, the points and the converted robot targets, as it was discussed in the previous section 2.2.

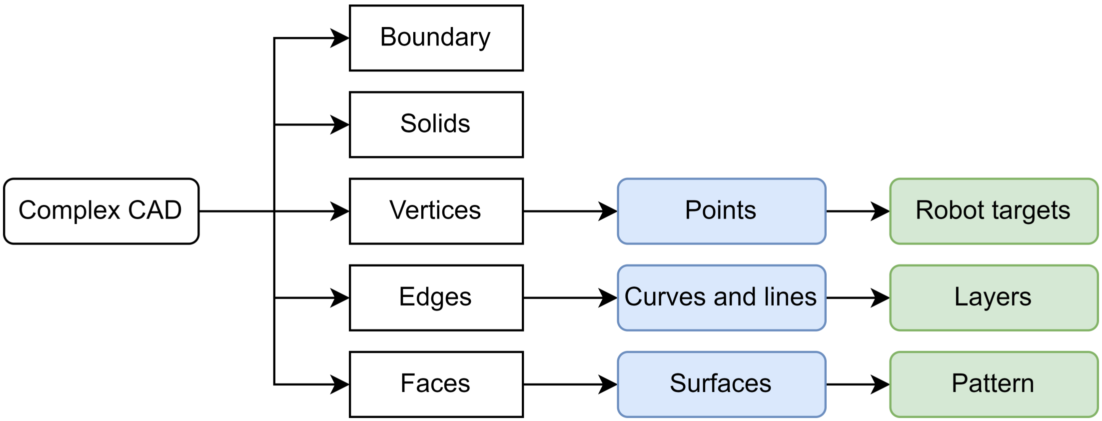

Figure 2.11: Parametrization flowchart for complex objects.

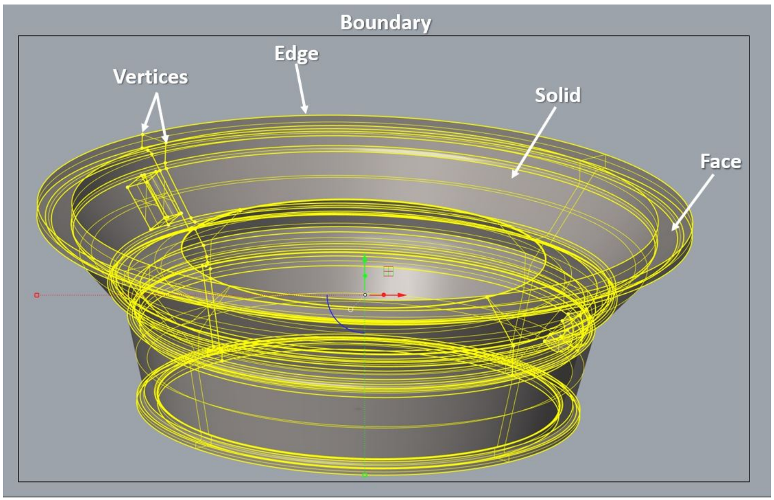

Figure 2.12: CAD Parametrization (3D model provided by SAFRAN Aircraft Engine under FAFil INTERREG project).

The deposition parameters for printing the complex model using LWAM are summarized in Table 2.3. Furthermore, Figure 2.13 shows the final results of the printed model using the proposed Parametric Modeling approach. The result shows a good match between the given 3D model of a complex object and the final metal product.

Table 2.3: Case 3: Complex model deposition parameters.

Power (W)	Travel speed (m/min)	Wire-feed rate (m/min)	Number of passes	Number of layers
2700	2.0	2.2	2	56

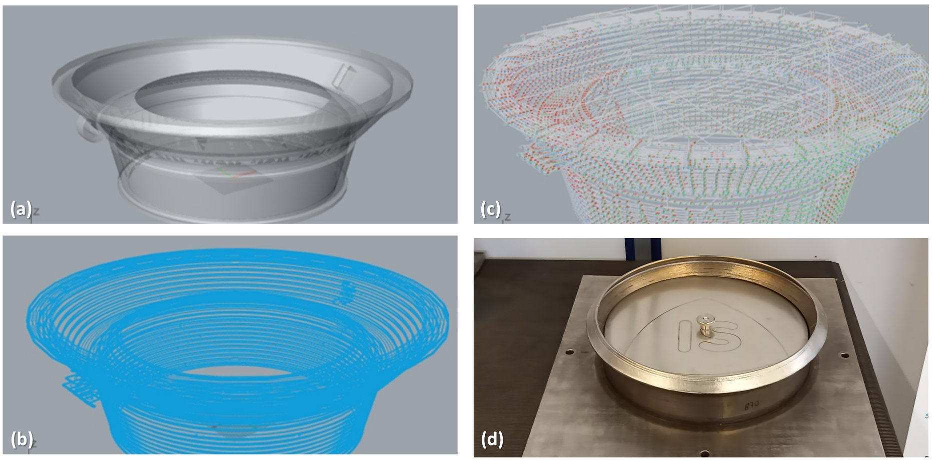

Figure 2.13: Case 3 (a) complex 3D model object, (b) complex model pattern creation, (c) complex model points creation, (d) printed metal complex object output.

2.4 Summary

In this chapter, a novel Parametric Modeling approach was developed for the LWAM process. The goal of the proposed approach was to use parametric design features to simulate 3D deposition paths for printing large scale metals using LWAM technology. The proposed approach includes a pattern creation and robot targets assignment while considering several deposition parameters and process requirements.

The experimental results show that the developed Parametric Modeling approach is capable of printing large scales parts using an automatic layer-by-layer deposition process without the need for using G Code. The results were conducted using three different cases namely, a wall, a hollow cylinder and a complex model.

For each case, the results show that the approach is feasible, adaptive, and is able to print precise 3D metallic objects using the LWAM process.

In summary, the main contribution is this chapter are the following:

- **1.** The development of an interactive framework where a product can be designed and modified without disrupting the deposition process.
- **2.** The robot system (frames) and deposition rules (process parameters and sequences) can be included easily in the LWAM process knowing the deposition requirements.
- **3.** In this approach, no external software to approximate the robot program for the entire deposition process using a robot.

The parametric approach will be used to 3D print metallic parts in the following chapters.

Chapter 3

Bead Geometry Prediction

3.1 Introduction

Laser Wire Additive Manufacturing (LWAM) uses a metal wire feed-stock and a laser source to create the molten pool, as shown in Figure 3.1. The LWAM needs a shielding gas shroud to protect the deposition from contamination. The process planning, the deposition strategies and the combination of parameters are important factors of the LWAM process. The process parameters (laser power, travel speed, wire feed rate) directly influence the layer geometry that will later define the final product creation. When the bead geometry composed of the bead height and width is well-defined, it improves the part's surface quality and the geometric accuracy of the product [47]. Figure 3.2 shows the flow path of printing for the LWAM. In the prediction model developed for the LWAM process, the choice of process parameters will be more accurate and optimized to improve product quality and productivity. Furthermore, the tool's path can be adapted

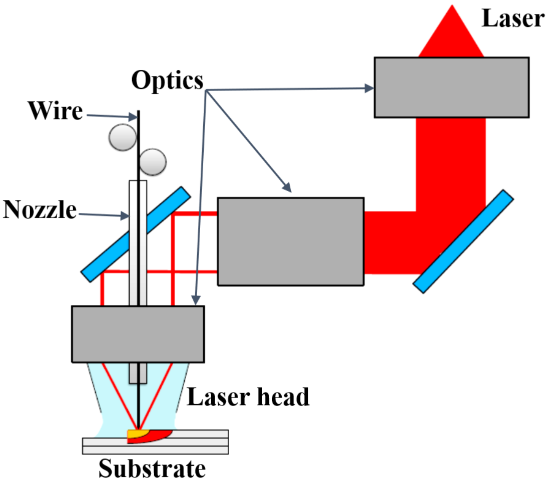

Figure 3.1: The LWAM schematic diagram [1]

using the prediction model. Two approaches can be used to address the issues related to the layer-by-layer deposition process. The first approach is numerical and uses experimental processes. The second approach employs multiple sensors to monitor and sometimes control the main deposition process parameters such as the laser power, the wire feed rate, advanced speed, or other parameters interfering during the printing process. This approach commonly uses sensors like pyrometers or camera vision systems to observe features such as layer height, melt pool characteristics, temperature etc.

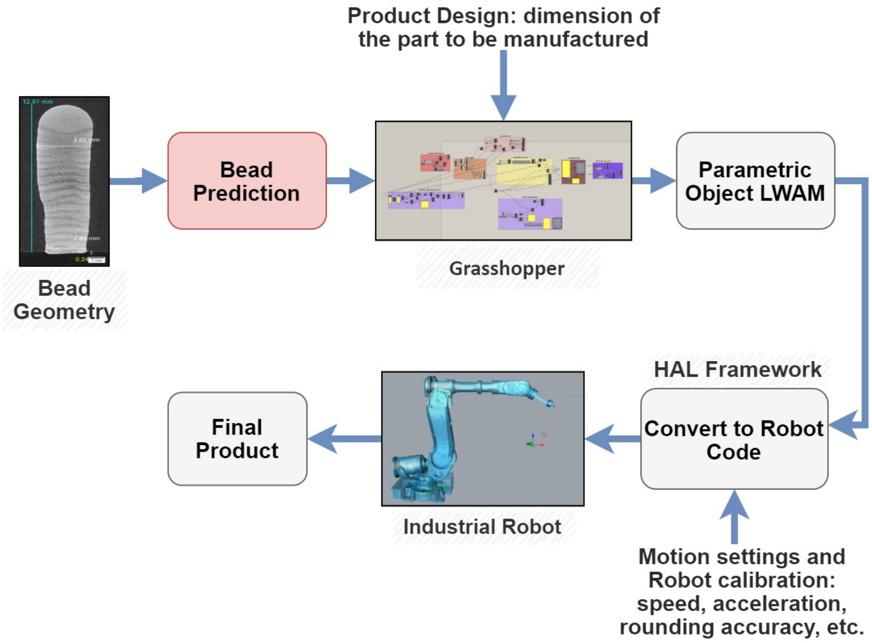

Figure 3.2: Flowchart diagram of the proposed approach for the LWAM system.

Different researches can be reported [48–57]. Mazumder et al. [58] analyzed the influence of independent parameters on the fabricated parts. Photodetector signals were used with a feedback controller. The obtained results showed a good surfaces roughness on the produced part by an average of 14 to 20%. Bi et al. [53], studied the influence of different process control strategies on the microstructure, the dimensional accuracy and hardness of the final part. An infrared (IR)-temperature is used to obtain the melt pool signal and connected to a Proportional Integral Derivative (PID) controller to regulate the laser power. The results show that a constant laser power in the process provides slightly better quality on the deposited parts. Toyserkani et al. [55] developed a feedback control system to enhance the deposition quality. A CCD camera is used to get melt pool images. A pattern recognition algorithm extracts the liquid/solid interface dimensions and the height in real-time. A PID controller is developed to adjust the laser pulse energy. The results showed an improvement and disturbances rejection around the operating points.

Cheng et al. [59] presented a closed-loop control model to measure the defects on the final part. A CCD camera with a Gaussian function is used as a shape descriptor to take the physical characteristics of the surface layers. The results show good reconstruction and detection of the surface shape patterns. Heralić et al. [60] developed a monitoring system to control the bead height and width in real-time. A laser line associated and two cameras are combined with an integrated PI controller and a feed-forward compensator. The laser power and wire feed rate are used as control signals. Doubenskaia et al. [61] investigated the impact zone of laser light during the deposition process. A bicolor pyrometer measured the temperature and a CCD camera integrated with a PHENIX PM-100 machine monitored the thermal radiation. The experimental results showed a sensitivity of the recorded signal to the variation of the process parameters.

Xiong et al. [62] developed a real-time measurement for the bead geometry (width and height). Two cameras are used to capture the images, a Gaussian filter to remove noises, a Sobel operator to detect the edge of the bead. Finally, a Hough transform algorithm is employed for curve fitting. Ocylok et al. [63] investigated the influence of process parameters on the melt pool geometry. A camera is used to measure the melt pool's area, length, and diameter at different process parameters. The obtained values are compared with the cross-sections and the laser spot diameter. An analysis software performs the calculation for each of the images. The experimental results show that the camera could detect process parameters that influence the melt pool size and provide accurate information.

Grobert et al. [64] employed a methodology to detect discontinuities in the deposition. A high-resolution digital single-lens reflex camera collects multiple deposition images. A computed tomography scan is used to label each layer. The images generated allow identifying porosity, fusion and inclusions. The experimental validations reveal that the camera-based system can detect deposition irregularities. Clijsters et al. [65] used online monitoring to estimate the deposition's quality. The system comprises a photodiode and a high-speed near-infrared (NIR) thermal CMOS camera. The experimental results show that the developed system can follow the melt pool variations, thus defects in real-time.

In [66], Xiong et al. presented a vision-based system that adjusts the wire feed rate in layers. A camera with composite filters is mounted to a robot, and a PID controller adjusts the wire feed rate. The experimental depositions of thin-walled showed acceptable results. Most of the cited related works faced variations and process uncertainties during the deposition process. The sensors usually delayed acquiring information in the melt pool and during data transmission between the controller. Another constraint is observed when the hot melt pool emission trouble the sensing device's functioning. This adds complexity to the information acquisition, thus augmenting the complexity. That is why most validation is performed on one line deposition, focusing on only one process parameter variation [67, 68].

Alternatively, the mathematical and the numerical approach employs simulations or generic equations to study the different deposition scenarios to observe the influence of the layer geometry on the final part [1, 69–73]. Zhu et al. [74] studied the influence of the laser power and the defocusing distance to improve the surface quality during the deposition process. The laser power was decreased at each layer to reduce the pool size change and avoid energy accumulation. This approach gave irregularities in the top layer while the defocusing distances were changed and were caused by fluctuating parameters and the system error. The height difference observed between layers propagated to the other layers and became very visible and affected the final part when it is not solved. Hence, there is a necessity for self-regulating the layer height. Donadello et al. [34] proposed a reconstruction of the spatial map of the layer height by investigating the variation of the layer thickness, which needs adjustment to satisfy the process's growth. It was found that a self-regulating mechanism occurs after an initial transient time that shows a fast deposition growth in the first layers and a decreasing trend after the initial layers until a steady-state is reached. This represents an equilibrium condition. The self-regulating mechanism happening during the deposition process is evident although there are disturbances coming from the system's error. Therefore, the layer thickness should be predicted in advance to solve and regulate those process parameters occupying a primary level in the 3D printing process.

In summary, the presented literature showed a lack of adaptive solutions to solve the layer issue in the additive manufacturing process.

Machine Learning (ML) has been applied in many fields today. Many new challenges exist in the industrial sectors, and complex problems are yet to be addressed. The efficiency of the ML is validated in many areas where physical models are hard to determine. The Neural Network (NN) algorithm is one of the most used ML approaches because it uses advanced algorithm structure [75]. NNs can also be used as supervised ML or unsupervised learning problems for problems with highly nonlinear relations. The NN architecture consists of the input layer, an output layer and a hidden layer [76]. The layers consist of neurons or nodes. In [77], Khatir et al. developed an improved artificial neural network (ANN) with an arithmetic optimization algorithm (IANN-AOA) for damage quantification problems. Functionally graded material plates are used to apply free vibration and damage identification. In [78], an ANN is used to identify damaged laminated composite structures. The network is trained using a fast convergence speed of gradient descent techniques in this approach. The global search capacity of evolutionary algorithms (EA) is used to guarantee the best possible solution quickly. Finally, a modified transmissibility damage indicator using local frequency response ratio (LFCR) is implemented in Zenzen et al. [79] work. Moreover, the location and size of damage in composite structures are detected using an ANN with reduced collected data for fast prediction and high accuracy.

Recently, to address issues relating to deposition accuracy, machine learning approaches are applied [80–85]. A second-order regression with a neural network is used by Xiong et al. [80] to predict the bead geometry in wire and arc additive manufacturing (WAAM) and to study the relationship between the bead geometry and the process variables. A roughness measuring method is developed in Xia et al. [82] for arc additive manufacturing using a laser sensor-based approach and other machine learning models. A back propagation neural network model is used by Nagesh and Datta [81] to estimate the bead geometry for tungsten inert gas (TIG) welding process. A first-order parameters is used by Milhomme et al. [83] to identify the correlations between the final geometry of Ti-6Al-4V beads and the input parameters and for the laser metal powder deposition process. Finally, the use of an artificial neural network (ANN) was investigated by Karmuhilan and Kumarsood [84] to predict the bead parameters based on some process parameters in Wire Arc Additive Manufacturing WAAM process.

It is observed from the state of the art that the machine learning approach, particularly the NNs, have not been applied to the LWAM for bead geometry prediction while considering the deposition parameters, which have a huge influence on both the bead width and the height of the final part. The complexity of the layer deposition stability and the high speed of the LWAM process is one reason why the study was not done previously.

In this chapter, the goal is to provide a machine learning approach employing a regression algorithm to predict the layer geometry in the LWAM process. Many experiments were performed, and the developed model predicted the height, width, and ratios for upcoming layers. Also, the influence of the deposition parameters (laser power, wire feed rate, and travel speed) on the final geometry is discussed using the neural network model.

The parametric approach presented in chapter 2 is used to implement the prediction algorithm. As a reminder, the parametric approach created generate a robot program for LWAM process for a digital CAD part. This approach is employed for the flexibility in the design, the path pattern design and the control of other parameters affecting the deposition quality.

The prediction model can help choose the process parameters and optimize them to improve the surface quality of the produced part. In summary, the prediction model leads to better quality products and avoid time loss.

The chapter is structured as follows, section 3.2 introduces the methodology; Section 3.3 presents the prediction model. Section 3.4 presents the experimental results and discussion. The chapter finishes in Section 3.5 with a summary.

3.2 Methodology

The bead geometry dimensions of layers have been obtained in this work. Grasshopper was used to create them parametrically. Grasshopper uses a generative algorithm and a parametric modeling method different from standard CAD software that uses a polygon-based approach. Rhino-Grasshopper was used to create the objects (bead geometry dimension, layer height, pattern, etc.) and the generative algorithms were used to create and convert toolpaths to robot programs with the intermediate of HAL framework. This approach is used because of the suitable programming methodology interface that uses mathematics and logic to create parts without using the G-Code [45]. The 3D product creation is divided into the following steps:

- Parametric Surface Creation: where a 2D cross sectional surface is created using mathematics and logics. On the other hand, a CAD part can also be imported directly and converted to a parametric CAD part using Grasshoppers tools.
- Pattern creation: where path patterns are created and added to the 2D cross sectional surface.
- Layer-to-layer deposition strategy: In this step, a suitable travel strategy from layer to layer is defined. The travel strategy depends on the process parameters such as the laser power, wire feed rate, and robot travel speed. The travel strategy needs to be carefully defined because it influences the cooling of the deposited layer, as well as the bonding between layers [86,87].
- Bead geometry measurements: In the end, a laser scanner is used to obtain the the bead geometry profiles during the LWAM process. The laser scanner is mounted on the robot tool to measure the bead geometry features for each layer deposition. A measurement for a single bead geometry and layer

deposition is shown in Figure 3.3.

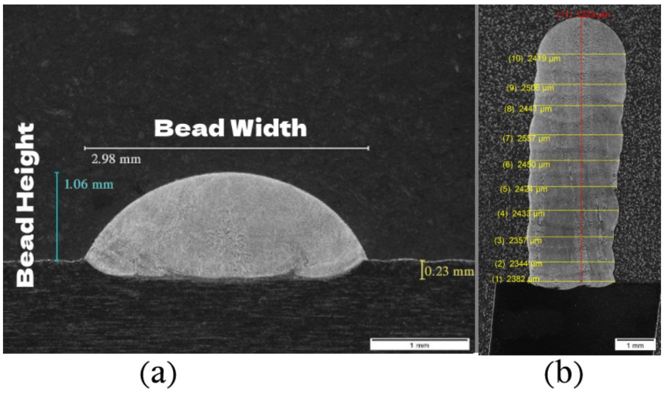

Figure 3.3: (**a**) Bead geometry measurements. (**b**) Layer deposition measurements.

After measuring the bead geometry dimensions, a regression algorithm predicts the bead geometry for the current and successive layers. The prediction function $F(x)$ is implemented in Grasshopper along with the product design specification, bead geometry dimension, and toolpath pattern. Then, the parametric object is converted to robot programs using HAL framework. The robot system, the process parameters and the deposition sequences are finally included. In the end, the final object is simulated virtually and transferred to the real robot to manufacture the 3D part. An overview of the created approach is shown in 3.2.

To create the prediction model, a linear regression and linearizations of the non-linear trend (power decay function) are used. A power decaying function is used to show the self-regulation of the layer geometry. The input of the prediction model is the training examples (x_i, $i = 1$ to m, $m =$ final layer geometry dimension) and the output is the prediction function showing the bead geometry changes over the layers.

The relation between the bead geometry measurements and the first-order deposition parameters: laser power, wire feed rate, and travel speed was determined using the neural network technique. The prediction algorithm (presented in Section 3.3) was used with the fixed deposition parameters first, and thereafter the neural network (discussed in Section 3.3.2) was applied with varying the deposition parameters to study their influence on bead geometry.

3.3 Prediction Model

The regression algorithm used in this work is a supervised-learning algorithm. Supervised learning predicts the bead geometry for deposited sample data. Supervised learning is perfect for problems where it is obvious to find a closed-form solution between the outputs and the inputs. The geometry prediction problem is a regression problem in which the mathematical function is derived from a training set.

For this work, a power decay function represents the prediction function and resolves the self-regulation mechanism happening during the deposition process. Also, the bead height, the width and width-height ratio are obtained for different deposition parameters (scenarios). In this section, the bead height prediction equations are presented since the same algorithm and technique are used for all prediction models.

3.3.1 Bead Height Prediction Model

The prediction algorithm starts with creating and saving the training examples (x_i, y_i), $i = 1$ to $m, m =$ which is the final layer in a dataset. x_i is the input variable or the number of layers often called the input features, and y_i is the output variable or layer height that needs to be predicted often called the target variable.

The prediction function $F(x)$ is the output of the regression. This function relates to the evolution of the bead height over layers. $h(x)$ represents the hypothesis of the linearized training set. $F(x) = a * x^b + c$; and $h(x) = \theta_0 + \theta_1\ x$.

The algorithm is created in Python and consists of the following steps: First, the training set is plotted to see the evolution trend of the bead geometry over the layers. Second, a decreasing concave up power trend: $a * x^b + c$; is created to represent a mapping function; a and $c > 0$; $b < 0$; a is the vertical stretch of the function, b is the rate of decay of the function and c the horizontal asymptote of the function. Third, the training set is linearized using natural logarithm and plotted. After that, a least-squares optimization is used to fit the natural logarithm plot (linearized model) where a linear regression algorithm is applied.

In the end, the optimization problem gives the parameters θ_0 and θ_1 of the hypothesis function $h(x)$. Finally, the power decay function is derived to create the layer prediction function where a is exponential of θ_1, b is θ_0, c is the horizontal asymptote.

The bead height prediction process is shown in Figure 3.4.

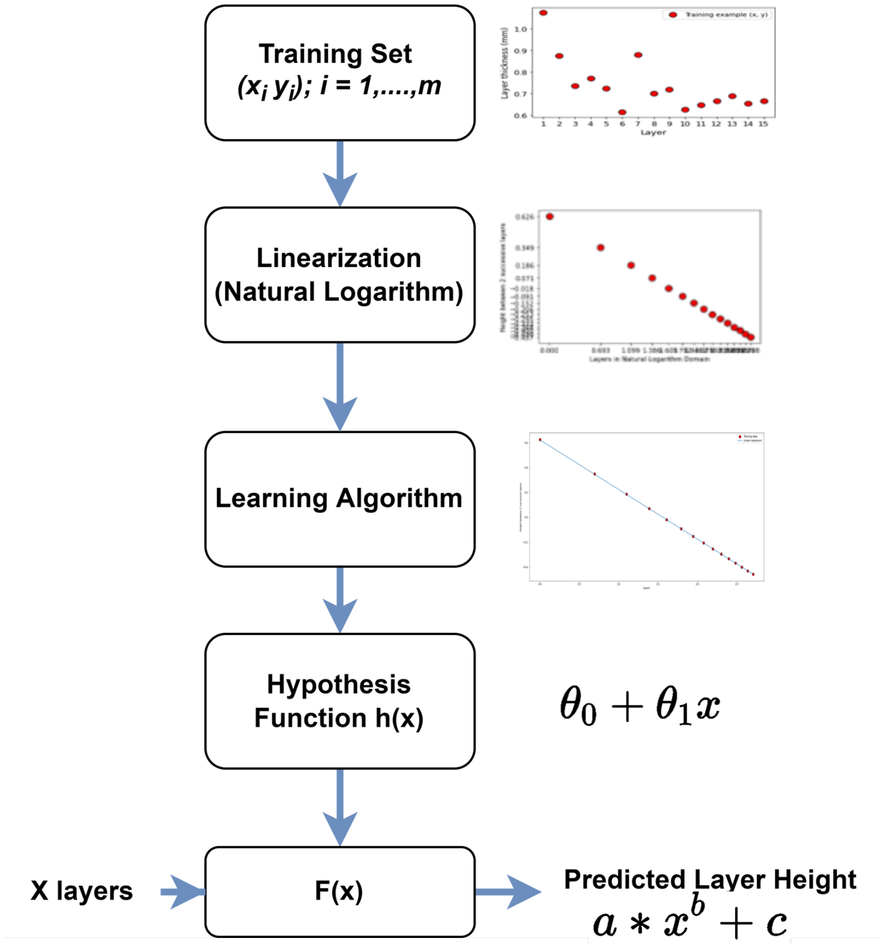

Figure 3.4: Bead height prediction process.

The following linear equation represents the linear model.

$$h(x) = \theta_0 + \theta_1 x \tag{3.1}$$

where $\{\theta_j; j = 0, 1\}$ are unknown variables. Thereafter, the cost function $J(\theta)$ is set up as follows:

$$J(\theta) = \frac{1}{2}\sum_{i=1}^{m}(h(x_i) - y_i)^2 \tag{3.2}$$

where $\{x_i, y_i; i = 1, \ldots, m\}$. After, θ is selected to minimized the cost function $J(\theta)$. A search algorithm called *gradient descent* is used.

$$\theta_j := \theta_j - \alpha \frac{\partial}{\partial \theta_j} J(\theta) \tag{3.3}$$

This update is performed simultaneously for all values of $j = 0, \ldots, n$, and n is the number of unknown variables. The *learning rate* (α) technique is used so that when the learning rate is decreased, the regression algorithm converges to its global minimum rather than oscillating around the minimum. To obtain a reasonable learning-rate value, tuning experiments is performed. The partial derivative of $J(\theta)$ gives the least-mean-squares (LMS) update also known as the Widrow–Hoff learning rule, which is defined as follows:

$$\theta_j := \theta_j + \alpha \sum_{i=1}^{m} (y_i - h_\theta(x_i)) x_{i,j} \quad \forall j \tag{3.4}$$

The learning rates and the number of iterations were chosen to converge to the best gradient descent values. When the output model is not good, either the number of iterations or the learning rate is changed or the mapping function parameters are changed. The prediction process is described in the flowchart shown in Figure 3.5. The number of iterations is from 1500 to 2000, and the learning rate is 0.03 in this work.

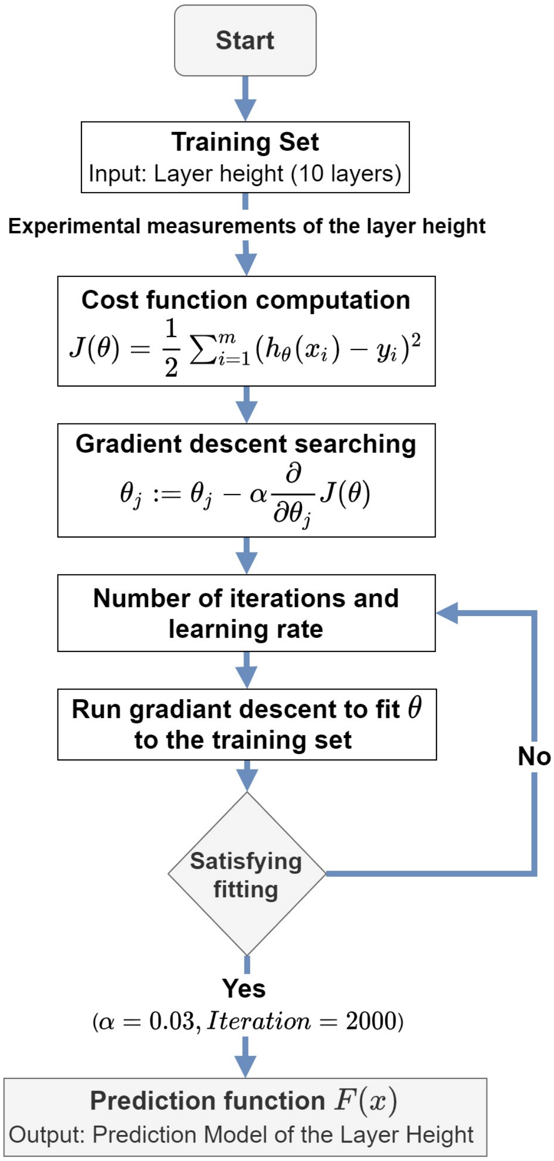

Figure 3.5: Flowchart of the bead height prediction model.

3.3.2 Neural Network Prediction

In this seciton, a neural network is used to study the correlations between the dispositional first-order parameters which are the laser power, the wire feed rate and the travel speed) and the geometrical bead measurements (height and width) in the LWAM process. The neural network is trained using the Levenberg–Marquardt algorithm (LM) and to solve the optimization problem [88].

The LM algorithm works with loss functions that take the form of a sum of squared errors. The exact Hessian matrix is not solved in the LM algorithm. Instead, the gradient vector and the Jacobian matrix [89] are used. The LM algorithm computation is presented in this subsection.

The following loss function which takes the form of a sum of squared errors is considered,

$$f = \sum_{i=1}^{m} e_i^2 \tag{3.5}$$

where e_i^2 is the error between the estimated output (prediction) and the training set, and m is the number of training samples. Thereafter, the Jacobian matrix of the loss function with respect to the parameters is defined,

$$J_{i,j} = \frac{\partial e_i}{\partial w_j}, \quad i = 1, \ldots, m, \ j = 1, \ldots, n \tag{3.6}$$

where w_j is the weight applied to the neuron's input to produce the output, m is the number of samples in the data set and n represents the number of parameters in the neural network. After, the gradient vector of the loss function is computed as,

$$\nabla f = 2J^T \cdot e \tag{3.7}$$

where e is the vector of all error terms. After, the Hessian matrix is approximated with the following expression,

$$H_f \approx 2J^T \cdot J + \lambda I \tag{3.8}$$

where λ is a damping factor that guarantees the positiveness of the Hessian and I represents the identity matrix. Finally, the parameters improvement process with the Levenberg–Marquardt algorithm is defined as,

$$w_{(i+1)} = w_i - (J_i^T \cdot J_i + \lambda_i I)^{-1} \cdot (2J_i^T \cdot e) \tag{3.9}$$

for $i = 0, 1, \ldots, m$, were w is the parameters vector. The parameter λ is initialized to be large to make the first updates in small steps towards the gradient descent direction. When the iteration results in a fail, the λ is increased by some factor. As shown in the following, this method gave pretty good results for finding the relations between the bead geometries and the input parameters.

3.4 Experimental Results

For the three cases, experimental tests were performed on the laser platform at Institut de Soudure. A robotized laser wire-feed system ran tests. An ABB 6-axis poly-articulated robot is used to provide the kinematics of the process. A fiber laser source called IPG Photonics with a power of 10 kW was used. A CoaxPrinter laser head is used to deliver the laser beam and the wire. Figure 3.6 shows the actual LWAM system setup.

Grasshopper was used to create the physical part specifications (bead geometry dimension, layer height, pattern, etc.) to perform the experiments. A generative algorithm was created in Grasshopper and converted to robot programs using the HAL framework. A hollow wall of 150 mm × 50 mm was deposited and the deposition path was created using the parametric algorithms.

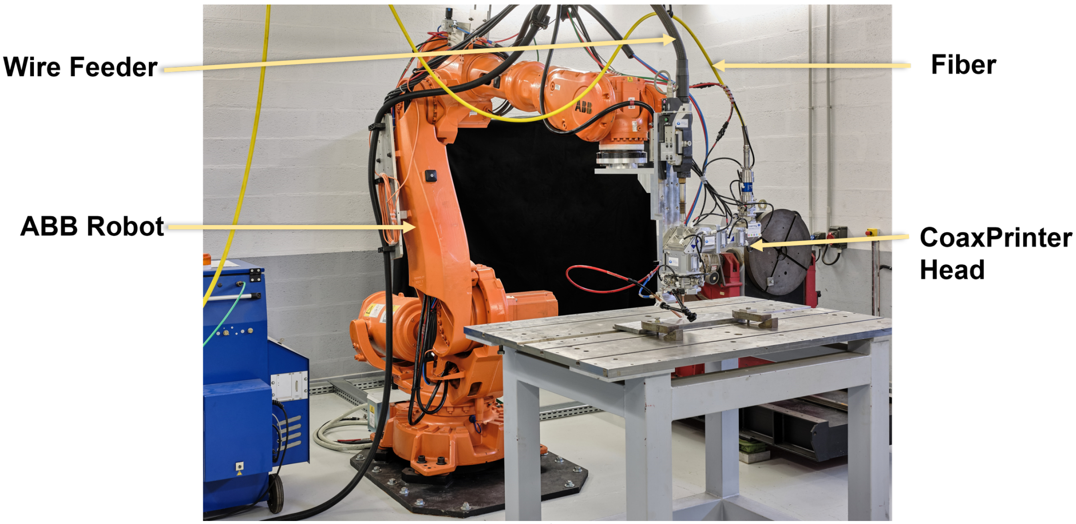

Figure 3.6: Experimental Setup of LWAM platform at Institut de Soudure.

3.4.1 Bead Geometry Prediction

The prediction algorithm proposed in Section 3.3 is tested for a hollow wall of dimension 150 mm × 50 mm with 15 layers was deposited using the following process parameters: laser power = 1.4 kW, wire-feed rate = 1.4 m/min, and travel speed of robot = 0.45 m/min. The process parameters are selected to achieve a uniform, stable and homogeneous final product, as shown in Figure 3.7. Figures 3.8 and 3.9 represent the results of the prediction model height and width respectively. In the figures, it is shown the prediction results for both the training

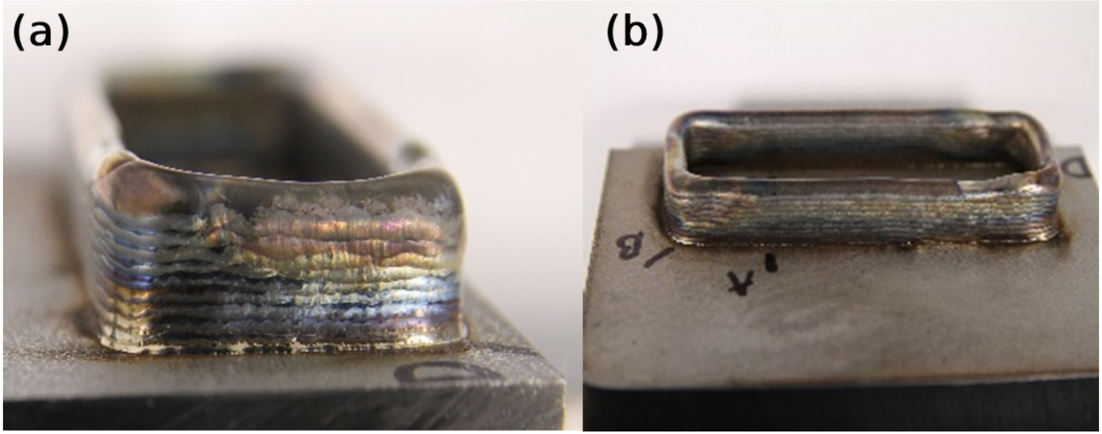

Figure 3.7: Experimental layers deposition; (**a**) front view, (**b**) side view.

data set (layers 1 to 10 — red circle) and the prediction data set (layers 11 to 15 — black circle).

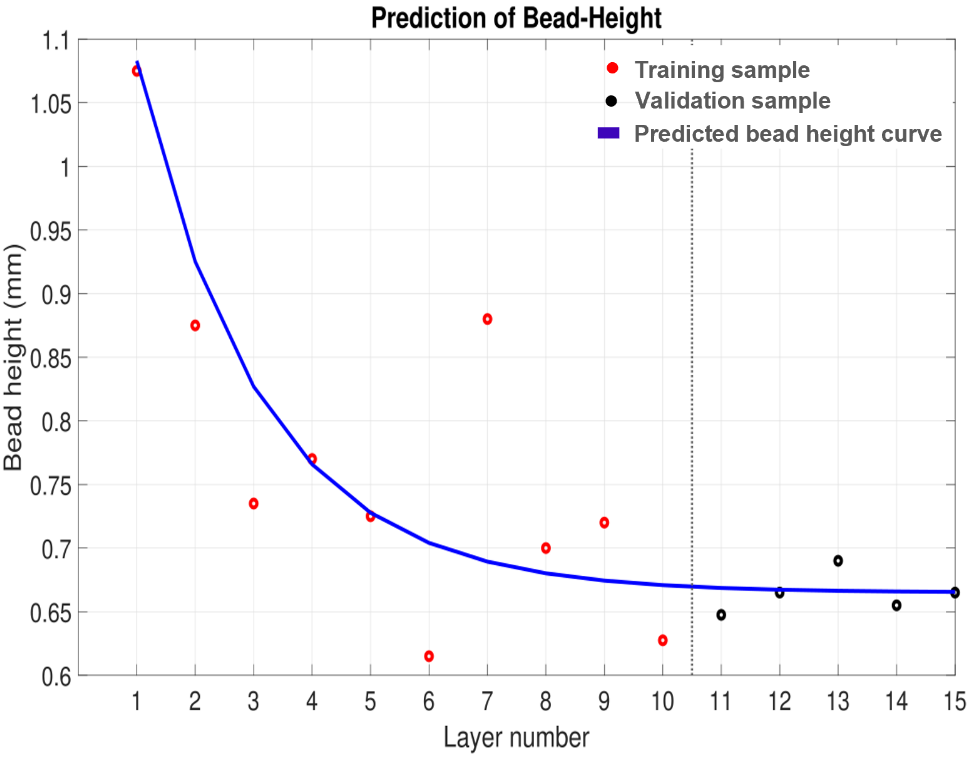

Figure 3.8: Result of the bead height prediction.

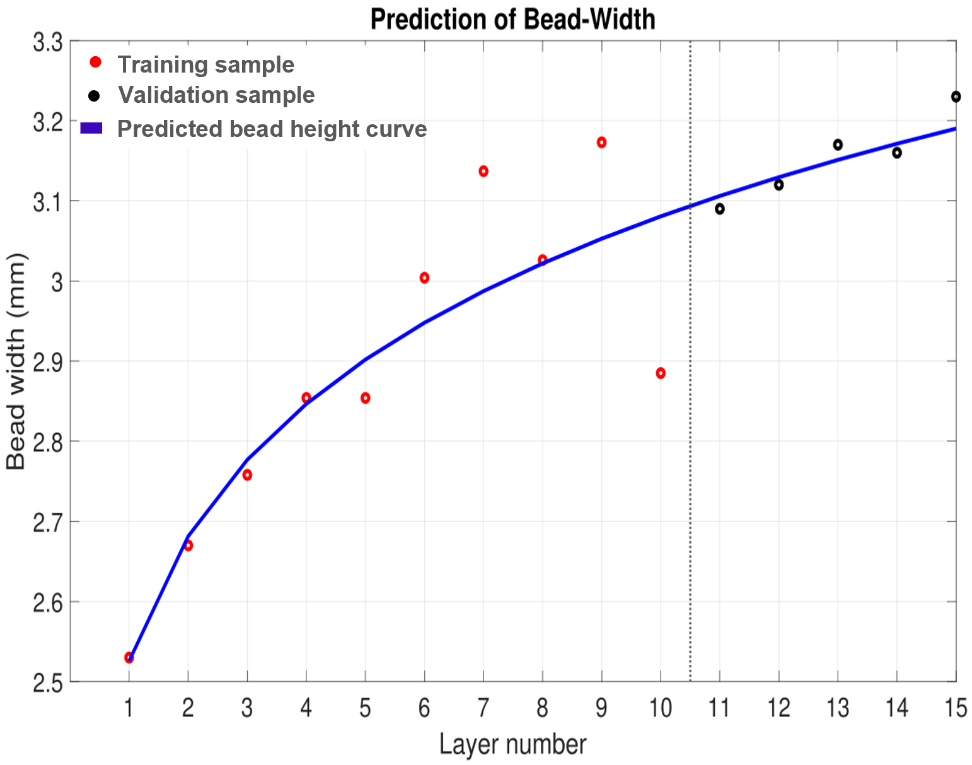

Figure 3.9: Result of the bead width prediction.

The plot of the training set in Figure 3.8 shows a power decay trend of the height evolution across the layers. This observation is the so-called the self-regulation mechanism of the layer height, and was been discussed by Simone Donadello et al. in [34].

In the figure 3.10 the bead-width-over-bead-height ratio across layers is shown. From the experimental results, a logarithmic increase is observed across layers. In the observation, the width-to-height ratio increases significantly across the first layers before reaching a threshold around layer 10.

The prediction ratio shown in Figure 3.10, interestingly indicates that the bead width increasing ratio is significant compared with bead height change over the layers. Here, the physical phenomenon observed is due to the conduction of heat resulting from the laser-matter interaction. When the wire is irradiated by the laser beam, the energy absorbed by the wire creates a molten pool deposited on the substrate. As the beads are added over the layers, the heat source “moves away” from the substrate. Consequently, the volume of material allowing the transfer of heat is decreased. This increases the flux density, which leads to local

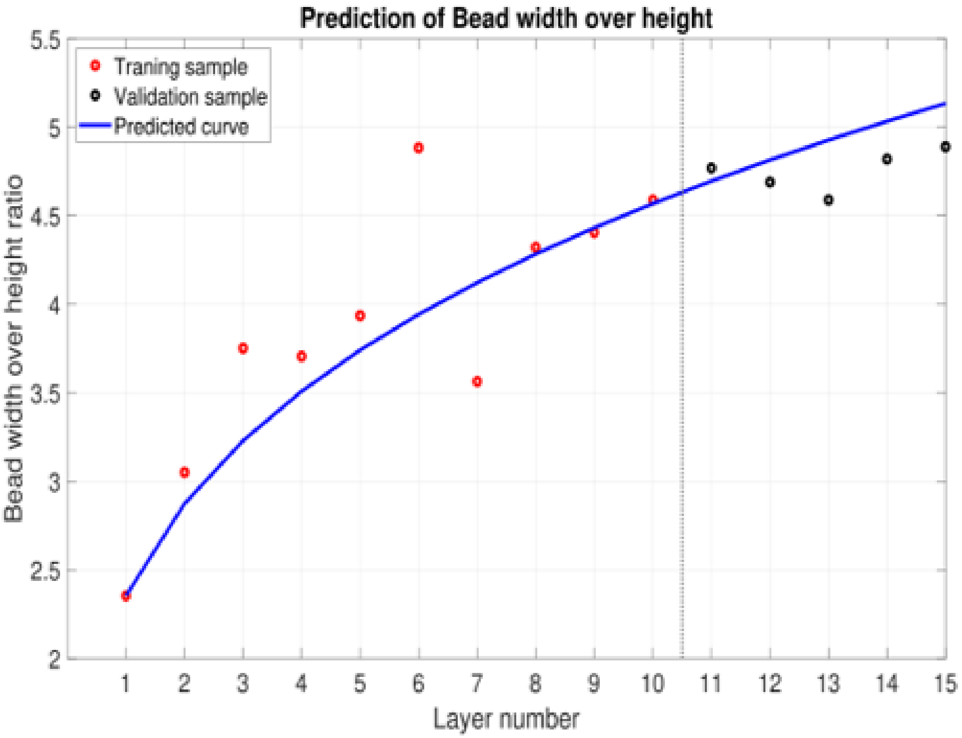

Figure 3.10: Bead width over height prediction.

heating, the wetting of the deposit, and a modification of the local properties of the metal, among other things. The spread of layers becomes significant with the increase of bead widths and the decrease of the bead height. This phenomenon stabilizes after a number of deposited layers, as shown Figure 3.11.

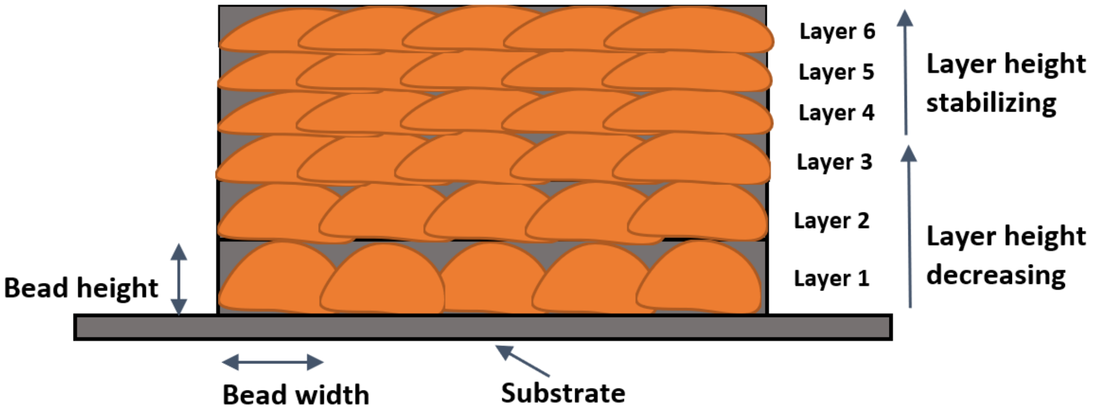

Figure 3.11: Schematic diagram of bead width and bead height for different deposited layers.

3.4.2 First-Order Deposition Parameters

The effectiveness of predictive models is investigated using neural network (discussed in Section 3.3.2). Many experiments with the three deposition parameters were carried out. As discussed before, the deposition parameters are the laser power (P), the wire feed rate (F), and the travel speed (V), as presented in Table 3.1.

Table 3.1: First-order deposition parameters.

Test Trial	**P (kW)**	**V (m/min)**	**F (m/min)**
Sample 1	1.6	0.6	2.0
Sample 2	1.6	0.3	2.2
Sample 3	2.0	0.9	2.2
Sample 4	1.6	1.2	2.2
Sample 5	1.4	1.4	0.45

The five sets of parameters choice come from a test campaign for the development of the process with a wire of 1.2 mm diameter in Inconel® 718 [90]. These five sets of parameters define the stability domain of the process, i.e., they allow the creation of stable deposition with different bead morphologies, which is the concern for this study. Figure 3.12 shows the different bead geometry morphologies for each parameter variation in the experimental design and each sample, 10 layers were deposited and measured (70% training data, 15% validation data and 15% as testing data).

The Levenberg–Marquardt algorithm (LM) is then used to see the influence of the deposition parameters (P, V, F) on the bead geometries (bead height and bead width). The LM parameters are the number of hidden layers and nodes. A single hidden layer was chosen with a size of 10 nodes (for more details, see, e.g. [82]) for a good predictive performance. 100 iterations for each sample were also used to obtain the other parameters using trial and error. Figure 3.13 illustrates the correlation between the measured height and the width predicted by the LM approach for the different deposition parameters.

The points shown in Figure 3.13, are scattered around the fit line (represents measured bead geometry). This indicates the correlation between the model output values and the actual values. The value of R^2 is the correlation between the model prediction (y^p) and the corresponding target (y^e). The value of R^2 is between 0 and 1, and if R^2 is equal to one, a perfect correlation is obtained. R^2

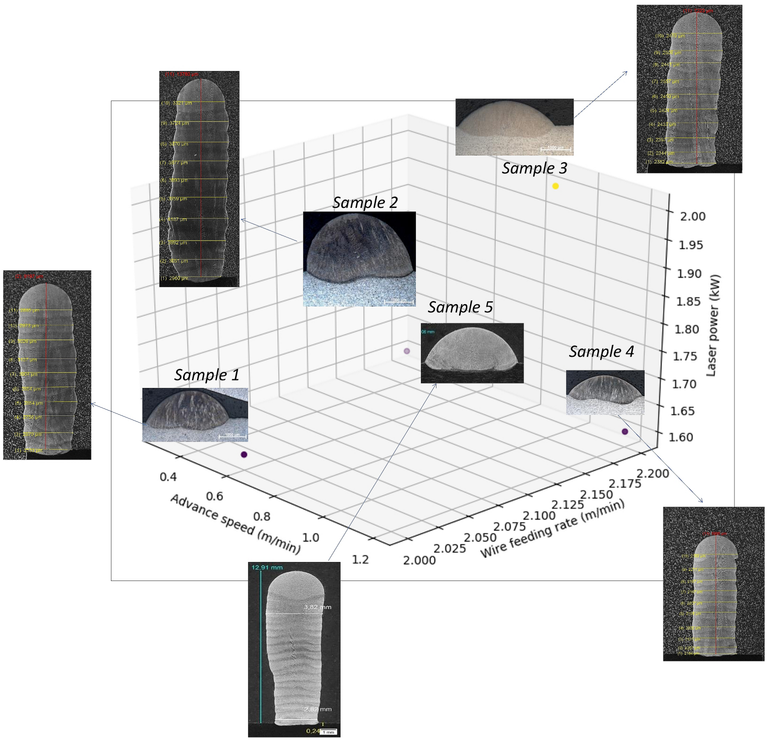

Figure 3.12: Bead geometry samples. source: Institut de Soudure

is computed as follows:

$$R^2 = 1 - \frac{\sum_{i=1}^{n}[y_i^p - y_i^e]^2}{\sum_{i=1}^{n}[y_i^p - y^m]^2}, \quad y^m = \frac{1}{n}\sum_{i=1}^{n} y_i^p \tag{3.10}$$

where n is the number of the experimental data. The prediction model's accuracy is evaluated for each sample with the computaion of the RMSE, MAE and MAPE. The prediction accuracy of the regression model is perfect for an RMSE, MAE and MAPE of 0.

RMSE measures the standard deviation of residuals.

$$RMSE = \sqrt{\frac{1}{n}\sum_{i=1}^{n}(y_i^e - y_i^p)^2} \tag{3.11}$$

MAE represents the average of the absolute difference between y^e and y^p values in the data-set.

$$MAE = \frac{1}{n}\sum_{i=1}^{n}|y_i^e - y_i^p| \tag{3.12}$$

MAPE is the MAE as a percentage.

$$MAPE = \frac{1}{n}\sum_{i=1}^{n}\frac{|y_i^e - y_i^p|}{y_i^e} * 100\% \tag{3.13}$$

The bead geometry prediction performance of different samples for the LWAM process is compared in Table 3.2.

Table 3.2: Model performance for different samples.

	RMSE		**R2**		**MAE**		**MAPE**	
Sample	**Height**	**Width**	**Height**	**Width**	**Height**	**Width**	**Height**	**Width**
1	0.0361	0.0337	0.9870	0.9894	0.0282	0.0082	2.8151%	0.8235%
2	0.0580	0.2053	0.9888	0.9242	0.0291	0.0301	2.9098%	3.0145%
3	0.0392	0.0154	0.9818	0.9652	0.0345	0.0037	3.4547%	0.3704%
4	0.0388	0.0094	0.9717	0.9300	0.0408	0.0030	4.0777%	0.2951%
5	0.0176	0.0258	0.9954	0.9947	0.0232	0.0047	2.3192%	0.4720%

Table 3.2 shows the comparison results. Sample 5 gives the best test trial as it shows good values of prediction accuracy measurements both for bead width and height. This result comes from the smooth thickness transition across layers and also the good distribution of the layer thicknesses provided by a high wire-feed rate with low power and travel speed compared with the other measured samples.

The worst performance is reported from Sample 2 showing the worst values of prediction accuracy measurements. Sample 2 has the highest RMSE, MAE and MAPE observed; however, the reported R^2 was good because R^2 gives an estimate of the strength of the relationship between y^e and the prediction curve $F(x)$. However, the value reported for this test does not explain the fitting explicitly. The other explanation of the obtained results from the distribution of the y^e in sample 2 shows a similar trend with the prediction curve, which does not fit the y^e values. The obtained prediction results indicated that high laser power and travel speed associated with low wire-feed rate give less desirable final bead geometry results.

The influence of deposition parameters on the prediction model and the bead geometry's accuracy are summarized in Table 3.3. The term "Acceptable bead prediction" in Table 3.3 represents the trend of the set of parameters with very good correlation coefficients (RMSE, R^2, MAE, MAPE). The designation "Good layer deposition" represents the experimental tests showing process stability (stable metal vapour plume, no stuck wire etc.) with a low laser power and travel speed associated with a high wire-feed speed.

Table 3.3: First-order deposition parameters.

Process Stability	**P**	**V**	**F**
Acceptable bead Prediction	Low	Low	High
Good layer Deposition	Low	Low	High

(Sample 1)

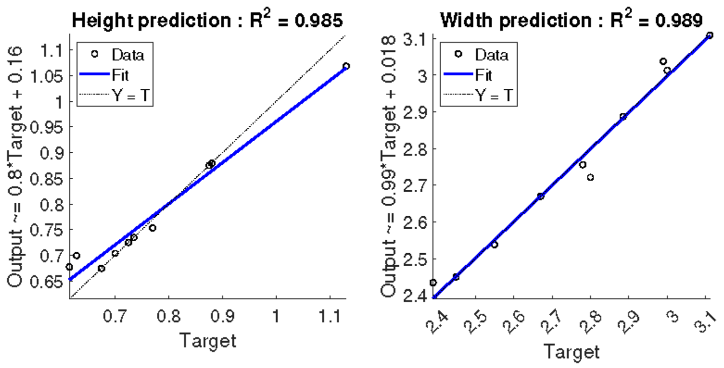

(Sample 2)

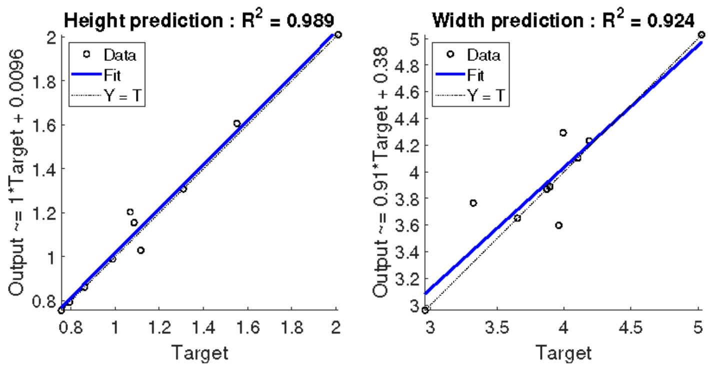

(Sample 3)

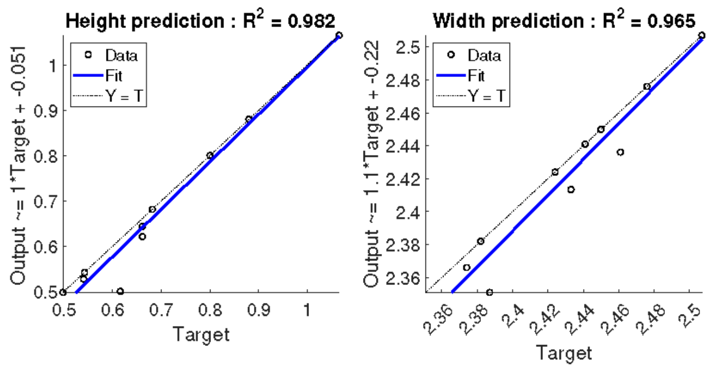

(Sample 4)

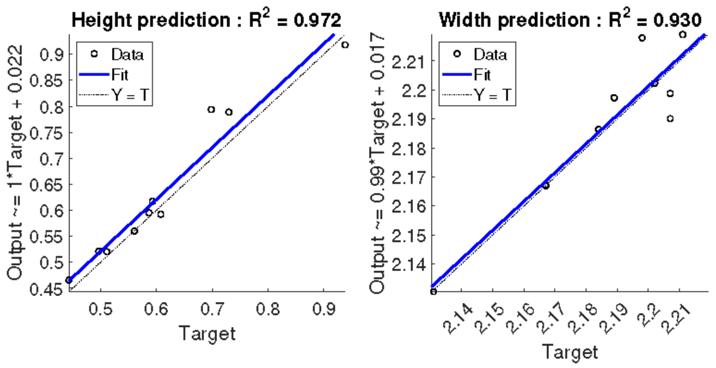

Figure 3.13: *Cont.*

(Sample 5)

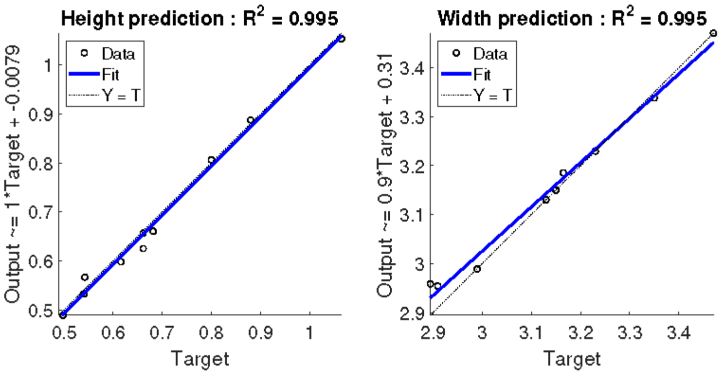

Figure 3.13: Regression plot for different samples prediction

3.5 Summary

In this chapter, a bead geometry prediction model for the LWAM process was created using a machine learning regression algorithm and neural network. The developed model predicted the bead height, bead width and the ratio therebetween. The results confirmed the profile's trend toward stable deposition. The prediction model is designed to be flexible and can be adjusted to follow the trends of various layer-deposition behaviours. The experimental results revealed that the developed machine learning model is capable of predicting the bead geometry for LWAM-deposited layers using Inconel 718 with acceptable error rates (i.e., 2∼4%). Several data samples have also been collected by a laser scanner to study the influence of different deposition parameters on the bead geometry. The obtained results showed that low power (P) and travel speed (V) with a high wire feed rate (F) gave better layer deposition and model prediction compared with other collected samples.

In the next chapter, instead of predicting the bead geometry, a physical model of the bead geometry will be created for the laser wire additive manufacturing process.

Chapter 4

Modeling of the Melting Pool

4.1 Introduction

Metal Additive Manufacturing (MAM) process development began in the late 1990s [29, 30]. The process consists of melting a wire or powder using an energy source to create a liquid melt pool bead. The beads are then added layer by layer to form the part. Today's application of the process can be found in the automotive sector, aircraft, medical implants, dental restoration, and even the fashion sector [2, 32, 33]. MAM integration in the industrial sector is still in process because of the complexity and the interference of highly sensitive parameters causing disturbances. A fluctuation of one process parameter such as the cooling rate, power, and speed can modify the melt pool shape, thus to the final part quality and integrity [27, 28].

According to different sources of energy used for metal deposition, MAM could be classified into Arc Additive Manufacturing (AAM), Electron Beam Additive Manufacturing (EBAM), and Laser Additive Manufacturing (LAM) [31]. With regard to the additive material form, Laser Additive Manufacturing could be divided into powder-based and wire-based Laser Additive Manufacturing. In this paper, we will focus on the Laser Wire Additive Manufacturing (LWAM) technology.

The process of LWAM consists of melting a wire using an energy source to create a liquid melt pool bead. The beads are then added layer by layer to form the final object, as illustrated in Figure 4.1.

To obtain a stable deposition process, reliable sensing, modeling and control

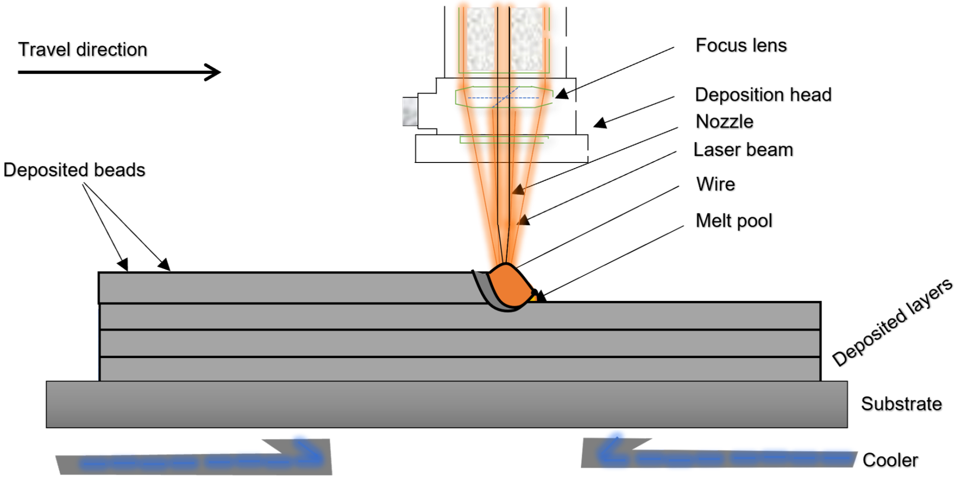

Figure 4.1: Schematic diagram for bead deposition process in the LWAM.

approaches are needed. Several methods, such as computational, empirical, and physical models are discussed in the literature. Several works are oriented on empirical, computational and numerical methods that can be reported such as [1, 91–102].

In Chapter 3, a model to predict bead geometry and improve deposition accuracy is created. A regression algorithm is applied to fit bead geometry with the main deposition process parameters (laser power, wire feed rate and advanced speed) and a neural network-based approach to study the influence of the parameters on the bead geometry. In [97], Magerramova et al. investigated body parts using computational and experimental methods. The Finite Element Method (FEM) was used in the Laser-Based Manufacturing (LBM) process to simulate gearbox housings and numerically optimize the product weight. The results show that the mass of body parts is reduced by up to 15% with the same strength properties. In [98], Liu et al. used a 3D microscale FEM with a powder arrangement system to simulate multi-layer powder stacking for Selective Laser Sintering (SLS). The model aimed mainly to investigate the thermal evolution of selective laser sintering using metal powders.

In [99], Fetni et al. developed an empirical model to study the impact of process parameters on the deposition. The thermal history and the melt pool dimension evolution of a 316L stainless steel reinforced by Tungsten carbides were studied using finite elements. The experimental analysis was correlated with the numerical results using experimental observations from light optical, scanning electron microscopies and thermocouple records. In [100], an empirical model of single bead geometry and the process parameters was developed. Linear regression was applied to fit the collected data using an optical profilometer. The response variables are the bead height, bead width, and angle of repose. The model showed the influence of the process parameter's interaction on the bead geometry. In [101], a Computer Fluid Dynamics (CFD) model with a discrete phase and fluid-solid coupling method is developed to study the influence of peening gas flow on the temperature field and powder trajectory. While in [102], Kiran et al. developed a thermo-mechanical weld model for 316L stainless steel. Their model estimates the residual stress for large parts. The results obtained are compared with the experimentally measured thermal field to validate the approach. In [103], a process map of single beads of Ti-6Al-4V was created using finite element analysis. The process is developed for the microstructure solidification in electron beam wire feed AM processes. In [104], Panagiotis et al. investigated finite element methods for modeling heat transfer analyses of metal additive manufacturing. While in [105], a finite element model is used to simulate the thermal and sintering phenomena occurring during the selective laser sintering deposition process. The model included the heat transfer coupling equation and the powder sintering equation.

The presented computational method work focused on the microstructures, heat transfer, and material properties. However, the computational method has its limitation as it is difficult to employ them for a control system design because of the complex partial differential equations. The drawbacks of the numerical and empirical methods are the need for several experimental tests to obtain response experiments and develop a reliable control model.

In all the cited works, the main limitations of empirical, computational and numerical models are large data management and long computation time. Also, the models are very limited and complicated to be employed for control system creation. Most of the time, the models need to handle multiple information. Therefore, an analytical model-based is required for process optimization as well as a stable and fast controller design. Few works can be reported, such as Yuze et al. [106], where the authors proposed an analytical method to predict the clad geometry and the catchment efficiency. The model couples the moving laser beam, the powder stream, the semi-infinite substrate with the heated powder spatial distribution, the attenuated laser power distribution, and 3D shape of the melt pool. Some years later, Yuze et al. [107] developed a physics-based model for melt pool dimensions: height, width, and wetting angle. The model was applied on single-track to multi-track and multi-layer deposition. The experimental validation showed good agreement at different levels of specific energy and powder feed rate for single-track simulation and good prediction of the dynamic height for 3D profile structures. However, some discrepancies between the model prediction and the experimental results were noticed. The differences came from the deviation of the powder feeding and the heat convection leading to oxidation in the process. In [108], the first analytical model for metal deposition was developed. The analytical model includes the material transfer phenomena and thermal transfer of the moving source. The model was derived from the molten pool's scalar mass, momentum, thermal conduction, and energy balances. Years later, Wang et al. [109] proposed an improved model based on Doumanidis et al.'s [108] work. The developed physics-multivariable model proposed a parameterization of the material transfer rate as a function of the process parameters, thus characterizing the steady-state melt-pool geometry.

This thesis proposes a complete physics-based multivariable model that describes the laser wire additive manufacturing process. The model's dynamic molten pool behavior includes material properties, process parameters, and thermal history. Further, the standoff distance was included in the model. A few works mention the importance of the standoff distance on the deposition process and the final part from the literature [74, 100, 101, 110, 111]. In [112], Pinkerton et al. [112] studied the role and effect of the standoff distance on the final part. Pinkerton et al. [112] produced some parts with variable standoff and compared their dimensions. In the results, the melt pool standoff distance induced changes in heat flow, powder flow, melt pool temperatures, powder assimilation sizes, and part growth. In summary, Pinkerton et al. [112] highlighted the relationship between the melt pool standoff distance and final part height. In [28], Sreekanth et al. studied the influence of some process parameters on the deposit geometry. It was found that the laser power and the standoff distance affect the width and depth of the deposit. The standoff distance plays a significant role in the final part height. Our contribution is the proposed model is the creation of a physical model that describes the LWAM process where key parameters such as the standoff distance are included.

In summary, the dynamics model proposed in this chapter gives a physical meaning and good insight into the role of deposition process parameters, material properties and thermal behavior during the LWAM process. It allows simulating chosen inputs as a function of the bead geometry's desired output. This closed-form model was created using physical balance equations and the combination of existing closed-form expressions cited earlier [108, 109, 112]. The model provides easiness and computation efficiency for offline simulation when dealing with process design and developing a controller for LWAM monitoring and control tasks.

4.2 Numerical model

As a non-linear process, LWAM involves complex interaction to perform a material transfer using laser power and a wire. The process parameters interfering in the process are the laser power, the travel speed, the standoff distance, the wire feed rate, etc. A physics-based model for the LWAM process is created in this work to solve the issue. Some assumptions based on previous studies and our understanding of the LWAM process are used to develop he desired model. The model provides a physical description of the LWAM process, considering most of the process requirements. This model is also a pillar for a reliable controller design.

The first assumption is taken from Doumanidis et al. [108]. Doumanidis stated the mass conservation of the melt pool equation. The equation says that the mass change rate of the melt pool is equal to the material transfer rate minus the mass rate of solidification (material loss).

$$\frac{d}{dt}(\rho V) = \mu f_r - \rho A v \tag{4.1}$$

where ρ is the melt pool density, V is the volume of the melt pool, μ is the mass transfer efficiency, f_r is the total material transfer rate (wire feed rate), A is the cross-section area of the melt pool and v is the travel speed. The mass transfer efficiency of the deposition is the ratio of the mass deposited over layers with respect to the consumed wire. Doumanidis's idea was applied to the LWAM process using a similar assumption.

This equation was derived assuming the bead geometry profile to have a half-ellipsoidal form in the LWAM process as shown in Figure 4.2. The half of the three-dimensional ellipsoid is characterized by the melt pool width, w, the melt pool length, l, and the melt pool height, h. Therefore, the volume V can be expressed with respect to the melt pool geometry variables w, h, l as:

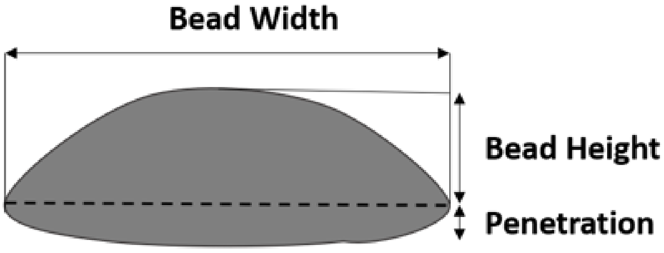

Figure 4.2: Half-ellipsoidal form of the bead geometry

$$V = \frac{\pi}{6} w h l \tag{4.2}$$

and the area A will be equal to

$$A = \frac{\pi}{4} w h \tag{4.3}$$

Further, for simplicity, the ratio between the melt-pool width and height will be fixed. Also, the melt-pool width and length are assumed to be equal [113]. In this work, some deposition trials allowed to obtain this ratio for different process parameters, as presented in 3. The equation presented by Doumanidis et al. is adapted to LWAM process. However, the model should be extended to reflect and describe the process fairly. After substituting the volume, the area, the ratio and the width-length equality assumption to Equation 4.1, the mass conservation equation of the melt-pool becomes:

$$\frac{d}{dt}\left(\frac{\pi}{6}\rho whl\right) = \mu f_r - \frac{\pi}{4}\rho rh^2 v \tag{4.4}$$

The derivative of $\frac{d}{dt}\left(\frac{\pi}{6}\rho whl\right)$ with respect to the melt-pool height variable assuming that $l = w$ and the ratio $r = w/h$ gives the following expression:

$$\frac{d}{dt}\left(\frac{\pi}{6}\rho wh(t)l\right) = \frac{d}{dt}\left(\frac{\pi}{6}\rho w^2 h(t)\right) = \frac{d}{dt}\left(\frac{\pi}{6}\rho r^2 h(t)^2 h(t)\right) = \frac{d}{dt}\left(\frac{\pi}{6}\rho r^2 h(t)^3\right) = \rho\frac{\pi}{2}r^2 h^2(t)\frac{dh(t)}{dt} \tag{4.5}$$

Then the mass balance equation of the melt pool can be rewritten as:

$$\rho\frac{\pi}{2}r^2 h^2(t)\frac{dh(t)}{dt} = \mu f_r - \rho\frac{\pi}{4}rh^2(t)v \tag{4.6}$$

Also, the melt-pool width and length are assumed to be equal has proven in many experiments. In this work, w = l for simplicity. The next step is to find the material transfer rate. The material transfer rate is the product of the mass transfer efficiency and the total material transfer rate (wire feed rate) μf_r.

In Equation 4.6, the obtained model does not explicitly show how the model uses the laser power. Also, several process parameters and material properties should be shown up in the equation to understand the physics of the deposition process. It is known that the melt-pool area and volume are mainly dependent on the laser power and the travel speed as discussed in Section 4.1. To improve and adapt the Doumanidis model to the LWAM process, Equation 4.6 needs to be extended to an equation that relates the melt-pool dimension to the process parameters and material properties. Eagar and Tsai [114] developed an equation expressing a Gaussian heat distribution of the melt-pool where the pool shape was represented as a function of the operating parameter. The equation is in the following form:

$$n = \frac{Qv}{4\pi a^2 \rho C\left[T_m - \mathrm{T}\right]} \tag{4.7}$$

Where Q is the laser power, a is the thermal diffusivity, C is the specific heat, T_m is the melting temperature and T, the initial temperature of each layer. To extend the equation to the bead geometry profile, Wang et al. [109] proposed a parametrization of the melt pool cross-sectional area at steady state to the operating process parameters n.

$$\bar{A} = \Gamma(\bar{n}) \tag{4.8}$$

where Γ is a linear function. Wang expressed the melt pool cross-sectional area at a steady state as:

$$\bar{A} = Av^2/4a^2 \tag{4.9}$$

Following this idea, this work adopts the same assumption for the cross-sectional area and assumes the existence of a linear coefficient called Γ. From the assumptions, Wang's parametrization shown in Equation 4.8 becomes:

$$\frac{Av^2}{4a^2} = \Gamma \frac{Qv}{4\pi a^2 \rho C\left[T_m - \mathrm{T}\right]} \tag{4.10}$$

From Equation 4.10, the cross-sectional area A is derived:

$$A = \Gamma \frac{Q}{\pi \rho v C\left[T_m - \mathrm{T}\right]} \tag{4.11}$$

From Equation 4.11, it is evident that the melt-pool area varies with the increase or decrease of the laser power, and it also varies with the variation of the velocity. Considering the melt pool's balance Equation 4.1 at steady-state conditions, d/dt $(\rho V) = \mu\ f_r - \rho\ A\ v = 0$, gives $\mu\ f_r = \rho\ A\ v$. This means that the material transfer rate is equal to the mass rate of solidification at a steady state. Then the material transfer rate, $\mu\ f_r$ can be approximated to the mass rate of solidification. Therefore, the following equation can be drawn:

$$\mu f_r \cong \rho A v \tag{4.12}$$

Therefore the material transfer rate from Equation 4.12 is equaled to Equation 4.11

$$\mu f_r \cong \Gamma \frac{Q}{\pi C\left[T_m - T\right]} \tag{4.13}$$

Then, the mass balance equation becomes

$$\rho\frac{\pi}{2}r^2h^2(t)\frac{dh(t)}{dt} = \Gamma\,\frac{Q}{\pi C\left[T_m - \mathrm{T}\right]} - \rho\frac{\pi}{4}rh^2(t)v \tag{4.14}$$

The obtained final equation is further extended. The extension can be possible with Pinkerton et al.'s works [112]. Pinkerton stated that the heat flowing into the melt pool is determined by considering the interaction between laser parameters and the melt pool. Pinkerton et al. expression has used the optics parameters and the power variation with respect to the z-axis to describe the system. It assumes the laser beam to have an even power distribution for the calculation of the intensity of radiation that reaches the melt pool. The equation states that the diameter of the laser beam in a horizontal plane through the deposition point, d, is given in terms of the melt pool standoff, z_{pool}, the beam diameter D, and the focal length of the objective lens f.

$$d = D\left|\frac{f - z_{\mathrm{pool}}}{f}\right| \tag{4.15}$$

Further, Pinkerton investigated the relationship between the intensity and other variables. Pinkerton developed another equation that relates the intensity of the laser source I to other process parameters and material properties around the beam area at the melt pool.

$$I = \frac{4f^2\left(1 - r_{\mathrm{p}}\right)Q}{\pi D^2\left(f^{-z}\mathrm{pool}\right)^2} \tag{4.16}$$

With Q is the laser power and r_{p} is the proportion of laser power reflected from the wire. Also, Pinkerton assumed that the heat flowing into the melt pool to be proportional to the intensity of the laser source I, the melt pool width w and the melt pool's surface absorptivity α. Therefore, the rate of heat flowing into the melt pool, $\dot{Q}$ is expressed as

$$\dot{Q} = \frac{\pi\alpha I w^2}{4} \tag{4.17}$$

The following equation is drawn for the LWAM process based on Pinkerton's equations.

It is assumed that in the LWAM process, the heat flowing into the melt pool is expressed as:

$$\dot{Q} = \frac{\alpha f^2 w^2 \left(1 - r_p\right) Q}{D^2 \left(f - z_{\text{pool}}\right)^2} \tag{4.18}$$

where α is the absorptivity of the melt pool, f is the focal length, w the width of the deposited bead, r_p is the reflected laser power from the wire; Q is the laser power, D is the beam diameter of the laser source and z_{pool} is the standoff distance.

In LWAM, the standoff distance (z_{pool}) is not stated forward and well defined as in other processes, this variable will be set up, in this work, in the following manner. The z_{pool} is defined with respect to DT, which is called the working distance. In this work, we assume that $DT = z_{\text{pool}} + n_z$, as shown in Figure 4.3, where n_z is the nozzle variable that describes by the movement of the nozzle on the Z-axis.

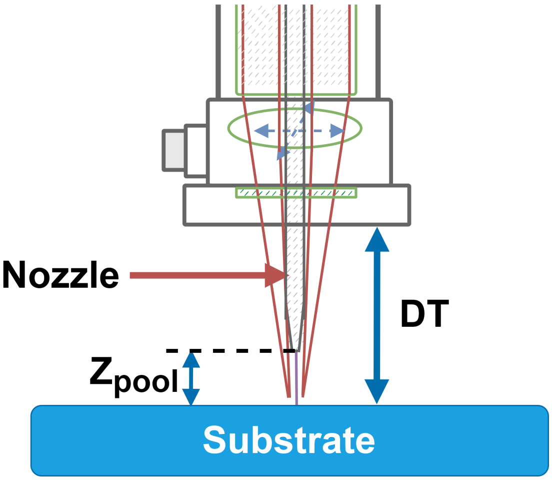

Figure 4.3: Standoff distance set-up.

In order to extend the Equation 4.19 to more process parameters and material properties, the Rosenthal equation 4.19 is used in the LWAM process. It is assumed that the heat flowing into the melt pool moves from layer to layer during the deposition process. The application of Rosenthal's equation [115] at each layer edge is assumed to be:

$$T\left(Z_i\right) = T_{i-1} + \frac{\dot{Q}}{2\pi k R_i} e^{-\frac{v\left(W_i\right)}{2a}} \tag{4.19}$$

where $T\left(Z_i\right)$ is the initial temperature at layer Z_i, T_{i-1} is the temperature of the preceeding layer with $i = 1$ to n; n is the last layer, $\dot{Q}$ is the heat flow to the melt pool, k is the thermal conductivity, R_i is the length of the part, W_i is the theoretical layer thickness, v is the travel speed and a is the thermal diffusivity. Substituting Equation 4.18 into Equation 4.19 will change the temperature distribution at each layer edge (orange points in Figure 4.4) while including more process variables (z_{pool}, f, D, v) and more material properties (α, k, a) to the LWAM process for a fair physical description of the process. The generated equation is:

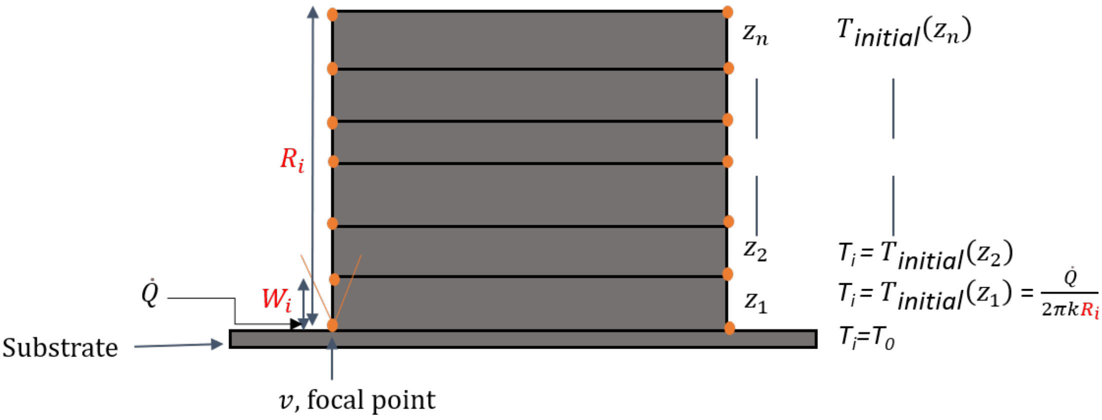

Figure 4.4: Rosenthal solution applied to the LWAM process

$$T\left(z_i\right) = T_{i-1} + \frac{\alpha f^2 w^2 \left(1 - r_p\right) Q}{2\pi k R_i \left(D^2 \left(f - z_{pool}\right)^2\right)} e^{-\frac{v(W_i)}{2a}} \tag{4.20}$$

Then, the material transfer rate from Equation 4.13 will take the following form after replacing the temperature Equation 4.20 into 4.13:

$$\mu f_r = \Gamma \frac{Q}{\pi C \left[T_m - T_{i-1} - \frac{\alpha Q f^2 w^2 (1 - r_p)}{2\pi k R_i \left(D^2 \left(f - z_{pool}(t)\right)^2\right)} e^{-\frac{v(W_i)}{2a}}\right]} \tag{4.21}$$

The mass balance equation from Doumanidis 4.1 becomes an extended dynamics multivariable equation applied to the LWAM process. The extended equation calculates the melt pool height for the LWAM process while taking into consideration several process variables and material properties involved in the complex process.

$$\rho \frac{\pi}{2} r^2 h^2(t) \frac{dh(t)}{dt} + \rho \frac{\pi}{4} r h^2(t) v = \Gamma \frac{Q}{\pi C \left(T_m - T_{i-1} - \frac{\alpha Q f^2 w^2 (1 - r_p)}{2\pi k R_i \left(D^2 \left(f - z_{pool}\right)^2\right)} e^{-\frac{v(W_i)}{2a}}\right)} \tag{4.22}$$

This equation includes several variables that can be used for simulation purposes to understand their influence on bead geometry. Further, this equation can be used in a control system to regulate one or more deposition process parameters.

4.3 Numerical Validation

For the three cases, experimental tests were performed on the laser platform at Institut de Soudure. A robotized laser wire-feed system ran tests. An ABB 6-axis poly-articulated robot is used to provide the kinematics of the process. A fiber laser source called IPG Photonics with a power of 10 kW was used. A CoaxPrinter laser head is used to deliver the laser beam and the wire. Figure 4.5 shows the LWAM system setup.

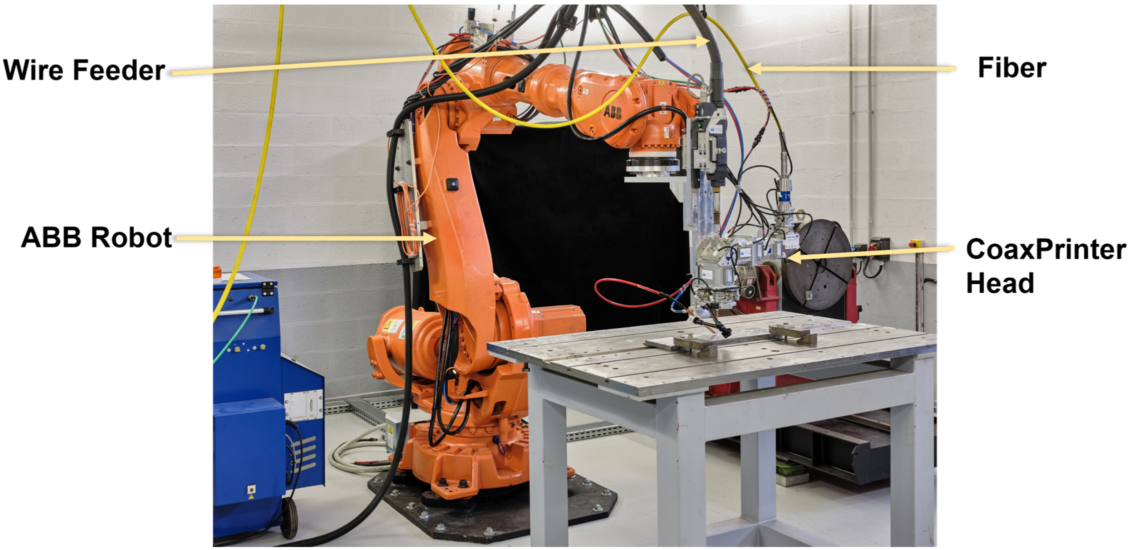

Figure 4.5: Experimental Setup of LWAM platform at Institut de Soudure.

For validating the physical-based model, derived in Section 4.2 and given by Equation (4.22), two metallic hollow cylinders were deposited. It is worth mentioning that, the cylinder shape was chosen as a deposition object, based on the fact that it is more convenient for a continuous and clear height profile acquisition due to the configuration of the precited head and the placement of the profilometer, as shown in Figure 4.6.

The deposition process parameters for both cylinders are summarized in Table 4.1. Furthermore, the process variables and material properties of Inconel 718 with their definitions are shown in Table 4.2 and 4.3 respectively.

Figure 4.6: Profilometer set-up for data acquisition.

Table 4.1: Process parameters for the two deposited cylinders.

	Power (W)	Travel speed (m/min)	Wire feed rate (m/min)	Standoff distance (mm)	Number of layers	Layer thickness (mm)
Cylinder 1	2700	2.0	2.4	1.5	9	0.7
Cylinder 2	2100	0.6	2.1	1.5	8	1.2

Table 4.2: Process variables and material properties of Inconel 718.

Symbols	**Parameters**	**Parameters Value**	**Sources**
Γ	Gain	Variable	Experiments
Q	Power (W)	Variable	Experiments
C	Melt specific heat $(J/(kg.K))$	760 - 800	[116]
T_m	Melting temperature (K)	1570	[116]
T_{i-1}	Temperature of the preceeding layer (K)	Variable	Experiments
α	Absorptivity of the melt pool	0.5	[117]
f	Focal length of the objective lens (m)	160e-3	Experiments
w	Melt pool width (m)	Variable	Experiments
r_p	Proportion of laser power reflected	0.7	[118]
k	Thermal conductivity $(W/m.K)$	33	[116]
R_i	Height of the product (m)	Variable	Experiments
D	Laser beam diameter of the laser (m)	3.95e-3	Experiments
z_{pool}	Standoff distance (m)	Variable	Experiments
v	Travel speed of the robot (m/s)	Variable	Experiments
W_i	Layer thickness (m)	Variable	Experiments
a	Thermal diffusivity (m^2/s)	$a = k/(C/\rho)$	[119]
ρ	Melt pool density (kg/m^3)	Variable	[117]
r	Width over height ratio (m)	Variable	Experiments
h	Melt pool height (m)	Output	Calculated using the model

Table 4.3: Summary of the definition of the parameters.

Parameter	**Definition**
Γ	Constant gain
Q	Input laser power
C	Quantity of heat needed to increases the temperature 1 K per unit mass (kg)
T_m	Melting temperature of the material
T_{i-1}	Temperature of the layer where a new deposition will be done
α	The degree to which the material absorbs the laser power
f	The distance from the last lens to the point at which the laser beam is focussed
w	The measured width of a deposited bead
r_p	Reflected laser power from the material wire
k	The rate at which the heat is transferred by conduction through a unit cross-section area of material
R_i	Total height of the part to be produced
D	The diameter of the focuses laser beam
z_{pool}	Distance from the substrate to the nozzle tip
v	Deposition speed
W_i	Theoretical layer thickness
a	The ability of the material to conduct thermal energy thermal energy
ρ	Density of the material - the mass of a unit volume of the material
r	The ratio of the width to the height
h	Height of the deposited beads

Cylinder 1 has a diameter of $180mm$ and cylinder 2 has a diameter of $250mm$. The multi-step input trajectory of the temperature is 9 intervals for the first cylinder and 8 intervals for the second cylinder. The mean temperature is averaged for each layer and it has been considered as an input profile for the model validation, as shown in Figure 4.7.

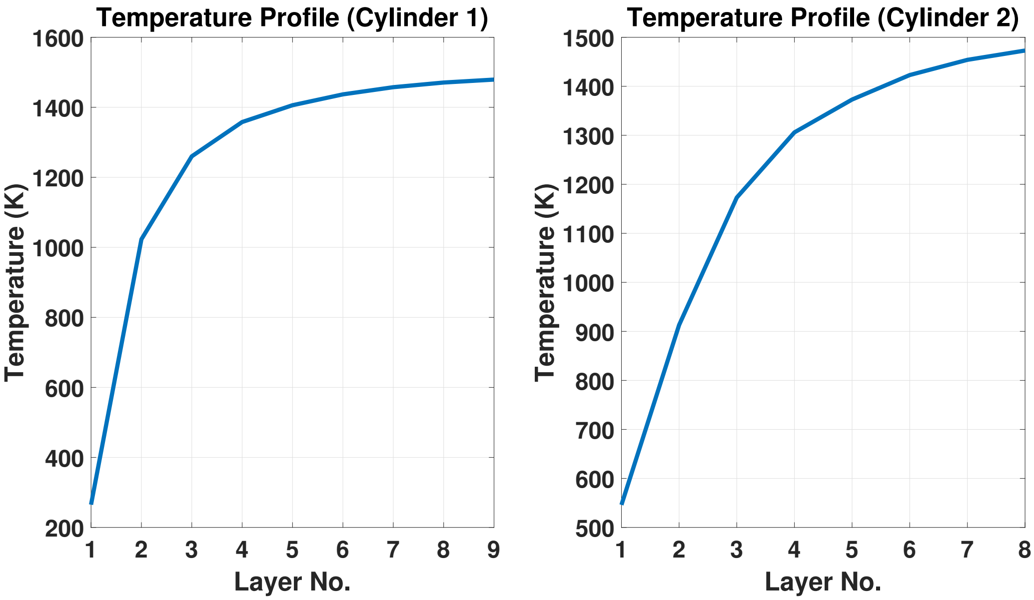

Figure 4.7: Temperature profile of cylinder 1 and cylinder 2.

The observation in Figure 4.7 can be explained by the high cooling and thermal dissipation of the first layers on the substrate. The layer temperature increases significantly in the early layers and increases slowly at the final layers, where it starts to reach a steady-state point. Therefore, as the layers increase, the thermal dissipation reduces and tends to reach the steady-state (layer 9 for cylinder 1 and layer 8 for cylinder 2). It is observed that when the temperature drops significantly at the earlier layers and less at the last layers, desired layer heights can be obtained. This observation matches our assumption and shows that the accumulation of height errors could be decreased by proper controlling the temperature input while printing the final product.

For each layer, bead geometry information of the deposited layer is collected using a scanControl 2950-100/BL laser profilometer. The measurement range of the device is up to 265 mm on the z-axis, and the measuring rate is up to 2,560,000 points/sec. The measurement range on the x-axis is up to 143.5 mm and the accuracy of the measurement is 12 m.

For this study, the profilometer laser is projected near the melt pool and close to the hot deposited layer to measure the bead geometry (see Figure 4.6). The target material, which is the hot Inconel 718, is a red-hot glowing metal. It emits a wavelength of 1000 nm and emits a high proportion of light at the wavelengths in which the laser operates. Blue laser light was used at a shorter wavelength of 405 nm, far from the visible spectrum red part. This means that the blue laser light is unaffected by the emitted light and can provide stable signals. The data acquisition of the two cylinders with model validation outputs are shown in Figure 4.8 and Figure 4.9.

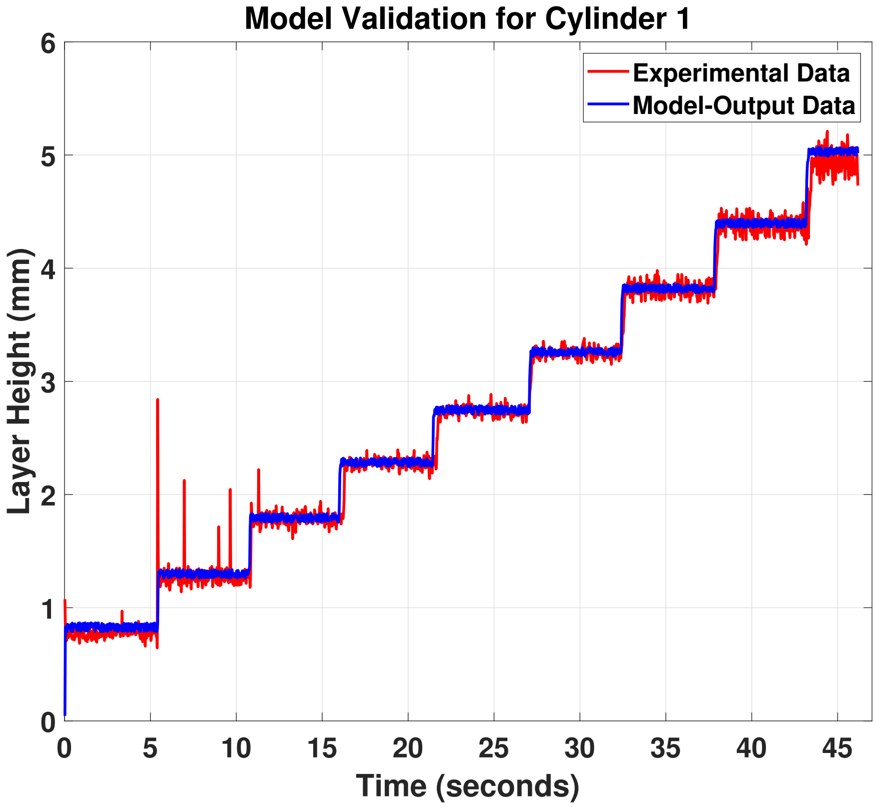

Figure 4.8: Model validation for cylinder 1

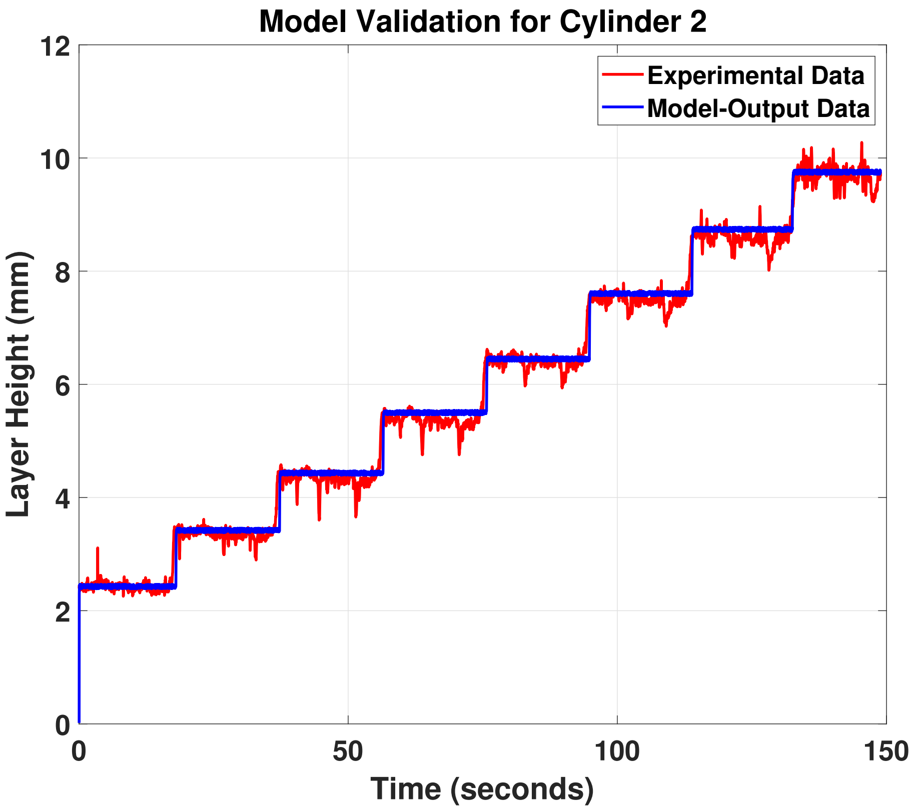

Figure 4.9: Model validation for cylinder 2

The results in Figure 4.8 and Figure 4.9 show that the proposed model predictions (blue curve) for the melt-pool height follow the experimental measurements (red curve) very well, and both the predictions and measurements show a clear pattern of step changes, correlating to the step changes of the printed layer height. Based on this obtained model, an MPC feedback controller can be designed to track the melt-pool height trajectory using the temperature input to improve the final printed product. However, some fluctuations can be seen in the experimental data. This can be explained by the vibrations caused by the robot's movement while collecting the data using the laser profilometer. Furthermore, the surface roughness of the printed cylinder provides additional noise to the bead height measurements. Nonetheless, this noise and fluctuation of the collected data are common in the Metal Additive Manufacturing processes (see e.g., [109]) and it doesn't affect the influence of the general dynamic behaviour of the system.

4.4 Summary

This work developed a physics-based model of the bead geometry for the Laser Wire Additive Manufacturing process (LWAM). The developed model aimed to include known process parameters and material properties to describe the LWAM process properly. The validation performed for two cylinders using the temperature profiles measured approximately layer by layer shows that the developed model matches the experiment data, thus predicting the layer height well. The main contribution is the adding of critical process parameters influencing the deposition stability in the LWAM. The following conclusions are drawn:

- The proposed model describes and simulates the behavior of the bead geometry in the laser wire additive manufacturing process.
- The temperature is an important input parameter and significantly influences the layer by layer deposition.

In the next chapter, an MPC controller will be designed to track the reference height and regulate the temperature input while keeping it in its region of operation.

Chapter 5

Bead Height Control

5.1 Introduction

The AM process usually needs reliable sensing, modeling, and control approaches to work well. Several methods, such as computational, empirical, and physical models, can be used to modelized and control the process. Finite Element Analysis is mainly employed for the computational method. Several works can be reported [120]. In [97], Magerramova et al. investigated body parts using computational and experimental methods. The finite element method (FEM) was used in the Laser-Based Manufacturing Process to simulate gearbox housings and numerically optimize the product weight. The results show that the mass of body parts is reduced by up to 15% with the same strength properties. In [98] Liu et al. used a 3D microscale FEM with a powder arrangement system to simulate multi-layer powder stacking for Selective Laser Sintering (SLS). The model aimed mainly to investigate the thermal evolution of selective laser sintering using metal powders.

In [103], a process map of single beads of Ti-6Al-4V was created using finite element analysis. The process is developed for the microstructure solidification in electron beam wire feed AM processes. In [104], Panagiotis et al. investigated finite element methods for modeling heat transfer analyses of metal additive manufacturing. While in [105], Dong et al. used a finite element model to simulate the thermal and sintering phenomena occurring during the selective laser sintering deposition process. The model included the heat transfer coupling equation and the powder sintering equation. The presented computational method focused mainly on the microstructures, heat transfer, and material properties. However, the computational method has its limitation as it is difficult to employ them for a control system design because of the complex partial differential equations. Empirical models could be a good solution to overcome the computational method issues. Many works can be related. In [121], a PI-closed loop controller was implemented for keeping a constant melt pool width during the deposition based on an infrared imaging system. This implementation showed that the control model gave satisfactory results in adjusting the laser power to keep a stable melt pool width compared with depositions where constant laser power was used. In [122], Song et al. presented a predictive control strategy for the melt pool temperature stabilization for the laser cladding process. A dual-color pyrometer was employed to obtain the temperature measurement and a state-space dynamic model was used to represent the process. The results showed that the closed-loop model could track and stabilize the melt pool temperature. In [123], Devesse et al. used a hyperspectral camera to obtain measurements of the temperature from the melt pool surface. A linear state feedback and a proportional-integral controller based on a linearized physical model of the melt pool dynamics are used to keep the melt pool width constant. Experimental results showed that the control system achieve a good regulation of the melt pool size with acceptable errors.

In [124], Farshidianfar et al. developed an infrared system to monitor surface temperatures of deposition microstructure during Laser Additive Manufacturing (LAM). A PID feedback controller stabilizes the cooling rate by adjusting the travel speed. The experimental results show that the controller can achieve acceptable microstructure in real-time. In [125], a structured light scanner is used to obtain the part height. A closed-loop controller is implemented to adjust the deposition height to ensure a good geometrical accuracy of the final part. The results show that the model can give satisfactory results both on power and wire-based laser metal deposition (LMD). In [126], Heralic et al. used a 3D scanning system to obtain the surface for each deposited layer. An iterative learning control system compensates for the depositions by varying the wire feed rate across layers. The experimental results showed that the developed model works for the automatic deposition of structures. In [127], Liu et al. used a near-infrared monochrome (NIRM) camera to get the melt pool size and a first-order transfer function created for an automatic control system. The laser power was used as the input variable in the system and a model predictive controller (MPC) was created to control the melt pool size. The experimental results showed that the control system had improved the final part quality. In [128], a single-neuron self-adjusting controller is created for the wire and arc additive manufacturing (WAAM) process. The controller takes the travel speed as the input to correct the layer width. The experimental results show that the controller contributes to the stability of the layer width. In [129], the clad height is controlled using the scanning speed as the control input. A charge-coupled charge-coupled device (CCD) camera gets the training data profiles and Adaptive Neuro-Fuzzy Inference Systems (ANFIS) are developed to control the system. The experimental results showed satisfactory outcomes in the laser cladding process. In [130], Zeinali et al. presented a real-time acquisition and control of the clad height. The substrate velocity is taken as the input of the system. A CCD is used to obtain the clad heigh and an adaptive sliding mode control with an uncertainty estimator is implemented. The experimental results showed an improvement in the final deposition.

In [131], Moralejo et al. controlled the melt pool geometry of laser cladding by implementing a feedforward and a Proportional integral (PI) controller. The input of the system is the laser power and the output is the melt pool width. A CMOS camera is used to obtain the melt pool images. The results showed that the controller improved the system response with minor delay. In [132], photodiodes were used to obtain the heat radiation signal in Laser Metal Deposition (LMD) and an adaptive Proportional Integral-Derivative (PID) control was implemented to adjust the laser power and control the weld pool size. The experimental results showed that the system successfully controlled the weld pool size with an acceptable range. In [133], Fathi et al. presented a Sliding Mode controller (SMC) based on a parametric Hammerstein model to control the deposited layer geometry. The scanning speed is used as the control input. The experimental results showed that the controller could reduce the stair-step effect in the created parts. As reported in the state of the art, it can be noticed that there is a lack of a model-based controller in the literature. The drawbacks of the numerical and empirical methods are the need for several experimental tests to obtain response experiments and develop a reliable control model.

In this chapter, a controller is designed based on the developed physics model created in chapter 4. Since the created model has many variables with constraints, and some of the variables can be used simultaneously as input variables, a Model Predictive Controller (MPC) is proposed to solve the problem and obtain a good process efficiency. MPC is suitable for most multivariable continuous control applications. The goal is to achieve good performance for a wide range of operating conditions in the LWAM process. The physics-based model developed is used as the plant of the controller and incorporates knowledge of how the layer height change with the operating process parameters and material properties.

The linearization process has been applied in many domains where the non-linear model is difficult to solve [134–138]. In section 5.2, the developed model is first linearized using Taylor's series expansion and the Jacobian linearization process. In the linearization process, the gradient of the nonlinear equation for all process parameters and material properties variables is evaluated in order to create a linear representation at the evaluation point.

5.2 Model Linearization

In the developed model, the main process parameters are the temperature, the laser power, the travel speed, the layer thickness and the standoff distance. Therefore, these parameters are selected as inputs. In this thesis, only one input, the temperature, is considered to investigate the system's behavior. The state vector is $h(t)$ and the inputs are $T_{i-1}(t)$, $Q(t)$, $v(t)$, W_i, and z_{pool}. As the developed model is non-linear, the state-space equation derived is non-linear and represented as:

$$\frac{dh(t)}{dt} = \dot{h} = \frac{2\Gamma Q}{\pi^2 C h^2 r^2 \rho \left(-\frac{Q f^2 w^2 \alpha (1-r_p) e^{-\frac{W_i v}{2a}}}{2\pi R_i D^2 k \left(f - z_{\text{pool}} \right)^2} + T_m - T_{i-1} \right)} - \frac{v}{2r} \tag{5.1}$$

The equation needs to be linearized to create a linear state-space form. The non-linear equation can be represented as $\frac{dh(t)}{dt} = f(T_{i-1},\, Q,\, v,\, W_i, z_{pool})$ The equation will be linearized by a Taylor series expansion as the following.

$$\frac{dh}{dt} = f(h,u) \approx f(\bar{h},\bar{u}) + \left.\frac{\partial f}{\partial h}\right|_{\bar{h},\bar{u}} (h-\bar{h}) + \left.\frac{\partial f}{\partial u}\right|_{\bar{h},\bar{u}} (u-\bar{u}) \tag{5.2}$$

$\bar{h}$ and $\bar{u}$ are the steady-state values of the state and the inputs; therefore, $f(\bar{h},\bar{u}) = 0$. The linearized expression is further simplified using deviation variables are defined as $h' = h - \bar{h}$ and $u' = u - \bar{u}$. The deviation variables are the change in the steady-state conditions. The derivatives of the deviation variable give: $\frac{dh'}{dt} = \frac{dh}{dt} - \frac{d\bar{h}}{dt}$ and $\frac{du'}{dt} = \frac{du}{dt} - \frac{d\bar{u}}{dt}$ The partial derivatives at steady-state are zero $\frac{d\bar{h}}{dt} = 0$, $\frac{d\bar{u}}{dt} = 0$, therefore $\frac{dh'}{dt} = Ah' + Bu'$ where A and B are the partial derivatives of $f(h,u)$ at steady-state conditions. The state-space form of a Linear Time Invariant (LTI) system is given as:

$$\begin{aligned} \dot{x} &= Ax + Bu \\ y &= Cx + Du \end{aligned} \tag{5.3}$$

where $x \in R^n$ is the state, $\dot{x} \in \mathbb{R}^n$ is the state derivative, $y \in \mathbb{R}^p$ is the output, $u \in \mathbb{R}^m$ is the input. A is the state matrix, B is the input matrix and C the output matrix. D is the matrix showing the influence of the inputs on the output. The dimensions of the matrix are $A \in \mathbb{R}^{n\times n}$ $B \in \mathbb{R}^{n\times m}$ $C \in \mathbb{R}^{p\times n}$ $D \in \mathbb{R}^{p\times m}$ with m the inputs, n the states and p the outputs.

The final linearized equation in linear state space form with five inputs, one state, and one output is:

$$\dot{x} = \left[\left.\frac{\partial f}{\partial x}\right|_{\bar{x},\bar{u}}\right] x + \left[\left.\frac{\partial f}{\partial T_{i-1}}\right|_{\bar{h},\bar{u}} + \left.\frac{\partial f}{\partial \bar{Q}}\right|_{\bar{h},\bar{u}} + \left.\frac{\partial f}{\partial v}\right|_{\bar{h},\bar{u}} + \left.\frac{\partial f}{\partial W_i}\right|_{\bar{h},\bar{u}} + \left.\frac{\partial f}{\partial z_{pool}}\right|_{\bar{h},\bar{u}}\right] u \tag{5.4}$$

$$y = x \tag{5.5}$$

where

$$A = \left[\left.\frac{\partial f}{\partial \mathrm{x}}\right|_{\bar{x},\bar{u}}\right] \tag{5.6}$$

$$B = \left[\left.\frac{\partial f}{\partial T_{i-1}}\right|_{\bar{h},\bar{u}} + \left.\frac{\partial f}{\partial \bar{Q}}\right|_{\bar{h},\bar{u}} + \left.\frac{\partial f}{\partial v}\right|_{\bar{h},\bar{u}} + \left.\frac{\partial f}{\partial W_i}\right|_{\bar{h},\bar{u}} + \left.\frac{\partial f}{\partial z_{pool}}\right|_{\bar{h},\bar{u}} \right] \tag{5.7}$$

$$C = 1 \text{ and } D = 0 \tag{5.8}$$

The computed matrices are give as follows,

$$A = -\frac{4}{\pi^2 C h^3 r^2 \rho \left(-T_i + T_m - \mid \frac{Q f^2 w^2 \alpha (1-r_p) e^{-\frac{W_{ij}}{2a}}}{2\pi R_i D^2 \left(f - z_{pool}\right)^2} \right)} \tag{5.9}$$

$$B_{11} = \frac{2\Gamma Q}{\pi^2 C h^2 r^2 \rho \left(-T_i + T_m - \frac{Q f^2 w^2 a (1-r_p) e}{2\pi R_i D^2 \left(f - z_{pool}\right)^2} \right)^{-\frac{W_{ij} v}{2a}} \Bigg)^2} \tag{5.10}$$

$$B_{12} = \frac{2\Gamma}{\pi^2 C h^2 r^2 \rho \left(-T_i + T_m - \frac{Q f^2 w^2 \alpha (1-r_p) e}{2\pi R_i D^2 k \left(f - z_{pool}\right)^2} \right)} \tag{5.11}$$

$$+ \frac{\Gamma Q f^2 w^2 \alpha \left(1 - r_p\right) e^{-\frac{W_{ij} v}{2a}}}{\pi^3 C R_i h^2 r^2 \rho D^2 k \left(f - z_{pool}\right)^2 \left(-T_i + T_m - \frac{Q f^2 w^2 \alpha (1-r_p) e}{2\pi R_i D^2 \mathrm{k} \left(f - z_{pool}\right)^2} \right)^{-\frac{W_{ij} v}{2a}} \Bigg)^2} \tag{5.12}$$

$$B_{13} = -\frac{1}{2r} - \frac{W_{ij} \Gamma Q^2 f^2 w^2 \alpha \left(1 - r_p\right) e^{-\frac{W_{ij} v}{2a}}}{2\pi^3 C R_i h^2 r^2 \rho D^2 a k \left(f - z_{pool}\right)^2 \left(-T_i + T_m - \frac{Q f^2 w^2 a (1-r_p) e}{2\pi R_i D^2 k \left(f - z_{pool}\right)^2} \right)^{-\frac{W_{ij} v}{2a}} \Bigg)^2} \tag{5.13}$$

$$B_{14} = -\frac{g \Gamma Q^2 v f^2 w^2 \alpha \left(1 - r_p\right) e^{-\frac{W_{ij} v}{2a}}}{2\pi^3 C R_i h^2 r^2 \rho D^2 a k \left(f - z_{pool}\right)^2 \left(-T_i + T_m - \frac{Q f^2 w^2 \alpha (1-r_p) e}{2\pi R_i D^2 k \left(f - z_{pool}\right)^2} \right)^{-\frac{W_{ij} v}{2a}} \Bigg)^2} \tag{5.14}$$

$$B_{15} = \frac{2\Gamma Q^2 f^2 w^2 \alpha \left(1 - r_p\right) e^{-\frac{W_{ij} v}{2a}}}{\pi^3 C R_i h^2 r^2 \rho D^2 k \left(f - z_{\text{pool}}\ \right)^3 \left(-T_i + T_m - \frac{Q f^2 w^2 \alpha (1-r_p) e^{-\frac{W_{ij} v}{2a}}}{2\pi R_i D^2 k \left(f - z_{\text{pool}}\ \right)^2} \right)^2} \tag{5.15}$$

5.3 Controller Design

The Model predictive controller (MPC) is a model-based control strategy. The MPC calculates the optimal input value by predicting the future state and the outputs over a prediction horizon with constraints based on the process's model and the current state value. This chapter aims to use MPC to predict and compensate the layer height eventual error. The dynamics equation developed provided 5 inputs that can be used singularly or combined simultaneously. The developed model is first linearized using Taylor's series expansion and the linear state-space model is used as the plant of the MPC controller.

The MPC parameters are the sample time, the prediction horizon, the control horizon, the constraints and the weights.

- **The sample time (T_s)** determines how often the MPC controller takes control actions. A rule of thumb is tofirst measure the rise time which is the time it takes to go from 10% to 90% of its final value, when given a step input. It is best to have the sample time be about 5-10% of the rise time, so that there is ample time to make corrections during the rise time.
- **The prediction horizon (P_h)** defines how far the controller predicts into the future. The prediction horizon needs to be long enough to cover significant future events. From a control-theoretic perspective, recall that a system exhibits both a steady state and transient response when subjected to a unit step input. The rule of thumb is that the prediction horizon should include about 20-30 sample times during the transient system response.
- **The control horizon (C_h)** is the time duration for which optimal control actions are computed. As a rule of thumb, the control horizon stays around 10%-20% of the prediction horizon.
- **The constraints** are specified to bound the prediction horizon. The inputs and output constraints are set to around $1/10th$ of the nominal constraint values.
- **The input and output tuning matrices** help balance the controller's performance and obtain a smooth response.

The control layer of the MPC problem is formulated as a quadratic optimization problem that is solved at each time k to determine the control actions considering that the values of state and inputs are known. The following cost function is used to represent the control problem:

$$\begin{aligned} &\min_u \quad \mathrm{J}(x(k), u(.)) = \textstyle\sum_{i=1}^{H_p} \left\{ \frac{w_i^y}{s^y} [r(k+i|k) - y(k+i|k)] \right\}^2 \\ &\text{s.t.} \\ &\quad u_{lb} \leq u(k+j|k) \leq u_{ub} \\ &\quad y_{lb} \leq y(k+i|k) \leq y_{ub} \\ &\quad \forall\ i \in \{1, ..., H_p\}\ and\ j \in \{0, ..., C_h\}. \end{aligned} \tag{5.16}$$

where, k is the current control interval, H_p is the prediction horizon, C_h is the control horizon, where ϵ_k is a non-negative slack variable , which quantifies the worst-case constraint violation. $y(k+i|k)$, $r(k+i|k)$ are the predicted value of the plant output and the reference value at ith prediction horizon step, respectively. s^y is a scale factor of the plant output, w_i^y is the tuning weight for the plant output at ith prediction horizon. u_{lb},u_{ub} and y_{lb}, y_{ub} are the low bound and upper bound of the input and output respectively.

Figure 5.1, shows the schematic diagram of the proposed MPC controller design for the LWAM system.

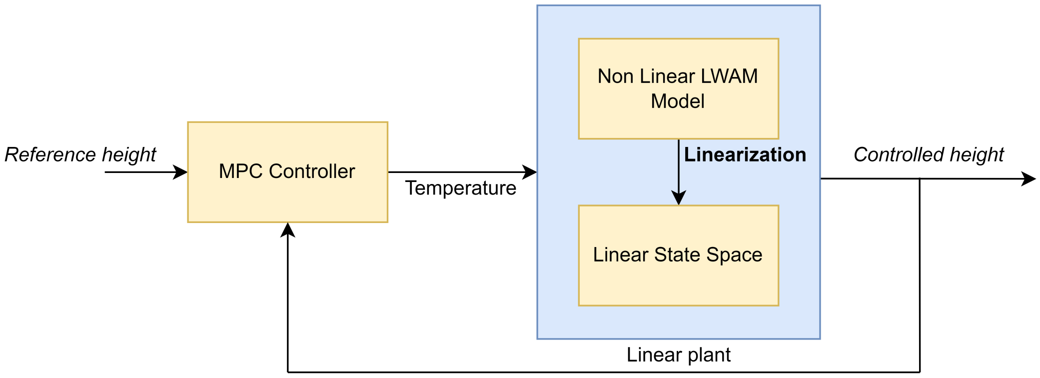

Figure 5.1: Schematic diagram for the layer height control.

Remark: For simplicity, Only the temperature input was used as the manipulated variable for the MPC controller design. More specifically, The height controller applied a generalized MPC algorithm that takes the feedback signals into the control action to improve the system performance by controlling the temperature input. This control system configuration is able to stabilize layer growth by avoiding over-building and compensating for under-building through control of the process heat input in order to have a fixed layer height [139].

For this study, the sample time T_s has been chosen to be 10% of the rise time. The prediction horizon H_p has been defined to include 20 sample times during the transient system response. The control horizon C_h was considered to stay around 10%-20% of the prediction horizon. The constraints are set to around $1/10th$ of the nominal constraint values (fore more details see e.g., [140]).

5.4 Simulation Results

The MPC controller is tested using the process parameters and material properties of Inconel® 718 [141] that are given in Table 5.1. The linearized model discussed in Section 5.2, for the provided parameters values, is given by the following state-space matrices, $A = [-0.2262]$; A is the system matrix. $B = [8.77e-08, 0.0001338, 1.815e-07, -0.01047, -0.1466]$; B is the input matrix where rows 1 to 5 represent the power input, the standoff input, the temperature input, the wire-feed rate and the travel speed respectively. For this work, only the temperature is selected and simulated as the input of the MPC controller. Finally, the output matrix $C = 1000$ and the feed-forward matrix $D = 0$.

Table 5.1: Parameters values used for MPC controller testing.

Parameter	Value	Parameter	Value	Parameter	Value
Γ	0.15	D	1.5e-3 (m)	W_i	0.7 (m)
C	800 (J/(kg K)	T_m	1570 (K)	T_0	273 (K)
f	160e-3 (m)	w	2.8e-3 (m)	r_p	0.7
r	2.33e-3 (m)	k	33 (W/m.K)	ρ	8145 (kg/m^3)
R_i	12e-3 (m)	a	5.0e-06 (m^2/s)	α	0.5 (m)

The simulation is performed in the MPC Designer toolbox in the Matlab® software. The input temperature is constrained to 273 Kelvin as the minimum and 1450 Kelvin as the maximum. It is worth mentioning that; the temperature of the deposited bead was measured layer by layer using a thermal camera during the experimental deposition. It was observed that the temperature signals of the deposited beads displayed a measured temperature of 1400 to 1450 Kelvin, and hence, the maximum input temperature in this work was chosen to be 1450

Kelvin. The height output constraints are $0.75mm$ for the minimum and $0.9mm$ for the maximum. The increments rate is 100 Kelvin. The chosen sampling time is $T_s = 0.1s$, corresponding to around every 3 bead profiles. The prediction horizon is $H_p = 15$ and the selected control horizon is $C_p = 3$. The tuning weight matrices of the input are selected to be 0.2 in order to balance the controller response and the temperature input movement. The input weight matrix Q_i is not specified to avoid steady-state error in the output. The output weight matrix is $Q_o = 5$, so the height is kept near the reference height input. The MPC parameters are summarized in Table 5.2.

Table 5.2: MPC parameters for layer height control.

MPC parameter	min value	value	max value
Sampling time (T_s in s)	-	0.1	-
Prediction horizon (H_p)	-	15	-
Control horizon (C_h)	-	3	-
Input constraint (K)	273	-	1450
Output constraint (mm)	0.75	-	0.9
Input weight	-	0	-
Output weight (mm)	-	5	-

The simulation result in Figure 5.2, shows that the MPC controller can track the layer height reference with little overshoot and acceptable responding time. The input variable, which is the temperature, increases at the beginning to reach a maximum of 1450 Kelvin and then decrease to its steady-state value of 1270 kelvin, as shown in Figure 5.3.

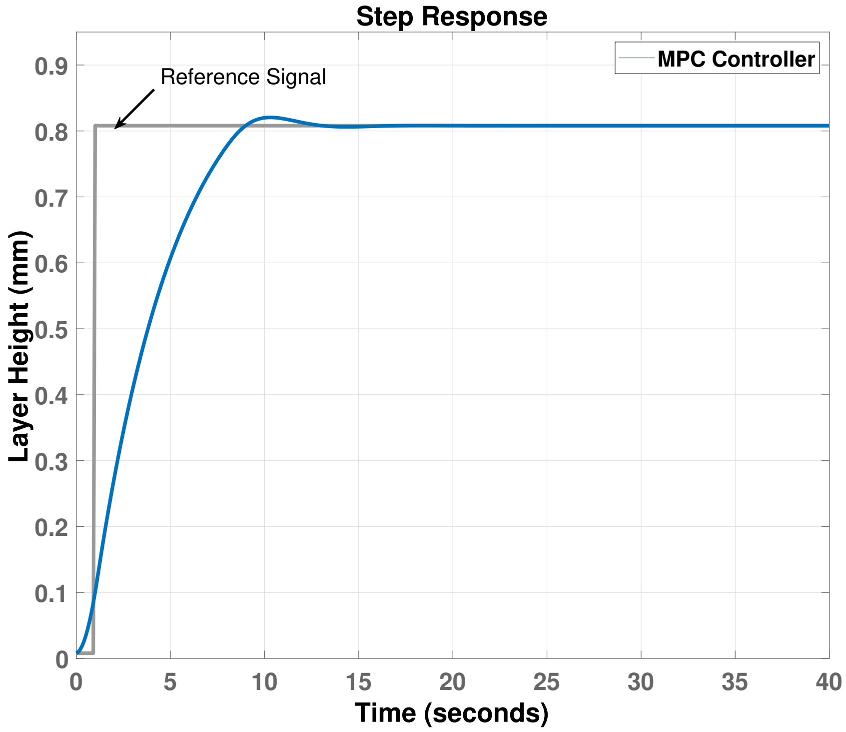

Figure 5.2: Step response of the closed-loop feedback system.

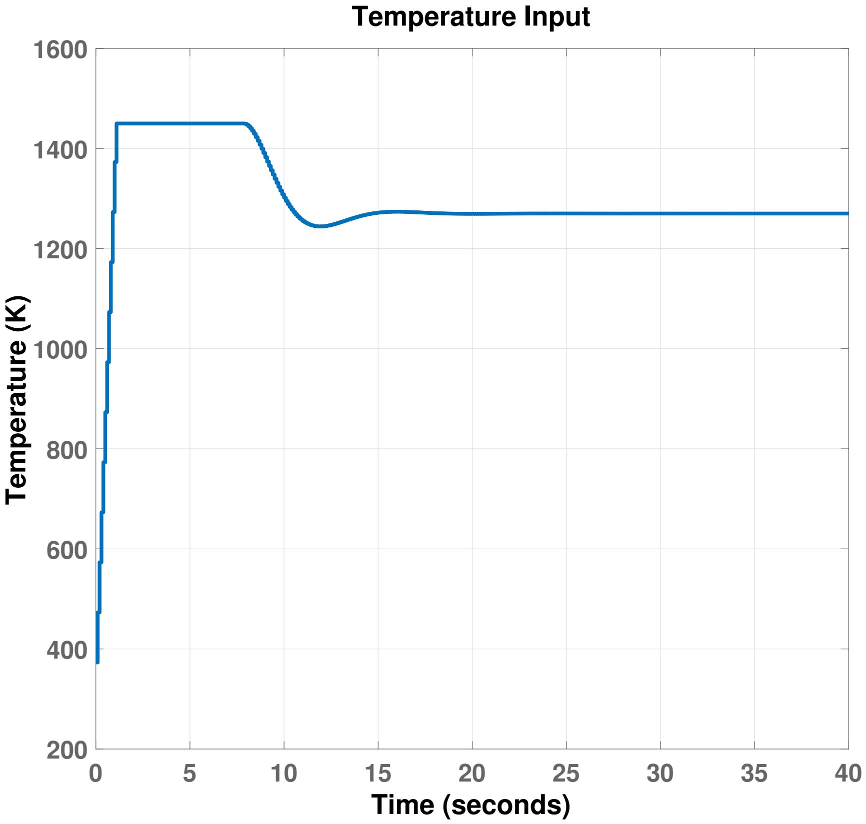

Figure 5.3: Controlled input temperature.

5.5 Summary

This chapter presented the linear state-space representation of the multivariable model developed and an MPC controller simulation. The MPC is designed to keep the bead height trajectory constant with the regulation of the input temperature in its working operation range. The MPC controller is suitable for MIMO systems where variables influence each other and have constraints. The developed multivariable model offers the flexibility to control other process parameters simultaneously within their region of operation. A cylinder was simulated using the MPC approach. The result shows that the developed offline controller can track and improve the height response when the proper MPC model parameters are selected. The following conclusions are drawn:

- The MPC controller can track the reference height and regulate the temperature input while keeping the parameters in their region of operation.
- The system response shows an acceptable transient response with an overshoot within a good tolerance 5%.

Chapter 6

Conclusion and Future Works

6.1 Conclusion

This research aimed to create a complete description of the laser wire additive manufacturing from the modeling to the control of the deposition process. An industrial robot where a laser head is attached is used to achieve this task. The results of this work are the beginning of developing a reliable and robust robotized direct energy deposition of LWAM process which is in high demand in the manufacturing process sector, mainly in the aerospace industry.

In chapter 2, a novel Parametric Modeling approach was developed for the new process. A parametric method is used to create and simulate 3D products using LWAM technology without the need for using G-code. The proposed approach creates deposition patterns and robot targets considering the deposition parameters and process requirements. Different products, such as a wall, a hollow cylinder and a complex model, were produced to verify the approach. The results show that the developed Parametric Modeling approach is feasible, adaptive, and can print precise 3D metallic objects using the LWAM process. In chapter 3, a layer geometry (width and height) prediction model is created to improve deposition accuracy. Data samples were collected to study the influence of different deposition parameters on the bead geometry. First, a machine learning regression algorithm was used to predict the bead geometry evolution of the collected experimental data. Then, a neural network-based approach was used to study the influence of different deposition parameters: laser power, wire-feed rate, and travel speed on bead geometry. The results showed that the regression algorithms could predict the bead geometry in the LWAM. Also, it is found that there exists a power decay in correlating process parameters to bead geometry. The experimental results also showed that the width-to-height ratio increases over the layer progression due to the heat conducted from the laser-matter interaction.

On the other hand, the obtained results show that control of the horizontal and vertical robot movement can be achieved more precisely by predicting in advance the bead geometry. In chapter 4, a physical non-linear model for the LWAM process was developed. The model includes the material properties of the material and the process parameters of the equipment to simulate the behavior of the bead geometry. Experimental data were collected and used to validate the model. The results show that the model works and can display the real behavior of the bead geometry during the LWAM process. In chapter 5, the developed model was first linearized using Taylor's series and Jacobian techniques in order to be used in an offline controller. Afterward, an MPC controller was created to simulate a linear state space obtained from the linearization. The simulation results show that the MPC could track the reference height and regulate the temperature input and the height response without exceeding the fixed constraints.

6.2 Future Works

For future works, In chapter 2, the parametric approach is created for a deposition process where the laser head stays orthogonally to the deposition plan. Therefore, future works can be axed in a more advanced method where robot targets for complex products can be created using the full capability of the robot. Also, a post-processing program can be created to detect optimal deposition sequences and add them automatically. In chapter 3, the developed prediction model was created for Inconel 718, therefore, to predict the geometry behavior with another material, experimental must be performed again. Therefore, it is proposed to extend the prediction function for a variety of other materials. In chapter 4, the input temperature was reasonably approximated; however, accurate temperature measurement can be obtained with a reliable device. The temperature highly affects the bead geometry behavior and is also influenced by other process parameters such as power and travel speed. That is why in chapter 5, it is suggested to develop a MISO or MIMO MPC controller to control the complete deposition process. Also, a gain-scheduling can be considered to reflect fairly the LWAM as some material properties of Inconel 718 change with the temperature. As a general remark, the LWAM process is a complex non-linear process; therefore, many data acquisition devices or estimation algorithms will bring this innovative technique to manufacturing industries in the near future.

Appendix

3D printing: A method used to build a three-dimensional product layer by layer.

Additive Manufacturing (AM): A method to create 3D parts from digital information using 3D printing techniques.

Direct Energy Deposition (DED): DED uses a thermal energy to deposit materials layer by layer.

Laser Wire Additive Manufacturing (LWAM): This method uses a laser source and a wire feedstock to create a melt pool and deposit the metal layer by layer.

Additive manufacturing simulations: The product creation process when it is simulated in software before creating the end-to-end product.

Tool path - path pattern: The movement of the robotic head to print the 3D object.

3D product optimization: This technique aims to improve the additive manufacturing simulation. It may include mathematical formulation where design parameters are identified and tuned to create the best product.

Heat source: The energy source used to melt a material.

Laser: A Laser generates a high energy density beam of photons transmitted and focused to create a spot size of energy.

Laser beam shape: It defines the melt pool shape, mainly the melt pool width size and is chosen coordinately with the power and the travel speed.

Wire feed rate: The transferred mass material per unit time. This variable influences the bead geometry, mainly the bead height and is chosen coordinately with the laser power and the travel speed.

Travel speed: It defines the mass material transferred to the process and is chosen according to the laser power and the wire feed rate. It is the speed of the deposition tool.

Focal length distance: The distance between the last optic to the substrate.

Working distance: It is the distance from the last plate to the substrate. This variable influences the bead geometry deposited, thus the process's stability.

Wire nozzle: The nozzle guides the wire feeding material into the melt pool.

Gaz nozzles: The gaz nozzles direct the shielding gas precisely into the melt pool.

Solidification: Solidification occurs when the melt pool phase changes to a solid state due to a temperature decrease of the material reaching its freezing point. This solidification of the melt pool is called the bead geometry.

Metal: The metal material in a form of wire or powder used in the MAM process. The metal needs certain properties such as durability and strength to be used in high temperatures, corrosive environments, or biocompatible applications.

Molten pool: When the laser power is focused on the metal wire, some of the laser heat is lost, some are reflected to the metal wire and some get absorbed by the metal wire. The absorbed energy consumes and melts the metal to form a melt pool.

Bibliography

[1] Natago Guilé Mbodj, Mohammad Abuabiah, Peter Plapper, Maxime El Kandaoui, and Slah Yaacoubi. Bead geometry prediction in laser-wire additive manufacturing process using machine learning: Case of study. *Applied Sciences*, 11:11949, 12 2021.

[2] Mostafa Yakout, M.A. Elbestawi, and Stephen C. Veldhuis. A review of metal additive manufacturing technologies. *Solid State Phenomena*, 278:1–14, 7 2018.

[3] Global 3d printing report 2016 executive summary. 2016.

[4] Wohlers report 2013: Additive manufacturing state of the industry annual worldwide progress report, wohlers associates. inc., colorado, usa. 2013.

[5] Wohlers report...: 3d printing and additive manufacturing, state of the industry, annual worldwide progress report. wohlers associates incorporated. 2014.

[6] Eu industrial strategy & additive manufacturing: Increasing the resilience of the industrial ecosystems. dg grow - european commission. 2021.

[7] Belforte. Industrial laser market outperforms global manufacturing instability. *Journal of Industrial Laser Solutions, 31.*, 2015.

[8] Hyub Lee, Chin Huat Joel Lim, Mun Ji Low, Nicholas Tham, Vadakke Matham Murukeshan, and Young-Jin Kim. Lasers in additive manufacturing: A review. *International Journal of Precision Engineering and Manufacturing-Green Technology*, 4:307–322, 7 2017.

[9] Osama Abdulhameed, Abdulrahman Al-Ahmari, Wadea Ameen, and Syed Hammad Mian. Additive manufacturing: Challenges, trends, and

applications. *Advances in Mechanical Engineering*, 11:168781401882288, 2 2019.

[10] Yong Huang, Ming C. Leu, Jyoti Mazumder, and Alkan Donmez. Additive manufacturing: Current state, future potential, gaps and needs, and recommendations. *Journal of Manufacturing Science and Engineering*, 137, 2 2015.

[11] Rajat Kawalkar, Harrsh Kumar Dubey, and Satish P. Lokhande. A review for advancements in standardization for additive manufacturing. *Materials Today: Proceedings*, 10 2021.

[12] Donghong Ding, Zengxi Pan, Dominic Cuiuri, and Huijun Li. A multi-bead overlapping model for robotic wire and arc additive manufacturing (waam). *Robotics and Computer-Integrated Manufacturing*, 31:101–110, 2 2015.

[13] Dong-Gyu Ahn. Directed energy deposition (ded) process: State of the art. *International Journal of Precision Engineering and Manufacturing-Green Technology*, 8:703–742, 3 2021.

[14] Richard Leach and Simone Carmignato. *Precision Metal Additive Manufacturing*. CRC Press, 9 2020.

[15] Adrita Dass and Atieh Moridi. State of the art in directed energy deposition: From additive manufacturing to materials design. *Coatings*, 9:418, 6 2019.

[16] AN Jinoop, CP Paul, and KS Bindra. Laser-assisted directed energy deposition of nickel super alloys: A review. *Proceedings of the Institution of Mechanical Engineers, Part L: Journal of Materials: Design and Applications*, 233:2376–2400, 11 2019.

[17] C. P. Paul, S. K. Mishra, C. H. Premsingh, P. Bhargava, P. Tiwari, and L. M. Kukreja. Studies on laser rapid manufacturing of cross-thin-walled porous structures of inconel 625. *The International Journal of Advanced Manufacturing Technology*, 61:757–770, 7 2012.

[18] C.R. Cunningham, J.M. Flynn, A. Shokrani, V. Dhokia, and S.T. Newman. Invited review article: Strategies and processes for high quality wire arc additive manufacturing. *Additive Manufacturing*, 22:672–686, 8 2018.

[19] Tiago A. Rodrigues, V. Duarte, R.M. Miranda, Telmo G. Santos, and J.P. Oliveira. Current status and perspectives on wire and arc additive manufacturing (waam). *Materials*, 12:1121, 4 2019.

[20] Peng Wang, Hanzheng Zhang, Hao Zhu, Qingzhuang Li, and Mengnan Feng. Wire-arc additive manufacturing of az31 magnesium alloy fabricated by cold metal transfer heat source: Processing, microstructure, and mechanical behavior. *Journal of Materials Processing Technology*, 288:116895, 2 2021.

[21] Bintao Wu, Zengxi Pan, Donghong Ding, Dominic Cuiuri, Huijun Li, Jing Xu, and John Norrish. A review of the wire arc additive manufacturing of metals: properties, defects and quality improvement. *Journal of Manufacturing Processes*, 35:127–139, 10 2018.

[22] S. W. Williams, F. Martina, A. C. Addison, J. Ding, G. Pardal, and P. Colegrove. Wire + arc additive manufacturing. *Materials Science and Technology*, 32:641–647, 5 2016.

[23] Jae-Deuk Kim, Joo Yong Cheon, and Changwook Ji. Review on the wire arc additive manufacturing process and trends in non-ferrous alloys. *Journal of Welding and Joining*, 39:603–612, 12 2021.

[24] Michael Zenou and Lucy Grainger. Additive manufacturing of metallic materials, 2018.

[25] Hui-Chin Chang. Parametric design used in the creation of 3d models with weaving characteristics. *Journal of Computer and Communications*, 09:112–127, 2021.

[26] Xiaobo Bai, Omar Huerta, Ertu Unver, James Allen, and Jane E. Clayton. A parametric product design framework for the development of mass customized head/face (eyewear) products. *Applied Sciences*, 11:5382, 6 2021.

[27] Amir Mahyar Khorasani, Ian Gibson, Moshe Goldberg, and Guy Littlefair. A survey on mechanisms and critical parameters on solidification of selective laser melting during fabrication of ti-6al-4v prosthetic acetabular cup. *Materials and Design*, 103:348–355, 8 2016.

[28] Suhas Sreekanth, Ehsan Ghassemali, Kjell Hurtig, Shrikant Joshi, and Joel Andersson. Effect of direct energy deposition process parameters on single-track deposits of alloy 718. *Metals*, 10:96, 1 2020.

[29] S.L. Sing, C.F. Tey, J.H.K. Tan, S. Huang, and Wai Yee Yeong. 3d printing of metals in rapid prototyping of biomaterials: Techniques in additive manufacturing. *Rapid Prototyping of Biomaterials*, pages 17–40, 2020.

[30] Michael Molitch-Hou. Overview of additive manufacturing process. 2018.

[31] Wenhao Huang, Shujun Chen, Jun Xiao, Xiaoqing Jiang, and Yazhou Jia. Laser wire-feed metal additive manufacturing of the al alloy. *Optics and Laser Technology*, 134:106627, 2021.

[32] Abdollah Saboori, Alberta Aversa, Giulio Marchese, Sara Biamino, Mariangela Lombardi, and Paolo Fino. Application of directed energy deposition-based additive manufacturing in repair. *Applied Sciences*, 9:3316, 8 2019.

[33] Taminger K.M. Domack C.S. Challenges in metal additive manufacturing for large-scale aerospace applications", in women in aerospace materials. *Springer: Cham, Switzerland*, pp. 105–124., 2020.

[34] Simone Donadello, Maurizio Motta, Ali Gökhan Demir, and Barbara Previtali. Monitoring of laser metal deposition height by means of coaxial laser triangulation. *Optics and Lasers in Engineering*, 112:136–144, 1 2019.

[35] Yichao Pan. Simplify robot programming with g-code. `https://www.universal-robots.com/blog/simplify-robot-programming-with-g-code`. Accessed: 27-12-2021.

[36] Bingbing Hu, Guoqing Jin, and Lining Sun. A novel adaptive slicing method for additive manufacturing. pages 218–223. IEEE, 5 2018.

[37] Sungwoo Lim, Richard A. Buswell, Philip J. Valentine, Daniel Piker, Simon A. Austin, and Xavier De Kestelier. Modelling curved-layered printing paths for fabricating large-scale construction components. *Additive Manufacturing*, 12:216–230, 10 2016.

[38] Danie Nilsson. G-code to rapid translator for robot-studio. 2016.

[39] Odysseas Kontovourkis and George Tryfonos. Integrating parametric design with robotic additive manufacturing for 3d clay printing: An experimental study. 7 2018.

[40] Odysseas Kontovourkis and George Tryfonos. Robotic 3d clay printing of prefabricated non-conventional wall components based on a parametric-integrated design. *Automation in Construction*, 110:103005, 2 2020.

[41] Thomas Fischer and Christiane Herr. Parametric customisation of a 3d concrete printed pavilion. 1 2016.

[42] Jiwoon Jeong, Hyein Park, Yoojeong Lee, Jihye Kang, and Jaehoon Chun. Developing parametric design fashion products using 3d printing technology. *Fashion and Textiles*, 8:22, 12 2021.

[43] Francesco Naddeo, Alessandro Naddeo, and Nicola Cappetti. Novel "load adaptive algorithm based" procedure for 3d printing of lattice-based components showing parametric curved micro-beams. *Composites Part B: Engineering*, 115:51–59, 4 2017.

[44] Danil Nagy. Computational design in grasshopper. `https://medium.com/generative-design/computational-design-in-grasshopper-1a0b62963690`. Accessed: 05-2020.

[45] T. Schwartz. Hal: Extension of a visual programming language to support teaching and research on robotics applied to construction. *Rob — Arch 2012 (pp. 92–101). Springer Vienna*, 2013.

[46] Donghong Ding, Zengxi Stephen Pan, Dominic Cuiuri, and Huijun Li. A tool-path generation strategy for wire and arc additive manufacturing. *The international journal of advanced manufacturing technology*, 73(1):173–183, 2014.

[47] Nima Shamsaei, Aref Yadollahi, Linkan Bian, and Scott M Thompson. An overview of direct laser deposition for additive manufacturing; part ii: Mechanical behavior, process parameter optimization and control. *Additive Manufacturing*, 8:12–35, 2015.

[48] Robert Sampson, Robert Lancaster, Mark Sutcliffe, David Carswell, Carl Hauser, and Josh Barras. An improved methodology of melt pool monitoring of direct energy deposition processes. *Optics and Laser Technology*, 127:106194, 7 2020.

[49] Noopur Jamnikar, Sen Liu, Craig Brice, and Xiaoli Zhang. Comprehensive process-molten pool relations modeling using cnn for wire-feed laser additive manufacturing. 3 2021.

[50] Giovanni Muscato, Giacomo Spampinato, and Luciano Cantelli. A closed loop welding controller for a rapid manufacturing process. *2008 IEEE International Conference on Emerging Technologies and Factory Automation*, pages 1080–1083, 9 2008.

[51] Lijun Song, Vijayavel Bagavath-Singh, Bhaskar Dutta, and Jyoti Mazumder. Control of melt pool temperature and deposition height during direct metal deposition process. *The International Journal of Advanced Manufacturing Technology*, 58:247–256, 1 2012.

[52] Yaoyu Ding, James Warton, and Radovan Kovacevic. Development of sensing and control system for robotized laser-based direct metal addition system. *Additive Manufacturing*, 10:24–35, 4 2016.

[53] Guijun Bi, Andres Gasser, Konrad Wissenbach, Alexander Drenker, and Reinhart Poprawe. Characterization of the process control for the direct laser metallic powder deposition. *Surface and Coatings Technology*, 201:2676–2683, 12 2006.

[54] F. Meriaudeau and F. Truchetet. Control and optimization of the laser cladding process using matrix cameras and image processing. *Journal of Laser Applications*, 8:317–324, 12 1996.

[55] Ehsan Toyserkani and Amir Khajepour. A mechatronics approach to laser powder deposition process. *Mechatronics*, 16:631–641, 12 2006.

[56] Dongming Hu and Radovan Kovacevic. Sensing, modeling and control for laser-based additive manufacturing. *International Journal of Machine Tools and Manufacture*, 43:51–60, 1 2003.

[57] Mahlen D. T. Fox, Duncan P. Hand, Daoning Su, Julian D. C. Jones, Stephen A. Morgan, Mark A. McLean, and William M. Steen. Optical sensor to monitor and control temperature and build height of the laser direct-casting process. *Applied Optics*, 37:8429, 12 1998.

[58] J. Mazumder, D. Dutta, N. Kikuchi, and A. Ghosh. Closed loop direct metal deposition: art to part. *Optics and Lasers in Engineering*, 34:397–414, 10 2000.

[59] Yuan Cheng and Mohsen A. Jafari. Vision-based online process control in manufacturing applications. *IEEE Transactions on Automation Science and Engineering*, 5:140–153, 1 2008.

[60] Almir Heralić, Anna-Karin Christiansson, Mattias Ottosson, and Bengt Lennartson. Increased stability in laser metal wire deposition through feedback from optical measurements. *Optics and Lasers in Engineering*, 48:478–485, 4 2010.

[61] M. Doubenskaia. Comprehensive optical monitoring of selective laser melting. *Journal of Laser Micro/Nanoengineering*, 7:236–243, 11 2012.

[62] Jun Xiong and Guangjun Zhang. Online measurement of bead geometry in gmaw-based additive manufacturing using passive vision. *Measurement Science and Technology*, 24:115103, 11 2013.

[63] Sörn Ocylok, Eugen Alexeev, Stefan Mann, Andreas Weisheit, Konrad Wissenbach, and Ingomar Kelbassa. Correlations of melt pool geometry and process parameters during laser metal deposition by coaxial process monitoring. *Physics Procedia*, 56:228–238, 2014.

[64] Christian Gobert, Edward W. Reutzel, Jan Petrich, Abdalla R. Nassar, and Shashi Phoha. Application of supervised machine learning for defect detection during metallic powder bed fusion additive manufacturing using high resolution imaging. *Additive Manufacturing*, 21:517–528, 5 2018.

[65] S. Clijsters, T. Craeghs, S. Buls, K. Kempen, and J.-P. Kruth. In situ quality control of the selective laser melting process using a high-speed, real-

time melt pool monitoring system. *The International Journal of Advanced Manufacturing Technology*, 75:1089–1101, 11 2014.

[66] Jun Xiong, Guangchao Liu, and Yupeng Pi. Increasing stability in robotic gta-based additive manufacturing through optical measurement and feedback control. *Robotics and Computer-Integrated Manufacturing*, 59:385–393, 10 2019.

[67] Paul O'Regan, Paul Prickett, Rossi Setchi, Gareth Hankins, and Nick Jones. Metal based additive layer manufacturing: Variations, correlations and process control. *Procedia Computer Science*, 96:216–224, 2016.

[68] Johanna Müller, Marcel Grabowski, Christoph Müller, Jonas Hensel, Julian Unglaub, Klaus Thiele, Harald Kloft, and Klaus Dilger. Design and parameter identification of wire and arc additively manufactured (waam) steel bars for use in construction. *Metals*, 9:725, 6 2019.

[69] Mingming Ma, Zemin Wang, Ming Gao, and Xiaoyan Zeng. Layer thickness dependence of performance in high-power selective laser melting of 1cr18ni9ti stainless steel. *Journal of Materials Processing Technology*, 215:142–150, 1 2015.

[70] I. Yadroitsev and I. Smurov. Selective laser melting technology: From the single laser melted track stability to 3d parts of complex shape. *Physics Procedia*, 5:551–560, 2010.

[71] Kai Guan, Zemin Wang, Ming Gao, Xiangyou Li, and Xiaoyan Zeng. Effects of processing parameters on tensile properties of selective laser melted 304 stainless steel. *Materials and Design*, 50:581–586, 9 2013.

[72] M. Averyanova, E. Cicala, Ph. Bertrand, and Dominique Grevey. Experimental design approach to optimize selective laser melting of martensitic 17-4 ph powder: part i – single laser tracks and first layer. *Rapid Prototyping Journal*, 18:28–37, 1 2012.

[73] K. Dai and L. Shaw. Parametric studies of multi-material laser densification. *Materials Science and Engineering: A*, 430:221–229, 8 2006.

[74] Gangxian Zhu, Dichen Li, Anfeng Zhang, Gang Pi, and Yiping Tang. The influence of laser and powder defocusing characteristics on the surface quality in laser direct metal deposition. *Optics and Laser Technology*, 44:349–356, 3 2012.

[75] Osvaldo Simeone. A brief introduction to machine learning for engineers. *Foundations and Trends in Signal Processing*, 12(3-4):200–431, 2018.

[76] German I Parisi, Ronald Kemker, Jose L Part, Christopher Kanan, and Stefan Wermter. Continual lifelong learning with neural networks: A review. *Neural Networks*, 113:54–71, 2019.

[77] Samir Khatir, Samir Tiachacht, Cuong Le Thanh, Emad Ghandourah, Seyedali Mirjalili, and Magd Abdel Wahab. An improved artificial neural network using arithmetic optimization algorithm for damage assessment in fgm composite plates. *Composite Structures*, 273:114287, 2021.

[78] H Tran-Ngoc, S Khatir, H Ho-Khac, G De Roeck, T Bui-Tien, and M Abdel Wahab. Efficient artificial neural networks based on a hybrid metaheuristic optimization algorithm for damage detection in laminated composite structures. *Composite Structures*, 262:113339, 2021.

[79] Roumaissa Zenzen, Samir Khatir, Idir Belaidi, Cuong Le Thanh, and Magd Abdel Wahab. A modified transmissibility indicator and artificial neural network for damage identification and quantification in laminated composite structures. *Composite Structures*, 248:112497, 2020.

[80] Jun Xiong, Guangjun Zhang, Jianwen Hu, and Lin Wu. Bead geometry prediction for robotic gmaw-based rapid manufacturing through a neural network and a second-order regression analysis. *Journal of Intelligent Manufacturing*, 25:157–163, 2 2014.

[81] D.S. Nagesh and G.L. Datta. Genetic algorithm for optimization of welding variables for height to width ratio and application of ann for prediction of bead geometry for tig welding process. *Applied Soft Computing*, 10:897–907, 6 2010.

[82] Chunyang Xia, Zengxi Pan, Joseph Polden, Huijun Li, Yanling Xu, and Shanben Chen. Modelling and prediction of surface roughness in wire arc additive manufacturing using machine learning. *Journal of Intelligent Manufacturing*, 1 2021.

[83] Sarah Milhomme, Julie Lartigau, Charles Brugger, and Catherine Froustey. Bead geometry prediction using multiple linear regression analysis. *The International Journal of Advanced Manufacturing Technology*, 117:607–620, 11 2021.

[84] M. Karmuhilan and Anoop kumar sood. Intelligent process model for bead geometry prediction in waam. *Materials Today: Proceedings*, 5:24005–24013, 2018.

[85] Christian Wacker, Markus Köhler, Martin David, Franziska Aschersleben, Felix Gabriel, Jonas Hensel, Klaus Dilger, and Klaus Dröder. Geometry and distortion prediction of multiple layers for wire arc additive manufacturing with artificial neural networks. *Applied Sciences*, 11(10):4694, 2021.

[86] K Ren, Y Chew, N Liu, YF Zhang, JYH Fuh, and GJ Bi. Integrated numerical modelling and deep learning for multi-layer cube deposition planning in laser aided additive manufacturing. *Virtual and Physical Prototyping*, pages 1–15, 2021.

[87] FQ Liu, L Wei, SQ Shi, and HL Wei. On the varieties of build features during multi-layer laser directed energy deposition. *Additive Manufacturing*, 36:101491, 2020.

[88] Ananth Ranganathan. The levenberg-marquardt algorithm. *Tutoral on LM algorithm*, 11(1):101–110, 2004.

[89] Rob Farber. Cuda application design and development. 2011.

[90] Ivan Cazic, Julien Zollinger, S Mathieu, Maxime El Kandaoui, Peter Plapper, and Benoit Appolaire. New insights into the origin of fine equiaxed microstructures in additively manufactured inconel 718. *Scripta Materialia*, 195:113740, 2021.

[91] P Peyre, P Aubry, R Fabbro, R Neveu, and A Longuet. Analytical and numerical modelling of the direct metal deposition laser process. *Journal of Physics D: Applied Physics*, 41:025403, 1 2008.

[92] Dmitrii Mukin, Ekaterina Valdaytseva, Gleb Turichin, and Artur Vildanov. An extended analytical solution of the non-stationary heat conduction problem in multi-track thick-walled products during the additive manufacturing process. *Materials*, 14:7291, 11 2021.

[93] Zhichao Liu, Hong-Chao Zhang, Shitong Peng, Hoyeol Kim, Dongping Du, and Weilong Cong. Analytical modeling and experimental validation of powder stream distribution during direct energy deposition. *Additive Manufacturing*, 30:100848, 12 2019.

[94] Prabu Balu, Perry Leggett, and Radovan Kovacevic. Parametric study on a coaxial multi-material powder flow in laser-based powder deposition process. *Journal of Materials Processing Technology*, 212:1598–1610, 7 2012.

[95] O. Illies, G. Li, J.-P. Jürgens, V. Ploshikhin, D. Herzog, and C. Emmelmann. Numerical modelling and experimental validation of thermal history of titanium alloys in laser beam melting. *Procedia CIRP*, 74:92–96, 2018.

[96] X. He and J. Mazumder. Transport phenomena during direct metal deposition. *Journal of Applied Physics*, 101:053113, 3 2007.

[97] Liubov Magerramova, Vladimir Isakov, Liana Shcherbinina, Suren Gukasyan, Mikhail Petrov, Daniil Povalyukhin, Darya Volosevich, and Olga Klimova-Korsmik. Design, simulation and optimization of an additive laser-based manufacturing process for gearbox housing with reduced weight made from alsi10mg alloy. *Metals*, 12:67, 12 2021.

[98] F.R. Liu, Q. Zhang, W.P. Zhou, J.J. Zhao, and J.M. Chen. Micro scale 3d fem simulation on thermal evolution within the porous structure in selective laser sintering. *Journal of Materials Processing Technology*, 212:2058–2065, 10 2012.

[99] Seifallah Fetni, Tommaso Maurizi Enrici, Tobia Niccolini, Hoang Son Tran, Olivier Dedry, Laurent Duchêne, Anne Mertens, and Anne Marie Habraken.

Thermal model for the directed energy deposition of composite coatings of 316l stainless steel enriched with tungsten carbides. *Materials and Design*, 204:109661, 6 2021.

[100] David J. Corbin, Abdalla R. Nassar, Edward W. Reutzel, Allison M. Beese, and Nathan A. Kistler. Effect of directed energy deposition processing parameters on laser deposited inconel ¡sup¿®¡/sup¿ 718: External morphology. *Journal of Laser Applications*, 29:022001, 5 2017.

[101] Xiao Zhang, Weijun Shen, Vignesh Suresh, Jakob Hamilton, Li-Hsin Yeh, Xuepeng Jiang, Zhan Zhang, Qing Li, Beiwen Li, Iris V. Rivero, and Hantang Qin. In situ monitoring of direct energy deposition via structured light system and its application in remanufacturing industry. *The International Journal of Advanced Manufacturing Technology*, 116:959–974, 9 2021.

[102] Numerical simulation development and computational optimization for directed energy deposition additive manufacturing process. *Materials*, 13:2666, 6 2020.

[103] Joy Gockel, Jack Beuth, and Karen Taminger. Integrated control of solidification microstructure and melt pool dimensions in electron beam wire feed additive manufacturing of ti-6al-4v. *Additive Manufacturing*, 1-4:119–126, 10 2014.

[104] Panagiotis Michaleris. Modeling metal deposition in heat transfer analyses of additive manufacturing processes. *Finite Elements in Analysis and Design*, 86:51–60, 9 2014.

[105] L. Dong, A. Makradi, S. Ahzi, and Y. Remond. Three-dimensional transient finite element analysis of the selective laser sintering process. *Journal of Materials Processing Technology*, 209:700–706, 1 2009.

[106] Yuze Huang, Mir Behrad Khamesee, and Ehsan Toyserkani. A comprehensive analytical model for laser powder-fed additive manufacturing. *Additive Manufacturing*, 12:90–99, 10 2016.

[107] Yuze Huang, Mir Behrad Khamesee, and Ehsan Toyserkani. A new physics-based model for laser directed energy deposition (powder-fed additive man-

ufacturing): From single-track to multi-track and multi-layer. *Optics and Laser Technology*, 109:584–599, 1 2019.

[108] Charalabos Doumanidis and Yong-Min Kwak. Geometry modeling and control by infrared and laser sensing in thermal manufacturing with material deposition. *Journal of Manufacturing Science and Engineering*, 123:45–52, 2 2001.

[109] Qian Wang, Jianyi Li, Michael Gouge, Abdalla R. Nassar, Panagiotis (Pan) Michaleris, and Edward W. Reutzel. Physics-based multivariable modeling and feedback linearization control of melt-pool geometry and temperature in directed energy deposition. *Journal of Manufacturing Science and Engineering*, 139, 2 2017.

[110] Malte Buhr, Julian Weber, Jan-Philip Wenzl, Mauritz Möller, and Claus Emmelmann. Influences of process conditions on stability of sensor controlled robot-based laser metal deposition. *Procedia CIRP*, 74:149–153, 2018.

[111] Daisuke Kono, Haruyuki maguchi, Yohei Oda, and Toshimasa Sakai. Stabilization of standoff distance by efficient and adaptive updating of layer height command in directed energy deposition. *CIRP Journal of Manufacturing Science and Technology*, 31:244–250, 11 2020.

[112] Andrew J. Pinkerton and Lin Li. The significance of deposition point standoff variations in multiple-layer coaxial laser cladding (coaxial cladding standoff effects). *International Journal of Machine Tools and Manufacture*, 44:573–584, 5 2004.

[113] Melt pool temperature control for laser metal deposition processes—part ii: Layer-to-layer temperature control. *Journal of Manufacturing Science and Engineering*, 132, 2 2010.

[114] T W Eagar and N S Tsai. Temperature fields produced by traveling distributed heat sources. *Weld. Res. Suppl.; (United States)*, 12 1983.

[115] D Rosenthal. The theory of moving sources of heat and its application of metal treatments. 1946.

[116] Liu Cao and Xuefeng Yuan. Study on the numerical simulation of the slm molten pool dynamic behavior of a nickel-based superalloy on the workpiece scale. *Materials*, 12:2272, 7 2019.

[117] Patcharapit Promoppatum, Shi-Chune Yao, P. Chris Pistorius, and Anthony D. Rollett. A comprehensive comparison of the analytical and numerical prediction of the thermal history and solidification microstructure of inconel 718 products made by laser powder-bed fusion. *Engineering*, 3:685–694, 10 2017.

[118] Erin B. Curry, Sanjubala Sahoo, Chloe Herrera, Ilya Sochnikov, S. Pamir Alpay, Rainer J. Hebert, Brian G. Willis, Jie Qi, and Jason N. Hancock. Optical response of nickel-based superalloy inconel-718 for applications in additive manufacturing. *Journal of Applied Physics*, 127:245111, 6 2020.

[119] José Díaz-Álvarez, Alberto Tapetado, Carmen Vázquez, and Henar Miguélez. Temperature measurement and numerical prediction in machining inconel 718. *Sensors*, 17:1531, 6 2017.

[120] Lev Podshivalov, Cynthia M. Gomes, Andrea Zocca, Jens Guenster, Pinhas Bar-Yoseph, and Anath Fischer. Design, analysis and additive manufacturing of porous structures for biocompatible micro-scale scaffolds. *Procedia CIRP*, 5:247–252, 2013.

[121] Meysam Akbari and Radovan Kovacevic. Closed loop control of melt pool width in robotized laser powder–directed energy deposition process. *The International Journal of Advanced Manufacturing Technology*, 104:2887–2898, 10 2019.

[122] Lijun Song and Jyoti Mazumder. Feedback control of melt pool temperature during laser cladding process. *IEEE Transactions on Control Systems Technology*, 19:1349–1356, 11 2011.

[123] Wim Devesse, Dieter De Baere, Michaël Hinderdael, and Patrick Guillaume. Temperature feedback control of laser cladding using high resolution hyperspectral imaging. *International Congress on Applications of Lasers and Electro-Optics*, page 1305, 2016.

[124] Mohammad H. Farshidianfar, Amir Khajepour, and Adrian Gerlich. Real-time control of microstructure in laser additive manufacturing. *The International Journal of Advanced Manufacturing Technology*, 82:1173–1186, 2 2016.

[125] Iker Garmendia, Joseba Pujana, Aitzol Lamikiz, Mikel Madarieta, and Josu Leunda. Structured light-based height control for laser metal deposition. *Journal of Manufacturing Processes*, 42:20–27, 6 2019.

[126] Almir Heralić, Anna-Karin Christiansson, and Bengt Lennartson. Height control of laser metal-wire deposition based on iterative learning control and 3d scanning. *Optics and Lasers in Engineering*, 50:1230–1241, 9 2012.

[127] Yangbo Liu, Liuping Wang, and Milan Brandt. Model predictive control of laser metal deposition. *The International Journal of Advanced Manufacturing Technology*, 105:1055–1067, 11 2019.

[128] Jun Xiong, Ziqiu Yin, and Weihua Zhang. Closed-loop control of variable layer width for thin-walled parts in wire and arc additive manufacturing. *Journal of Materials Processing Technology*, 233:100–106, 7 2016.

[129] Mohammad H. Farshidianfar, Amir Khajepour, Meysar Zeinali, and Adrian Gelrich. System identification and height control of laser cladding using adaptive neuro-fuzzy inference systems. *International Congress on Applications of Lasers and Electro-Optics*, pages 615–623, 2013.

[130] Meysar Zeinali and Amir Khajepour. Height control in laser cladding using adaptive sliding mode technique: Theory and experiment. *Journal of Manufacturing Science and Engineering*, 132, 8 2010.

[131] S. Moralejo, X. Penaranda, S. Nieto, A. Barrios, I. Arrizubieta, I. Tabernero, and J. Figueras. A feedforward controller for tuning laser cladding melt pool geometry in real time. *The International Journal of Advanced Manufacturing Technology*, 89:821–831, 3 2017.

[132] Masanori Miyagi, Takeshi Tsukamoto, and Hirotsugu Kawanaka. Adaptive shape control of laser-deposited metal structures by adjusting weld pool size. *Journal of Laser Applications*, 26:032003, 8 2014.

[133] Alireza Fathi, Amir Khajepour, Mohammad Durali, and Ehsan Toyserkani. Geometry control of the deposited layer in a nonplanar laser cladding process using a variable structure controller. *Journal of Manufacturing Science and Engineering*, 130, 6 2008.

[134] Robert Morgan. Linearization and stability analysis of nonlinear problems. *Rose–Hulman Undergraduate Mathematics Journal*, 16:5, 2015.

[135] Holger Voos. Nonlinear state-dependent riccati equation control of a quadrotor uav. *2006 IEEE Conference on Computer Aided Control System Design, 2006 IEEE International Conference on Control Applications, 2006 IEEE International Symposium on Intelligent Control*, pages 2547–2552, 10 2006.

[136] Olivier Brüls and Peter Eberhard. On the complete integrability and linearization of nonlinear ordinary differential equations. iii. coupled first-order equations. *Proceedings of the Royal Society A: Mathematical, Physical and Engineering Sciences*, 465:585–608, 2 2009.

[137] Olivier Brüls and Peter Eberhard. Sensitivity analysis for dynamic mechanical systems with finite rotations. *International Journal for Numerical Methods in Engineering*, 74:1897–1927, 6 2008.

[138] Guaraci Bastos, Robert Seifried, and Olivier Brüls. Analysis of stable model inversion methods for constrained underactuated mechanical systems. *Mechanism and Machine Theory*, 111:99–117, 5 2017.

[139] Chunyang Xia, Zengxi Pan, Joseph Polden, Huijun Li, Yanling Xu, Shanben Chen, and Yuming Zhang. A review on wire arc additive manufacturing: Monitoring, control and a framework of automated system. *Journal of Manufacturing Systems*, 57:31–45, 2020.

[140] J Anthony Rossiter. *Model-based predictive control: a practical approach.* CRC press, 2017.

[141] Ivan Cazic, Julien Zollinger, S Mathieu, Maxime El Kandaoui, Peter Plapper, and Benoit Appolaire. New insights into the origin of fine equiaxed

microstructures in additively manufactured inconel 718. *Scripta Materialia*, 195:113740, 2021.